Direct Measurement of the Hyperfine Structure Interval of Positronium Using High Power Millimeter wave Technology

Ph. D. thesis

Akira Miyazaki

Department of Physics
Faculty of Science, The University of Tokyo

December 2013

Abstract

In this thesis, positronium hyperfine structure (Ps-HFS) is directly measured. This is the first direct measurement of Ps-HFS. Although Ps-HFS has been *indirectly* measured with a Zeeman splitting method since 1952, there is no precedents for the *direct* measurement because Ps-HFS is in the millimeter-wave range (frequency $\Delta_{\mathrm{Ps}}^{\mathrm{HFS}} = 203$ GHz, wavelength = 1.5 mm, energy difference = 0.83 meV). A gyrotron oscillator is developed as a high-power millimeter-wave radiation source. A Fabry-Pérot resonant cavity accumulates radiation to equivalent power of about 20 kW to cause the induced transition between *ortho*-positronium and *para*-positronium. The obtained Ps-HFS value is

$$\Delta_{\mathrm{Ps}}^{\mathrm{HFS}} = 203.39^{+0.15}_{-0.14}\,(\mathrm{stat.}) \pm 0.11\,(\mathrm{syst.})\,\mathrm{GHz} \tag{1}$$

At the same time, lifetime of *para*-positronium is directly measured as

$$\tau_{\mathrm{p\text{–}Ps}} = 89^{+18}_{-15}\,(\mathrm{stat.}) \pm 10\,(\mathrm{syst.})\,\mathrm{ps} \tag{2}$$

This is also the first direct measurement of $\tau_{\mathrm{p\text{–}Ps}}$. They are consistent with QED calculations.

Contents

List of Figures

List of Tables

Chapter 1

Introduction

Quantum electrodynamics (QED) is the most successful quantum field theory. A lot of experiments give results in good agreement with calculated predictions. However, there are two problems in tests of QED: g-2 anomaly of muon ($> 3\sigma$) [1] and Lamb shift of muonic hydrogen ($\sim 5\sigma$, so called the proton charge radius puzzle) [2][3]. Uncertainties from the nuclear structure effects might be systematic problems in theoretical calculations. To overcome this limitation, one possibility is to study purely leptonic systems like positronium. Another problem exists between previous indirect measurements of hyperfine structure of positronium and *purely leptonic* QED predictions. In this thesis, positronium hyperfine structure is measured with a direct transition method. Direct measurement has not yet performed because of technological problems, and is a possible future candidate to solve this anomaly.

1.1 Positronium

	Ps	Hydrogen
mass	1.022 MeV	939.0 MeV
reduced mass	$m_e/2$	m_e
Bohr radius	0.105 nm	0.053 nm
I^{1st}	6.8 eV	13.6 eV
HFS	203.39 GHz	1.42 GHz

Table 1.1: Comparison of positronium and hydrogen atom.

Positronium (Ps), the bound state of an electron and a positron, is a good system with which to precisely study bound-state QED [4]. Positron and electron are so much lighter than the lightest hadrons or muon that the effects of strong interactions are negligible compared with the accuracy of present and any conceivable future experiments. For this reason, Ps is the unique system which can be described with very high precision by means of the QED only.

Ps is the lightest hydrogen-like atom. Table 1.1 compares Ps with a hydrogen atom. The Bohr radius of Ps is twice as large as that of hydrogen, and the first ionization potential (I^{1st}) is half as small as that of hydrogen. The states of Ps are classified according to the principal quantum number n, a sum of the orbital angular momentum L, a spin angular momentum S, and a total angular momentum J

$$n\ ^{2S+1}L_J. \tag{1.1}$$

A level structure of Ps are shown in Fig. 1.1. $L = 1$ states are unstable to emit a Lyman-α photon (243 nm). Some transitions have been studied precisely [5][6][7][8].

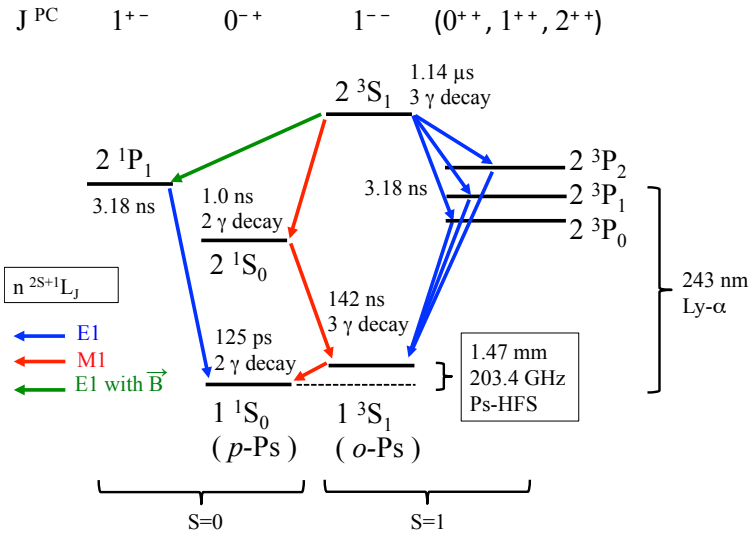

Figure 1.1: Schematic diagram of the lowest energy levels of positronium.

In this thesis, we discuss the magnetic dipole (M1) transition at the ground state. There are two spin states in the ground state: the $1\,^3S_1$ state (triplet) and the $1\,^1S_0$ state (singlet). The triplet state is called *ortho*-positronium (o-Ps), and the singlet state is called *para*-positronium (p-Ps). One denotes the o-Ps states and the p-Ps state with a ket notation $|S, m\rangle$

$$o\text{–Ps} \quad \begin{cases} |1,+1\rangle &= |\uparrow\Uparrow\rangle \\ |1,\ \ 0\rangle &= \frac{1}{\sqrt{2}}\left(|\uparrow\Downarrow\rangle + |\downarrow\Uparrow\rangle\right) \\ |1,-1\rangle &= |\downarrow\Downarrow\rangle \end{cases} \tag{1.2}$$

$$p\text{–Ps} \quad |0,\ \ 0\rangle = \frac{1}{\sqrt{2}}\left(|\uparrow\Downarrow\rangle - |\downarrow\Uparrow\rangle\right) \tag{1.3}$$

where m represents projection of S to the quantization axis, $\uparrow$ and $\Uparrow$ represent electron spin and positron spin, respectively. The energy level of the o-Ps state is slightly higher than p-Ps by a hyperfine structure interval (HFS) due to the spin-spin interaction. As shown in Table 1.1, HFS of Ps (Ps-HFS) is about 203 GHz, and 140 times as high as that of hydrogen (H-HFS). The detail of the hyperfine structure is described in the next section.

name	total spin S	projection m	C	P	decay mode	lifetime
p-Ps	0	0	+	−	2γ(, 4γ, 6γ, ...)	125 ps
o-Ps	1	0, ±1	−	−	3γ(, 5γ, 7γ, ...)	142 ns

Table 1.2: The classification of Ps according to its quantum numbers.

$L = 0$ states decay into some γ rays as shown in Table 1.2. Charge parity of o-Ps and p-Ps is odd and even, respectively ($C = (-1)^{L+S}$). Since a system of n photons has $C = (-1)^n$, o-Ps decays only into odd γ rays, and p-Ps decays only into even γ rays due to C-conservation. Single photon decay of o-Ps is prohibited by energy-momentum conservation. As the number of photons increases, the width of the decay mode decreases by a factor of the fine structure constant ($\alpha \sim 1/137$), and phase space of the final state is getting smaller. Thus, decay modes into many photons are highly suppressed. As a result, p-Ps mainly decays into two γ rays and o-Ps mainly decays into three γ rays. The experimental values of the decay rate of p-Ps and o-Ps are

$$\Gamma_{\text{p–Ps}} = 7.990\ 9(17) \times 10^9\ \text{s}^{-1}\ [9], \tag{1.4}$$

$$\Gamma_{\text{o–Ps}} = 7.040\ 1(7) \times 10^6\ \text{s}^{-1}\ [10]. \tag{1.5}$$

These decay rates are remarkably smaller than hadronic systems like J/Ψ. It is one advantage of Ps when one studies particle-antiparticle systems precisely.

1.2 Positronium Hyperfine Structure

Let us derive Ps-HFS ($\Delta^{\text{Ps}}_{\text{HFS}}$) in the lowest order calculation. An energy shift by the spin-spin interaction E^{Ps}_{b} is expressed as [11]

$$E^{\text{Ps}}_{\text{b}} = -\overrightarrow{\mu^-_{\text{e}}} \cdot \overrightarrow{B}, \tag{1.6}$$

where $\overrightarrow{B}$ is the magnetic field at the electron induced by the positron magnetic moment

$$\overrightarrow{B} = \overrightarrow{\nabla} \times \left[\frac{1}{4\pi} \overrightarrow{\mu^+_{\text{e}}} \times \overrightarrow{\nabla} \frac{1}{r} \right], \tag{1.7}$$

and $\overrightarrow{\mu^{\mp}_{\text{e}}}$ denotes the electron and positron magnetic moment with the Pauli matrix $\overrightarrow{\sigma}$

$$\overrightarrow{\mu^{\mp}_{\text{e}}} = \frac{\mp e}{m_{\text{e}}} \frac{\overrightarrow{\sigma}}{2} \tag{1.8}$$

$$\tag{1.9}$$

Using wave function of Ps $\phi(r)$ at $r = 0$, one obtains

$$\langle E_{\rm b}^{\rm Ps} \rangle = \frac{2\pi\alpha}{3m_{\rm e}^2} \langle \overrightarrow{\sigma_{\rm e+}} \cdot \overrightarrow{\sigma_{\rm e-}} \rangle \left| \phi(0) \right|^2 . \tag{1.10}$$

For the ground state

$$|\phi(0)|^2 = \frac{(m_{\rm e}\alpha)^3}{8\pi}. \tag{1.11}$$

The left figure of Fig. 1.2 shows the diagram of this spin-spin interaction. In addition, there is another contribution to Ps-HFS: a virtual annihilation channel shown in the right of Fig. 1.2

$$\langle E_{\rm A}^{\rm Ps} \rangle = \frac{\pi\alpha}{m_{\rm e}^2} \left\langle \overrightarrow{S}^2 \right\rangle \left| \phi(0) \right|^2 , \tag{1.12}$$

where $\overrightarrow{S}$ denotes total spin. The annihilation channel only contributes to o-Ps because of C conservation.

Figure 1.2: Feynman diagram of the lowest order Ps-HFS. Left shows the spin-spin interaction $\langle E_{\rm b}^{\rm Ps} \rangle$ (exchange of covariant photon). Right represents virtual annihilation channel $\langle E_{\rm A}^{\rm Ps} \rangle$.

Ps-HFS is obtained by subtracting $\langle E_{\rm b}^{\rm Ps} \rangle + \langle E_{\rm A}^{\rm Ps} \rangle$ of p-Ps from that of o-Ps

$$\begin{aligned} \Delta_{\rm HFS}^{\rm Ps} &= \text{spin exchange} + \text{annihilation} \\ &= \frac{1}{3} m_{\rm e}\alpha^4 + \frac{1}{4} m_{\rm e}\alpha^4 \\ &= \frac{7}{12} m_{\rm e}\alpha^4 \sim 204\,\text{GHz} \end{aligned} \tag{1.13}$$

One can derive the value of H-HFS ($\Delta_{\rm HFS}^{\rm H}$) in a similar way except for the virtual annihilation channel

$$\Delta_{\rm HFS}^{\rm H} = \langle E_{\rm b}^{\rm H} \rangle \sim 1.42\,\text{GHz}, \tag{1.14}$$

Ps-HFS is much larger than H-HFS because of its large magnetic moment or light mass. Ps-HFS is sensitive to new physics via the virtual annihilation channel which contributes to the Ps-HFS interval by about 43%. This is one advantage of studying Ps compared with a hydrogen atom. Although precise direct measurements of the H-HFS interval have been performed using hydrogen masers since 1960's [12], that of Ps-HFS has not been performed. The first motivation of this thesis is to measure Ps-HFS with a direct transition method. Theory of the direct transition and its difficulty are described in the next section.

1.3 Theory of Direct Measurement of Ps-HFS

Figure 1.3 is a level diagram for the hyperfine transition of ground-state Ps with radiation of energy density $\rho(\omega)$ per unit angular frequency. The input radiation is assumed to be linearly polarized, and the oscillating magnetic field vector is parallel to $|1,1\rangle$ and $|1,-1\rangle$. In this case, only $|1,0\rangle$ and $|0,0\rangle$ states are affected by the radiation because of angular momentum conservation.

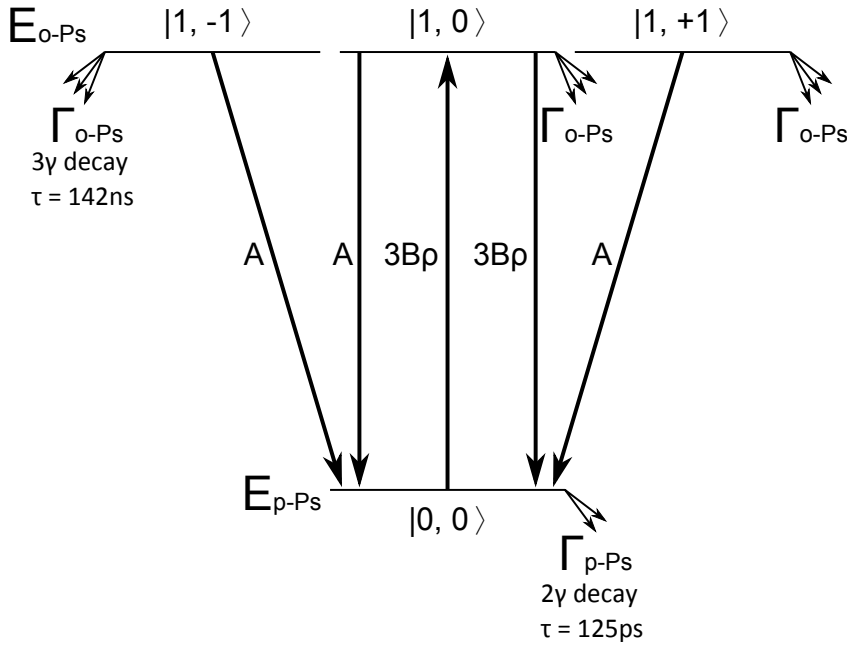

Figure 1.3: Level diagram of the hyperfine structure of positronium

There are some methods to calculate transition probability, for example, a numerical calculation of Hamiltonian [13], or using a Green's function [14]. The simplest method is a rate equation method and is introduced here. When we denote the population of $|S,m\rangle$ states as $N_{S,m}$, then the rate equations are expressed as

$$\begin{aligned}\frac{\mathrm{d}N_{0,0}(\omega,t)}{\mathrm{d}t} &= -3B(\omega)\rho(\omega)N_{0,0}(\omega,t) + 3B(\omega)\rho(\omega)N_{1,0}(\omega,t) \\ &\quad + A(N_{1,0}(\omega,t) + N_{1,+1}(t) + N_{1,-1}(t)) - \Gamma_{\mathrm{p\text{–}Ps}}N_{0,0}(\omega,t) \end{aligned} \tag{1.15}$$

$$\begin{aligned}\frac{\mathrm{d}N_{1,0}(\omega,t)}{\mathrm{d}t} &= 3B(\omega)\rho(\omega)N_{0,0}(\omega,t) - 3B(\omega)\rho(\omega)N_{1,0}(\omega,t) \\ &\quad - AN_{1,0}(\omega,t) - \Gamma_{\mathrm{o\text{–}Ps}}N_{1,0}(\omega,t) \end{aligned} \tag{1.16}$$

$$\frac{\mathrm{d}N_{1,+1}(t)}{\mathrm{d}t} = -AN_{1,+1}(t) - \Gamma_{\mathrm{o\text{–}Ps}}N_{1,+1}(t) \tag{1.17}$$

$$\frac{\mathrm{d}N_{1,-1}(t)}{\mathrm{d}t} = -AN_{1,-1}(t) - \Gamma_{\mathrm{o\text{–}Ps}}N_{1,-1}(t). \tag{1.18}$$

where A is the Einstein coefficient of Ps-HFS (i.e. a spontaneous emission rate) [15]

$$A = \frac{4}{3}\frac{\hbar^2\alpha}{m_e^2c^4}\omega_0^3 = 3.37 \times 10^{-8}\ \mathrm{s}^{-1}, \tag{1.19}$$

and $\omega_0 = 2\pi\Delta_{\mathrm{HFS}}^{\mathrm{Ps}}$. Note that this formula is written in the SI unit while Ref. [15] uses the CGS unit. The spontaneous emission occurs independently of input radiation, and emitted photons (millimeter waves) are unpolarized. The Einstein B coefficient (i.e. the induced transition coefficient) is related to A with a well known formula [16][17],

$$B(\omega) = A\frac{\pi^2c^3}{\hbar\omega_0^3}g(\omega), \tag{1.20}$$

where $g(\omega)$ is a line-shape function which satisfies

$$\int g(\omega)\mathrm{d}\omega = 1. \tag{1.21}$$

Induced photons are polarized corresponding to the linearly polarized input radiation. The pre-factor 3 in the term of $3B(\omega)\rho(\omega)$ is due to this polarization effect.

The spectrum line-shape is broadened, and peak height is suppressed as

$$g_{\mathrm{n}}(\omega) = \frac{1}{\pi}\frac{\Delta\omega_{\mathrm{n}}/2}{(\omega-\omega_0)^2 + (\Delta\omega_{\mathrm{n}}/2)^2}, \tag{1.22}$$

where $\Delta\omega_{\mathrm{n}}$ is the natural width (FWHM) because of the finite lifetimes of the states of Ps, and is expressed as

$$\Delta\omega_{\mathrm{n}} = A + \Gamma_{\mathrm{p\text{–}Ps}} + \Gamma_{\mathrm{o\text{–}Ps}}. \tag{1.23}$$

In the above equation, the decay rate of p-Ps ($\Gamma_{\mathrm{p\text{–}Ps}}$) is dominant and the natural width is about 1.3 GHz in frequency. The pressure broadening can be included in the above equation by replacing the decay rates of Ps in vacuum with those in gas. The Doppler broadening is very small (FWHMu = 80 MHz) because Ps is produced in gas of 300 K and is thermalized enough at this level of precision (We will discuss the non-thermalization problem of Ps in Sec. 1.5.3).

Let us solve Eq. (1.15) (1.16) (1.17) (1.18) by the low power approximation in which the transition rate is small enough (low Rabi frequency) :

$$\Gamma_{\mathrm{tran}} \equiv 3B(\omega)\rho(\omega) \ll \Gamma_{\mathrm{p\text{–}Ps}}. \tag{1.24}$$

This condition is satisfied if input power is less than 100 kW. In this approximation, $N_{0,0}$ promptly decays and decouples from these equations because the opposite transition from p-Ps to o-Ps can be ignored. Thus, the solutions can be expressed

as

$$N_{0,0}(t) = N_{0,0}(0)\exp\left[-\left(\Gamma_{\text{p–Ps}}\right)t\right] \tag{1.25}$$
$$N_{1,0}(t) = N_{1,0}(0)\exp\left[-\left(A+\Gamma_{\text{tran}}+\Gamma_{\text{o–Ps}}\right)t\right] \tag{1.26}$$
$$N_{1,1}(t) = N_{1,1}(0)\exp\left[-\left(A+\Gamma_{\text{o–Ps}}\right)t\right] \tag{1.27}$$
$$N_{1,-1}(t) = N_{1,-1}(0)\exp\left[-\left(A+\Gamma_{\text{o–Ps}}\right)t\right] \tag{1.28}$$

Transition probability in a time window $[t_0, t_1]$ is

$$P_{\text{o–Ps}\to 2\gamma} = \Gamma_{\text{tran}}\int_{t_0}^{t_1} dt N_{1,0} \tag{1.29}$$

This probability is measured by counting the number of 2γ rays emitted from transiting o-Ps. Figure 1.4 shows transition probability with time window $[0, \infty]$.

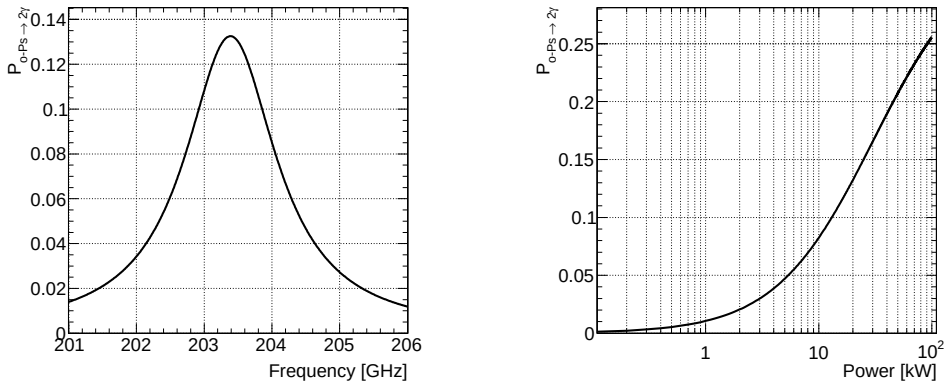

Figure 1.4: Theoretical calculation of transition probability. No pressure broadening and Doppler broadening, power broadening are considered. No time window is required. (left) Transition probability vs frequency (power = 20 kW). (right) Transition probability vs power (frequency = 203.4 kW).

The induced transition rate Γ_{tran} can be reinterpreted with a reaction cross-section $\sigma(\omega)$ [kb] and energy flux I [W/m^2] [17]

$$\Gamma_{\text{tran}} = \sigma \cdot \frac{I}{\hbar\omega}, \tag{1.30}$$

and the reaction cross-section and energy flux are given by

$$\sigma(\omega) = 3A\frac{\pi^2 c^2}{\hbar\omega_0^2}g(\omega) \tag{1.31}$$
$$I = \rho(\omega)c \tag{1.32}$$

For example, when one focuses power of 10 kW on 1 cm^2, corresponding I is about 10^8 [W/m^2], or energy density of 0.3 [J/m^3]. Since $P_{o\text{–}Ps\to 2\gamma}$ depends on the power flux and is inconvenient, $\sigma(\omega)$ is calculated to obtain Ps-HFS using the independently measured power flux.

Total transition probability of Ps and hydrogen with the same energy flux differs only by an effect of different reduced masses. The difficulty of Ps-HFS measurement compared with H-HFS is due to short lifetime of Ps and the frequency. The transition is suppressed with the natural width of $2\pi\Gamma_{p\text{–}Ps} \sim 1.3$ GHz, and the expected value of the transition is reduced with lifetime of o-Ps $\tau_{o\text{–}Ps} = 142$ ns. Thus, high-power 203 GHz radiation of over 10 kW power is required to force o-Ps to transit into p-Ps. A technological challenge related to the frequency is discussed in the next section.

1.4 Millimeter-wave Technology and Our Requirements

A millimeter wave or terahertz (THz) wave is the last electromagnetic wave that remains under development. Figure 1.5 shows so called "THz gap" where we have less understandings and devices than well-developed electronics, optics, or X- and γ-rays. In this frequency range, an electromagnetic wave has a characteristic of both light and radio-wave. It travels in almost a straight line like a laser beam, and is strongly diffracted like radio-wave at the same time. It is lossy in a waveguide, but is difficult to be handled in free space. Short wavelength requires high mechanical accuracy of waveguides, mirrors, or other devices for its propagation. In the millimeter-wave range, most of the materials have high reflectance and absorption with strong frequency dependence. It is very difficult to produce high-power and stable millimeter-wave radiation (>1 W). Even in computer simulations, calculation times of a finite element method can be readily divergent because of high frequency.

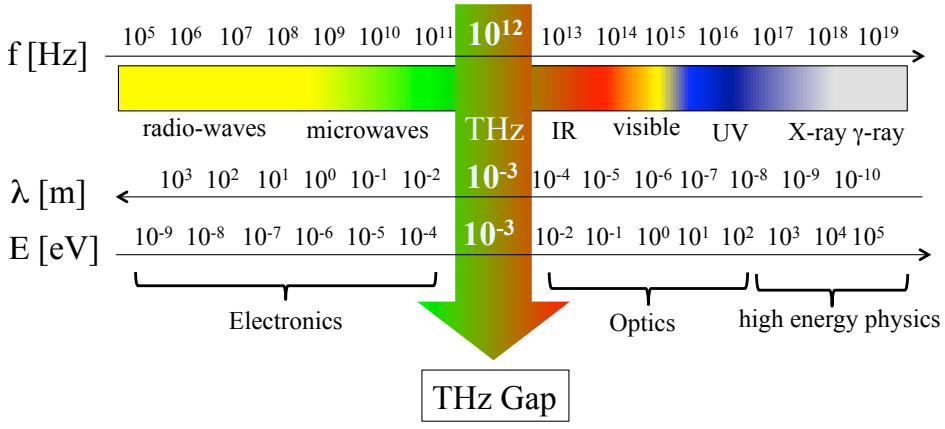

Figure 1.5: Schematic diagram of THz gap.

There are some applications of millimeter waves recently. Cosmic Microwave

Background (CMB) is in the millimeter-wave range, and measurement of the B-mode polarization in CMB is one of the most interesting topics in cosmology [18]. One plans to measure neutrino decay and its absolute mass difference with sensitive millimeter-wave detectors in KEK and Tsukuba University. Millimeter-wave radiation is also a probe to study molecules in astronomy [19] because millimeter (THz) wavelength appears in transitions between rotational (vibrational) levels of many molecules (This phenomenon also appears in this thesis. See Sec. 2.3.2). Above applications require very sensitive superconducting sensors, for examples, Transition Edge Sensor (TES), Superconducting-Insulator-Superconducting (SIS) hetero-dyne detector, Superconducting Tunnel Junction (STJ), Microwave Kinetic Inductance Detectors (MKIDs).

Many application of superconductors to the millimeter-wave detection means that a gap energy of a superconductor is in millimeter-wave energy, and indicates that millimeter waves play an important role in material science. In fact, millimeter waves can be a probe to study an electromagnetic response of a solid near the Fermi energy. Phonon, exiton, polariton, and other exited modes in solids are in the millimeter-wave range. Landau levels are also in the millimeter-wave or THz range, and for example, an application for the quantum Hall effect in graphene is studied recently [20]. It is worth mentioning that Landau levels are also related to a gyrotron oscillator described in Sec. 2.2.1.

The Ps-HFS direct measurement is one of the greatest technological challenges in the millimeter-wave field today. Especially, the requirement for very high power (>10 kW) is quite unique compared with other millimeter-wave science and conventional atomic or nuclear physics. Such high power is only studied to heat plasma in the field of fusion, and not applied to other fundamental science fields [21]. The direct measurement of Ps-HFS with an precision of about 0.1% requires

1. A high-power millimeter-wave oscillator producing over 100 W.
2. A resonant cavity accumulating equivalent power of over 10 kW.
3. A method to measure accumulating power with accuracy of better than 20 %.
4. Frequency stability of better than 200 MHz.
5. A method to scan frequency from 201 GHz to 206 GHz.

To achieve these requirements, we developed an optical system composed of a gyrotron oscillator and a Fabry-Pérot resonant cavity.

A gyrotron is a millimeter-wave oscillator with the highest power developed in plasma physics. Frequency stability of a gyrotron is usually very monochromatic (FWHM is better than 100 kHz) [22]. Since output frequency of a normal gyrotron is lower than 170 GHz, we developed a new gyrotron with 203 GHz output. It was a technical challenge to fabricate such a high frequency (sub-THz) gyrotron. Output frequency is tuned by replacing an internal RF cavity. Details of our gyrotron are explained in Sec. 2.2.1.

A Fabry-Pérot cavity is usually used as an etalon in many frequency regions, and also used as an amplifier in laser physics. Although a basic theory of this cavity is well known [23], it is non-trivial to put this cavity to practical use in the millimeter-wave range. Some ideas were needed to accumulate high-power radiation and to measure its power with the accuracy of 20%. Details of the Fabry-Pérot cavity are described in Sec. 2.2.2. An estimation of accumulated power is one of the key points in this thesis, and explained in Sec. 2.2.3.

1.5 Previous Measurement of Ps-HFS and Observed Discrepancy

1.5.1 Indirect Precision Measurement of Ps-HFS

year	$\Delta_{\mathrm{HFS}}^{\mathrm{Ps}}$ (GHz)	error (ppm)	reference
1952	203.2(3)	1500	[24]
1954	203.38(4)	200	[25]
1955	203.35(5)	250	[26]
1957	203.33(4)	200	[27]
1970	203.403(12)	58	[28]
1972	203.396(5)	24	[29]
1975	203.387 0(16)	8	[30]
1977	203.384(4)	20	[31]
1977	203.384 9(12)	6	[32]
1983	203.387 5(16)	8	[13]
1984	203.389 10(74)	3.6	[33]

Table 1.3: History of the Ps-HFS measurements using the Zeeman effect.

Ps-HFS has been measured indirectly since 1952 as listed in Table 1.3. All of the previous measurements used the Zeeman effect, and indirectly obtained the Ps-HFS interval. The method of indirect measurement is as follows. In a static magnetic field, the o-Ps state with $m = 0$ and the p-Ps state mix, and the resultant energy level of $m = 0$ differs from the $m = \pm 1$ states which is not affected by the magnetic field as shown in Fig. 1.6. The mixture state depends on the strength of the static magnetic field, and the energy difference between the mixed o-Ps state ($|+\rangle$) and the unperturbed o-Ps states ($|1, +1\rangle$, $|1, -1\rangle$) is related to Ps-HFS by the following equation,

$$\Delta_{\mathrm{mix}} = \frac{\Delta_{\mathrm{HFS}}^{\mathrm{Ps}}}{2}\left(\sqrt{1+x^2} - 1\right) \tag{1.33}$$

$$x = \frac{2g'\mu_B B}{h\Delta_{\mathrm{HFS}}^{\mathrm{Ps}}}, \tag{1.34}$$

where $g' = g\left(1 - 5\alpha^2/24\right)$ is the bound state electron g-factor in Ps, B is the strength of the static magnetic field. Therefore, $\Delta_{\rm HFS}^{\rm Ps}$ can be obtained from $\Delta_{\rm mix}$ and B. $\Delta_{\rm mix}$ becomes about 3 GHz when one applies a static magnetic field of about 1 T.

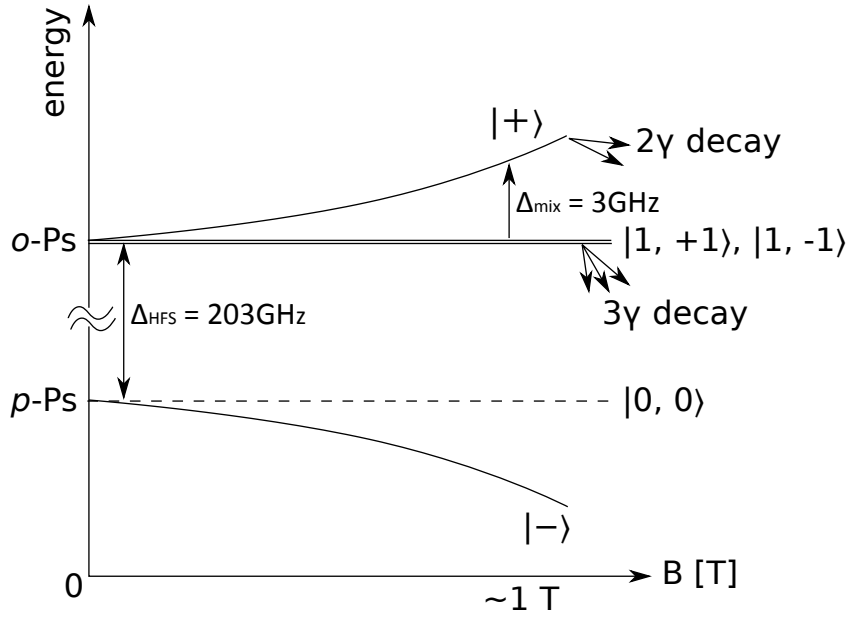

Figure 1.6: Zeeman splitting of Ps.

Figure 1.7 shows a setup of one of the previous measurements. Here, the strong static magnetic field was produced with an electromagnet, and the microwave of about 500 W was produced with a magnetron [13] and a klystron [33]. A Zeeman transition from the unperturbed o-Ps states ($|1,+1\rangle$, $|1,-1\rangle$) to the mixed o-Ps state ($|+\rangle$) occurs when the microwave frequency matches $\Delta_{\rm mix}$. The number of 2γ decays increases on resonance since the $|+\rangle$ state mainly decays into 2γ rays. The transition curve is obtained by measuring the increase of 2γ decays as changing the strength of the static magnetic field. The combined value of the most accurate two independent experiments [13, 33] is

$$\Delta_{\rm HFS}^{\rm Ps}(\text{exp.}) = 203.388\ 65(67)\ \text{GHz}. \tag{1.35}$$

The relative accuracy is 3.3 ppm.

1.5.2 Theoretical Prediction

We derived the Ps-HFS value in the lowest order in Sec. 1.2. Higher order corrections except for the first correction [34] had not been calculated when precise measurements were performed. Measured values and theoretical predictions are consistent since 1950's.

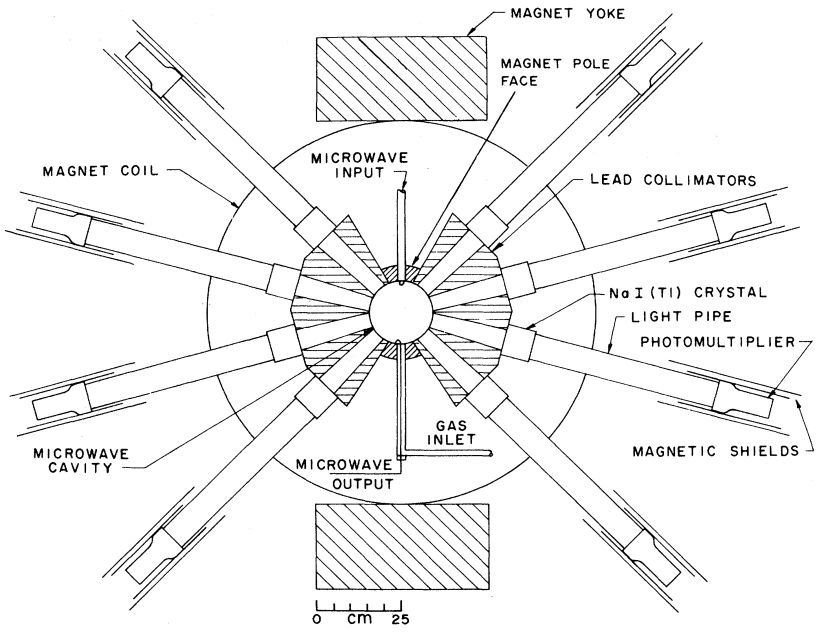

Figure 1.7: Schematic view of the previous experiment [31].

There are two approaches used in the studies of bound states. One is the Bethe-Salpeter method based on an exact two-body relativistic wave equation [11]. The other is nonrelativistic QED (NRQED), which is the effective theory that emerges by expanding the QED Lagrangian in electron velocity in the center-of-mass frame. Thus, the NRQED takes advantage of nonrelativistic energy of the electron and positron in Ps. However, the NRQED calculations lead to divergent results because it is the application of the nonrelativistic expansion in the relativistic momentum region. The divergence is cancelled if one includes additional hard-scale contributions, which is not obtained from the nonrelativistic expansion.

In addition to the difficulties in the bound-state QED, calculation of Ps-HFS has difficulties from its symmetry compared with a hydrogen atom or muonium. In a two-body system composed of mass M and m, recoil effect corrections are generally suppressed by m/M. Ps is strictly $M = m$ (if CPT invariance is true), and this suppression does not work. The fourth-order recoil terms of theory of muonium become the third-order corrections in Ps. Furthermore, the virtual annihilation channel (the right figure of Fig. 1.2) gives rise to many diagrams to be corrected.

A new method to calculate the higher order corrections up to $O(\alpha^3 \log \alpha^{-1})$ is established in 2000 [35][36][37]. To deal with the divergences in the NRQED, these calculations employ dimensional regularization, in which contributions from different energy scales are matched automatically. When one denotes the lowest order result calculated in Sec. 1.2 as $\Delta^{\rm Ps}_{\rm HFS(0)}$, corrected Ps-HFS can be expressed

as [35]

$$\Delta_{\rm HFS}^{\rm Ps}({\rm th}) = \Delta_{\rm HFS(0)}^{\rm Ps}\left\{1-\frac{\alpha}{\pi}\left(\frac{32}{21}+\frac{6}{7}\ln 2\right)+\frac{5}{14}\alpha^2\ln\frac{1}{\alpha}\right. \tag{1.36}$$
$$+\left(\frac{\alpha}{\pi}\right)^2\left[\frac{1367}{378}-\frac{5197}{2016}\pi^2+\left(\frac{6}{7}+\frac{221}{84}\pi^2\right)\ln 2-\frac{159}{56}\zeta(3)\right]$$
$$\left.-\frac{3}{2}\frac{\alpha^3}{\pi}\ln^2\frac{1}{\alpha}+\left(\frac{62}{15}-\frac{68}{7}\ln 2\right)\frac{\alpha^3}{\pi}\ln\frac{1}{\alpha}+D\left(\frac{\alpha}{\pi}\right)^3+\cdots\right\}$$

where the coefficient D is estimated as an error of the current calculation using hyperfine structure of muonium. The QED prediction of Ps-HFS is

$$\Delta_{\rm HFS}^{\rm Ps}({\rm th}) = 203.391\ 69(41)\ {\rm GHz}. \tag{1.37}$$

The relative accuracy is 2.0 ppm.

1.5.3 Discrepancy between Experiments and Theory

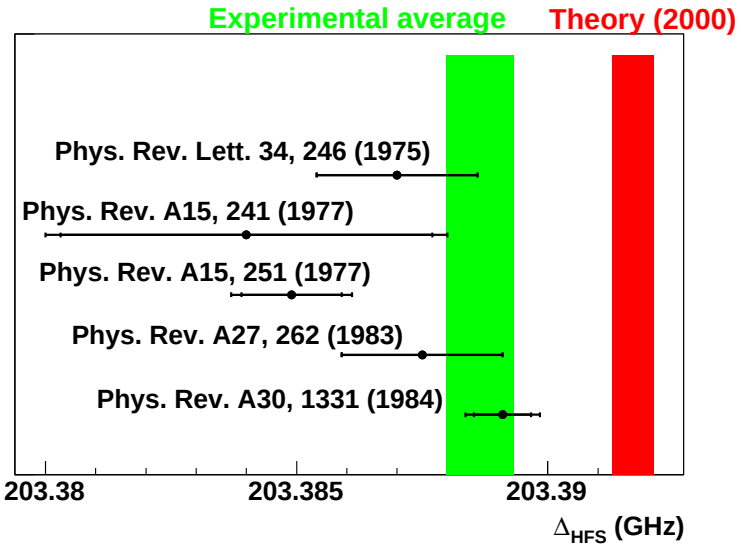

Figure 1.8: Historical plot of the Ps-HFS value. Points with error bars show the experimental results with references. The green and red bands show the average of the measured values (the average of the latest two results) and the theoretical calculation up to $O(\alpha^3\log\alpha^{-1})$, respectively.

Figure 1.8 shows a 3.9 σ (15ppm) discrepancy between the average of the most accurate two measurements (green band) and the theoretical calculation (red band). This is the third anomaly related to QED tests today. Possible reasons of the discrepancy are as follows:

1. new physics beyond the Standard Model
2. miscalculation of the theoretical value
3. common systematic uncertainties in the previous experiments

If the both QED calculation and experiment are correct, the discrepancy indicates contribution of an unknown particle. Ps-HFS is sensitive to a pseudo-scalar, a vector or an axial vector particle with a mass of 1 MeV via the virtual annihilation channel (the right figure of Fig. 1.2). To test this possible new physics, we have to check systematic uncertainties in the previous measurements. There are two possible systematic uncertainties in the previous indirect methods.

- The *non-thermalized* o-Ps becomes a source of the uncertainties not considered in the previous experiment. The previous measurement used a gas molecule as an electron donor to produce Ps. Ps-HFS in finite gas pressure is shifted by the Stark effect from electric fields of the gas molecule. One has to extrapolate Ps-HFS values of some pressure points to that of vacuum. In the previous extrapolation procedure, they assumed that the collision rate between Ps and gas molecules is proportional to the gas pressure. It means that mean velocity of Ps is the same for the various pressured gases, i.e. Ps is well thermalized in its short lifetime. It was reported that this well-thermalized assumption is not satisfied in the decay rate measurements [10] known as "o-Ps lifetime puzzle" in 1980's and 90's. At this late date, it was experimentally indicated that the non-thermalized Ps would also affect on the HFS measurement, and corrected Ps-HFS favors the theoretical calculation and disfavors the previous experimental average by 2.7 standard deviations [38]. One has to re-measure Ps-HFS in vacuum to confirm this assumption.

- Any effects related to the static magnetic field can be another source of uncertainties. One possible uncertainty is non-uniformity of the magnetic field. The formed Ps is widely spread in the microwave cavity whose size is about 20 cm in diameter (Fig. 1.7). The size of the used magnet is limited to prepare a uniform magnetic field in the region where Ps is formed. The uncertainty of the magnetic field strength directly contributes to the measured Ps-HFS value by Eq. (1.33). One possible approach is to produce a very uniform (ppm level) magnetic field by a large superconducting magnet as reported in [38]. The other way is to measure Ps-HFS without a static magnetic field.

It is necessary to verify the discrepancy with a new method. The second motivation of this thesis is to blaze a trail for re-measuring the observed discrepancy with a method totally different from previous experiments. Some independent experiments (using quantum interference [39][40][41][42], optical lasers [43], and a precise magnetic field and correcting gas effect [44][38]) have been performed, but have not yet reached a sufficient level of precision to completely address the observed discrepancy. A direct measurement of the Ps-HFS transition is the only

method free from systematic uncertainties from use of a static magnetic field. This new method firstly reported in this thesis will be a future competitor to the precise measurements for addressing the discrepancy (See Sec. 4.3).

This thesis is organized as follows. Chapter 2 describes the experimental apparatus in detail. The calibration and the analysis of the measured data is described in Chapter 3. The systematic errors are considered, and the result of the measurement is shown there. In Chapter 4, the power estimation and the condition of event selections are checked. The future prospect is also described there. Finally, we conclude this thesis in Chapter 5.

Chapter 2

Experiment

2.1 Experiment Overview

Figure 2.1 shows a schematic view of our experimental setup. The experiment is performed in Research Center for Development of Far-Infrared Region in University of Fukui.

The basic principle of this experiment is as follows:

1. A gyrotron oscillator radiates a millimeter-wave Gaussian beam of power from 100 to 550 W.
2. A Fabry-Pérot resonant cavity accumulates the Gaussian beam to obtain equivalent power of over 10 kW.
3. A ^{22}Na source emits a positron, and Ps is formed inside the Fabry-Pérot resonant cavity filled with gas as an electron source.
4. Millimeter-wave radiation causes the stimulated transition from o-Ps to p-Ps,
5. An increase of 2γ rays from transiting p-Ps decays is measured with γ-ray detectors.
6. Frequency is tuned from 201 GHz to 206 GHz by changing a RF cavity in the gyrotron oscillator to measure the cross-section of the Ps-HFS transition.

This chapter is organized as follows. First, an optical system composed of a gyrotron oscillator and a Fabry-Pérot resonant cavity are described. A power estimation method of the Fabry-Pérot cavity is described next. A procedure of power stabilization is also described. Then, a Ps formation assembly and γ-ray detectors are described. Special concern is required for gas selection. Finally, electronics and a data acquisition system are described.

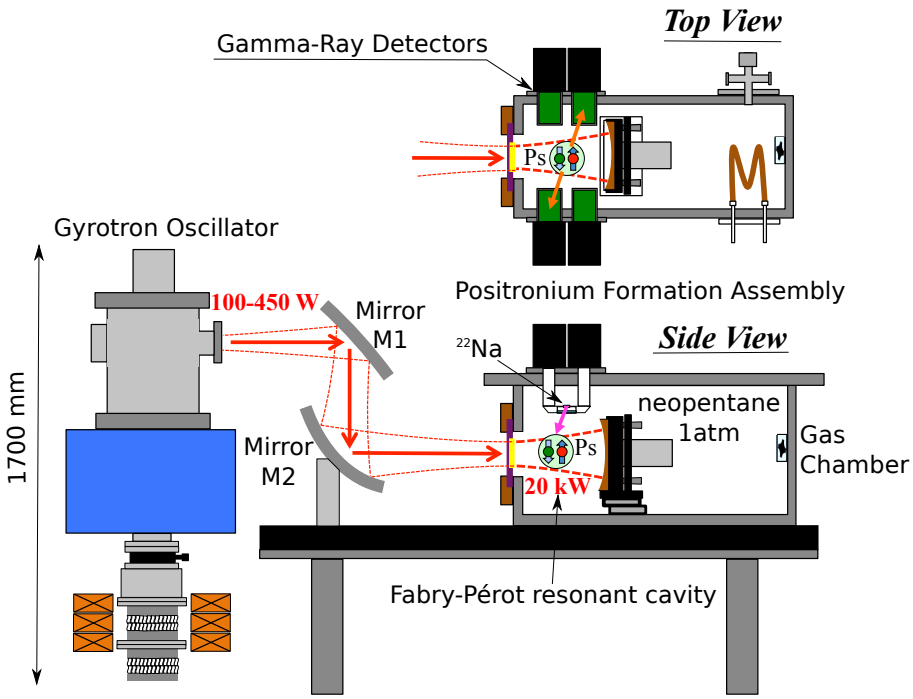

Figure 2.1: Schematic view of our experimental setup.

2.2 Millimeter-wave Optics System

2.2.1 Gyrotron Oscillator

This experiment needs high power ($> 100\,\mathrm{W}$), monochromatic ($< 0.1\%$), and high-duty ($> 30\%$) millimeter waves. The only solution today is a gyrotron oscillator.

Principle of gyrotron oscillator

A gyrotron oscillator is one of the cyclotron-resonance-maser fast wave devices [45][46][47]. It is not an amplifier but a self-exciting oscillator of millimeter waves. Gyrotron oscillation is caused by transitions between inversely distributed Landau levels of gyrating electrons instead of atomic energy levels used in another maser device. Since quantum mechanical treatment is not practical, a gyrotron theory is usually understood classically. A classical theory of gyrotron is described in Appendix. A. In this section, a highlight of the gyrotron mechanism is described.

Figure 2.2 shows a schematic view of the gyrotron oscillator used in this experiment (FU CW G1). The gyrotron is composed of three parts: an RF cavity (it is not a radio wave but is conventionally called RF) in a superconducting solenoid, a

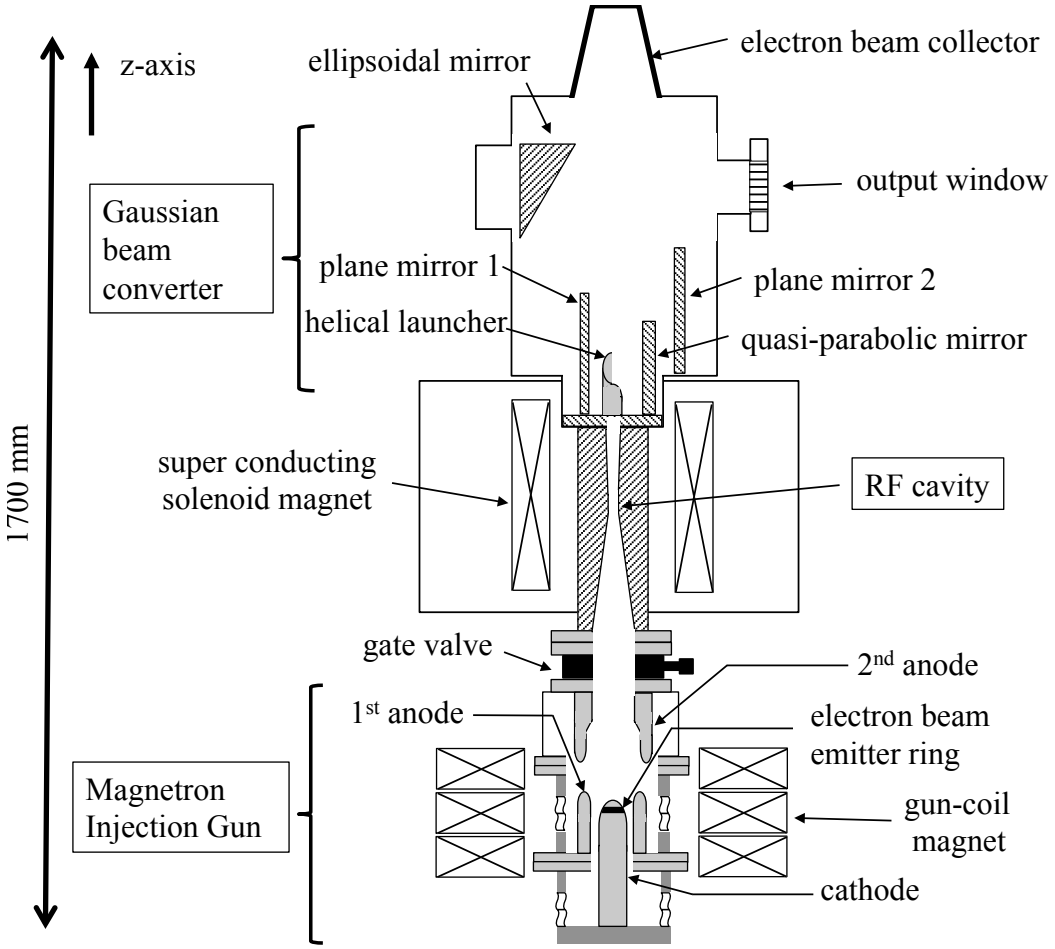

Figure 2.2: Schematic view of the gyrotron oscillator FU CW G1.

Magnetron Injection Gun (MIG), and a Gaussian beam converter. These all are in high vacuum (about 10^{-5} Pa). Electrons are emitted at an electron beam emitter applied high voltage (cathode voltage $V_\mathrm{k} = -18$ kV), and its trajectory is controlled with a gun-coil magnet ($\sim$0.1 T), and 1$^\mathrm{st}$ anode voltage ($\sim$10 kV). Electrons are gyrating in the RF cavity where a magnetic field B_0 is induced.

Figure 2.3 shows a cross-sectional view of electrons at the RF cavity. The cyclotron angular frequency of an electron is expressed as

$$\omega_\mathrm{c} = \frac{eB_\mathrm{z}}{m_\mathrm{e}\gamma} = \frac{\Omega_0}{\gamma}, \tag{2.1}$$

where $\gamma = 1/\sqrt{1-(v/c)^2}$ (v is velocity of the electron) is the Lorentz factor of an electron. The electron beam of current I_b is cylindrically distributed with radius R_b corresponding to the shape of the emitter ring at the MIG. The Larmor radius

(gyrating radius) is expressed as

$$r_{\mathrm{L}} = \frac{v_{\perp}}{\omega_{\mathrm{c}}}, \tag{2.2}$$

which is small enough compared with R_{b} and its thickness. Electrons are in cyclotron motion at random phase ψ because they are thermally emitted from the emitter.

Gyrating electrons and electric fields in RF cavity (radius 5 mm, length 24 mm) interact with each other according to Maxwell's equations and the Lorentz force. The interaction excites strong millimeter-wave radiation (100-550 W) of a waveguide mode ($\mathrm{TE_{mn}}$ mode). Radius of the RF cavity and an excited mode ($\mathrm{TE_{52}}$ mode in this experiment) determine output frequency. A waveguide mode is converted to a bi-Gaussian beam by the Gaussian beam converter and is output from a window.

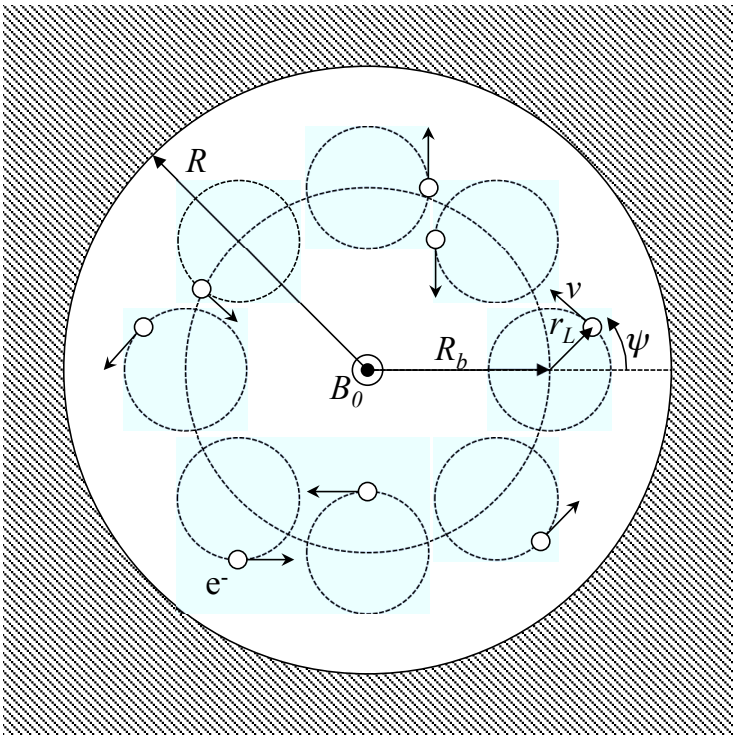

Figure 2.3: Schematic of an annular electron beam in the RF cavity.

Figures in Fig 2.4 demonstrate the interaction between electrons and the RF field. Note that electrons are in momentum space here (they are in real space in Fig. 2.3). We introduce relative phase θ between the electric field and the electron momentum. At the entrance of the cavity $z = 0$ mm, momenta of electrons are in random phase θ because of thermal emission from the MIG. They all have the

same energy (normalized as unity) determined by cathode voltage. When electrons start to interact with the RF field at the entrance of the RF cavity ($z = 6$ mm), some electrons are accelerated (gain energy, or outside the circle of radius 1 in the left of Fig. 2.4), and the others are decelerated (lose energy, or inside the circle) corresponding to their initial phases. Because of the Lorentz factor in cyclotron angular frequency ω_c in Eq. (2.1), ω_c of accelerated electron *decreases* while that of decelerated electron *increases*.

If RF frequency ω_r is slightly higher than the initial value of the cyclotron frequency ω_c, ω_c of only decelerated electrons moves closer to exact resonance with the RF field, thereby losing an increasing amount of energy on each successive cycle. It is clearly seen that automatic bunching to the deceleration phase occurs at $z = 12$ mm (center of the RF cavity) in Fig. 2.4. Finally, at $z = 20$ mm, the end of the interaction region in the RF cavity, most electrons lose initial energy as shown in the right figure. The RF field ideally gains 30% of initial energy of the electron beam. This is the principle of gyrotron oscillation, and a classical interpretation of cyclotron-maser-resonance.

Let us summarize the excitation condition of the gyrotron oscillator:

- Use (weakly) a relativistic electron beam
- Set magnetic field strength so that relativistic cyclotron frequency is slightly smaller than resonance frequency of the RF cavity

The remarkable feature of the gyrotron oscillator is using the relativistic effect of the electron cyclotron motion. The phase bunching itself occurs even if electrons are non-relativistic. However, non-relativistic electrons can never bunch to the *deceleration* phase, and does not excite millimeter-wave radiation in gyrotron operation.

The difference between cyclotron frequency and RF frequency is called frequency detuning. Frequency detuning determines non-linearity of gyrotron oscillation. Excitation efficiency is a single-valued function of electron-beam current I_b in case of small frequency detuning. Output power increases as I_b increases, which is called soft excitation. However, if frequency detuning is large, excitation efficiency is a multivalued function of I_b, which is called hard excitation. High efficiency is obtained in the hard excitation condition (See Appendix A.5). In our case, operation condition is soft but nearly hard excitation, and results in non-trivial behavior of output power. In case of hard excitation, power starts to be output at large electron-beam current, and increases as I_b *decreases* for a while. Then, power increases as I_b *increases* (See Fig. A.8 for detail). A gyrotron determines its plasma interaction, and one controls parameters to the required value. Thus, it is very difficult to set output power as a target of feedback controls and stabilize output power for a long time (one week). Details of power-stabilization procedure are described in Sec. 2.2.4

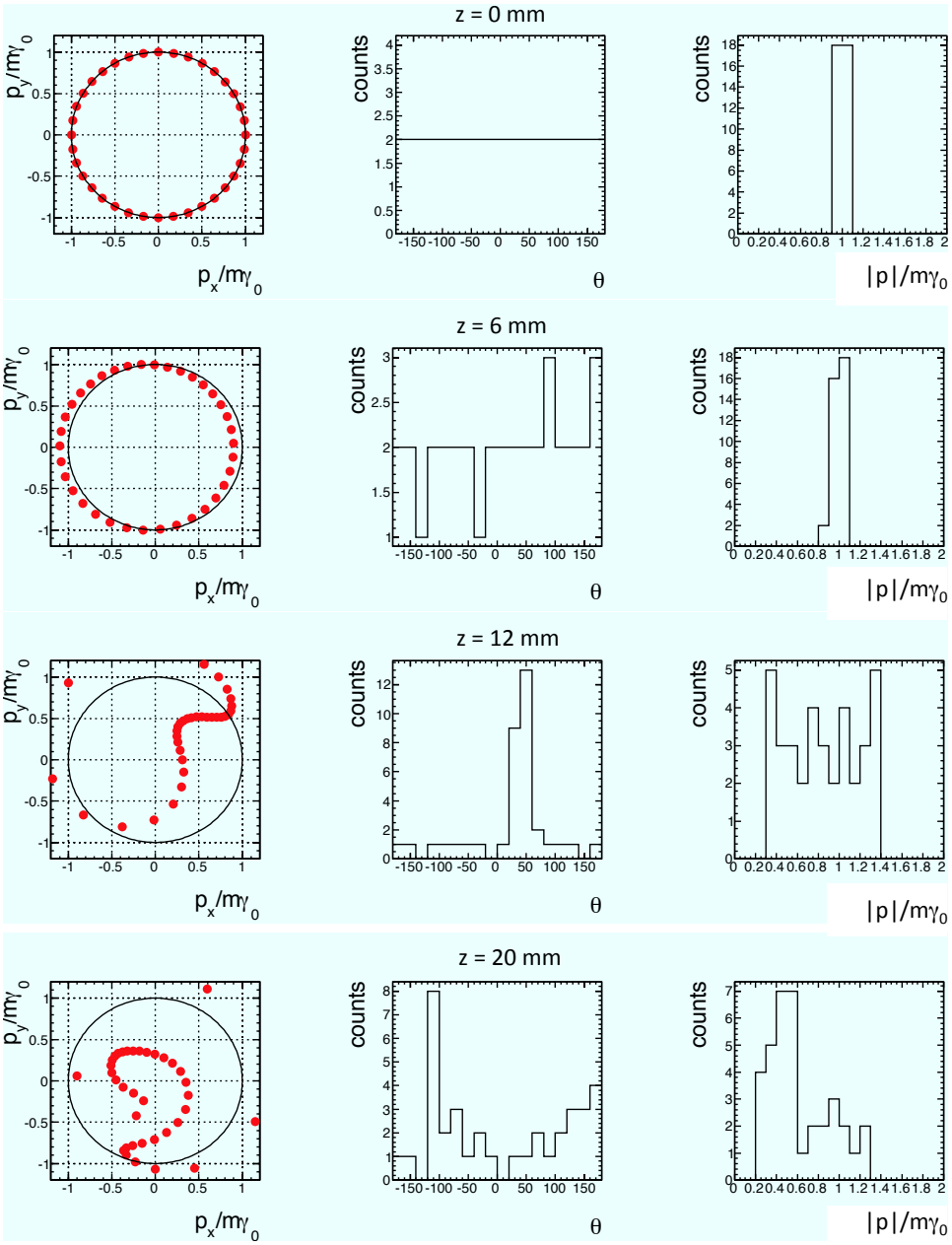

Figure 2.4: Simulated interaction between electrons and the RF field. Electron's momenta are calculated at $z = 0, 6, 12, 20$ mm in the RF cavity (see Fig. A.1 and Fig. A.3) with cathode voltage $V_\mathrm{k} = -18$ kV, electron-beam current $I_\mathrm{b} = 500$ mA, magnetic field strength $B_0 = 7.4$ T, cavity radius $R_2 = 2.475$ mm, beam radius $R_\mathrm{b} = 0.7 \cdot R_2$, and pitch factor $= 1.2$. Output power $P_\mathrm{out} = 2.5$ kW. The left figures show normalized momenta of electrons initially in random phase. The middle figures show histograms of electron phase. The right figures show normalized electron energy decreasing as passing through the RF cavity (the electromagnetic field gains energy).

Property of FU CW G1

Figure 2.5 shows a photograph of the gyrotron (FU CW G1) developed specifically for this measurement [48]. Operation parameters of FU CW G1 are summarized in Table 2.1. Table 2.2 summarizes strength of the superconducting magnetic field, frequency, and power of each cavity radius. Cathode voltage is fixed during the experiment. Strength of the superconducting magnetic field is adjusted to the value determined by the cavity radius. 1^{st} Anode voltage and the gun-coil magnetic field is controlled depending on the situation to stabilize output power and line-width, frequency drift.

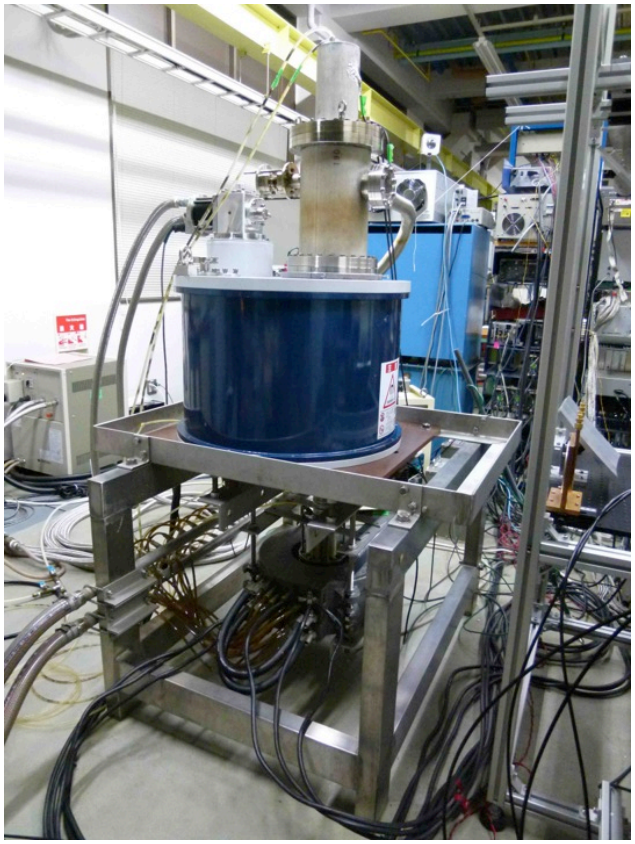

Figure 2.5: Photograph of FU CW G1.

Output power was measured with a calorimeter, which is a 46 ml water pool in a thin Teflon case. A temperature increase of water was measured with a resistance thermometer Pt100. The calorimeter was placed at angle about 45° to prevent a reflected beam from going back to the RF cavity because the reflected beam makes a standing wave, and also interferes electron interaction in the RF cavity to reduce accuracy of the power estimation (See Sec. 2.2.3). Expected output power is from 1 kW to 2 kW, while measured power was less than 600 W, and also varied by

Cathode voltage	-18 kV
1^{st} Anode voltage	$-8 \sim -11$ kV
2^{nd} Anode voltage	GND
Gun coil magnetic field	0.1∼0.14 T
Beam current	300∼400 mA
Repetition rate	5 Hz
Duty ratio	30 %

Table 2.1: Operation parameters of FU CW G1.

mode	R_2 [mm]	B_0 [T]	f_{calc}	Q_{calc}	f_{meas}	Δf [MHz]	P [W]
TE_{42}	2.453	6.57	180.76	2080	180.56	100	300
TE_{52}	2.481	7.35	202.51	2400	201.83	20	190
TE_{52}	2.475	7.37	203.00	2450	202.64	20	240
TE_{52}	2.467	7.37	203.66	2500	203.00	40	550
TE_{52}	2.467	7.37	203.66	2500	203.25	50	250
TE_{52}	2.463	7.42	203.99	2530	203.51	20	350
TE_{52}	2.453	7.43	204.82	2600	204.56	50	410
TE_{52}	2.443	7.48	205.65	2650	205.31	40	125

Table 2.2: Operating points used for this measurement.

factor of four depending on the cavity. Condition of gyrotron oscillation is very sensitive to the fabrication accuracy of the RF cavity, quality of the emitter surface of the MIG, and alignment between the cavity and the magnetic field. In general, it is difficult to reproduce the same condition for all gyrotron operations [49] (See Appendix A.6 for detail).

Output frequency was measured with hetero-dyne technique using a synthesizer (∼12 GHz) as a local oscillator. An even harmonic mixer (Virginia Diodes, WR5.1EHM) made of a Schottky barrier diode was used. When we denote gyrotron frequency as f_{RF}, synthesizer frequency as f_{LO}, and harmonic number as n, intermediate frequency (IF) is expressed as

$$f_{\mathrm{IF}} = |f_{\mathrm{RF}} - n f_{\mathrm{LO}}| \,. \tag{2.3}$$

f_{IF} was measured with an oscilloscope, and analyzed on-line with Fast Fourier Transform (FFT). Lower Side Band (LSB) corresponds to IF when $nf_{\mathrm{LO}} < f_{\mathrm{RF}}$, and Upper Side Band (USB) does when $f_{\mathrm{RF}} < nf_{\mathrm{LO}}$. Note that small LSB at the same LO means small RF. A harmonic number $n = 16$ was selected to monitor RF. Output power of the synthesizer for optimum measurement was from 9 dBm to 11 dBm. According to Table 2.2, measured frequency f_{meas} is always smaller than expected one f_{calc} by a few 100 MHz. Thermal expansion of cavity radius may cause the frequency shift in steady state operation of the gyrotron.

Figure 2.6 shows an example of measured FFT spectra of f_{IF} of LSB. Each line shows a FFT spectrum at different time in one gyrotron pulse duration. Measured frequency line-width is more than 2 MHz, and is drifted randomly about 20 MHz. Since these effects are very small (<100 ppm), and gyrotron operation is in principle complicated plasma interaction, many reasons are considered to explain these phenomena. The line-width may be due to large velocity spread $\Delta v_{//}$ of the electron beam or interaction with reflected electromagnetic waves [50][51]. The frequency drift may be due to voltage depression by space charge or thermal expansion of cavity radius in one pulse [52]. At the present stage of gyrotron technology, they are inevitable and result in a systematic error. Fortunately, it is small enough compared with present level of accuracy needed in this thesis (0.1% or 200 MHz). Better line-width and drift is needed to address the observed discrepancy (15 ppm or 3 MHz) in the future. This technical improvement is feasible because one reported that line-width of a low frequency (< 170 GHz) gyrotron is better than 100 kHz [22].

In order to measure the cross-section curve of the Ps-HFS transition, input radiation should be scanned from 201 GHz to 206 GHz. As shown in table 2.2, this was achieved by changing a gyrotron cavity with different radius R_2. A gate valve was inserted between the cavity section and the MIG (Fig. 2.2) not for an emitter surface to be exposed to air during the cavity replacement. It took more than 1 week after the replacement to flush the emitter, bake the cavity, carefully align all elements, and search for the best operation parameters. One exception is $f_{\mathrm{meas}} = 180.56$ GHz, where the operation mode is TE_{42} with the same cavity radius as the $f_{\mathrm{meas}} = 204.56$ GHz point to obtain a far off-resonant point.

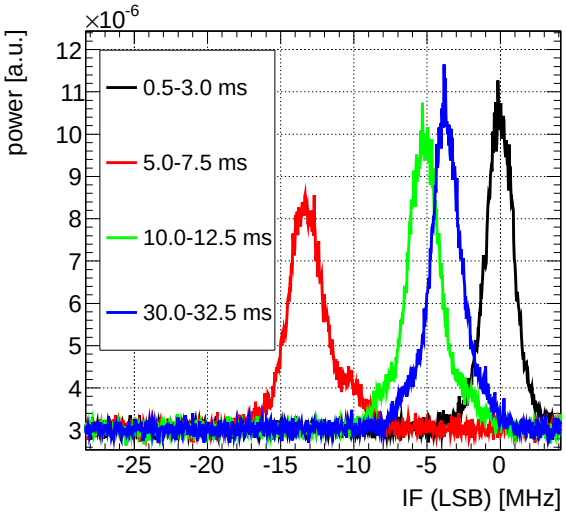

Figure 2.6: Measured frequency spectra of FU CW G1. IF of LSB is shown. Different lines correspond to different delay time from the rising edge of pulse. A time range for FFT is 2.5 ms. One spectrum is a result of the average of 100 cycles.

Output radiation from the window is designed to be a bi-Gaussian beam (See Appendix A.7). Power distribution of the bi-Gaussian was predicted with a Kirchhoff integral method as shown in Fig. 2.8. The horizontally long distribution changes to vertically long one during the propagation. Power distribution was measured with a temperature increase of a thin (1 mm) polyvinyl chloride plate (PVC). Figures 2.9 show photographs of PVC taken with an Infrared (IR) camera. Measured power distribution is in good agreement with the prediction. Parameters of the beam are beam waist size $(w_{\mathrm{x}}, w_{\mathrm{y}}) = (15.1\,\mathrm{mm}, 8.4\,\mathrm{mm})$ and beam waist position from the output window $(z_{0\mathrm{x}}, z_{0\mathrm{y}}) = (-102.7\,\mathrm{mm}, 56.8\,\mathrm{mm})$

The bi-Gaussian beam is converted to a Gaussian beam with toroidal mirrors according to the Gaussian lens formula [23]. One should pay attention that focus points are different depending on two curvature radius R_1 and R_2 as shown in Fig. 2.7. When the beam is reflected by a toroidal mirror at a reflection angle θ, focus points F_1 and F_2 are

$$F_1 = R_1 \frac{\cos\theta}{2} \tag{2.4}$$

$$F_2 = R_2 \frac{1}{2\cos\theta}. \tag{2.5}$$

Two mirrors M1 (R_1 = 2902 mm, R_2 = 1776 mm) and M2 (R_1 = 679 mm,

R_2 = 1482 mm) made of aluminum are shown in Fig.2.1. The reflection angle is fixed at 45°. M1 is placed at a distance of 550 mm from the output window, and M2 is placed 600 mm from M1. A new beam waist (size w_0 = 8.4 mm) is designed to be at 600 mm from M2, where the input side mirror of the Fabry-Pérot resonant cavity is placed. Figures 2.10 show measured power distribution of the converted beam. The beam is almost a perfect Gaussian beam, and efficiently couples to Fabry-Pérot resonant cavity.

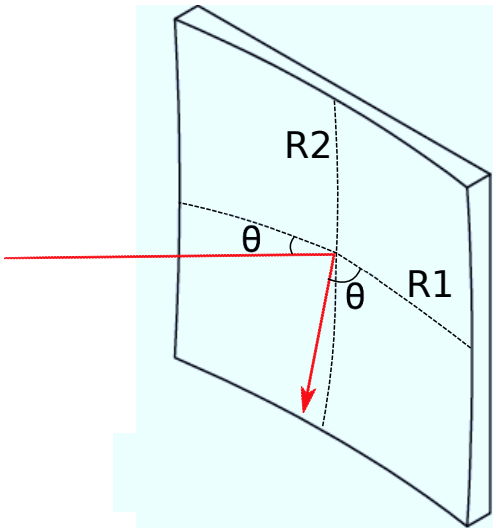

Figure 2.7: Schematic view of toroidal mirror.

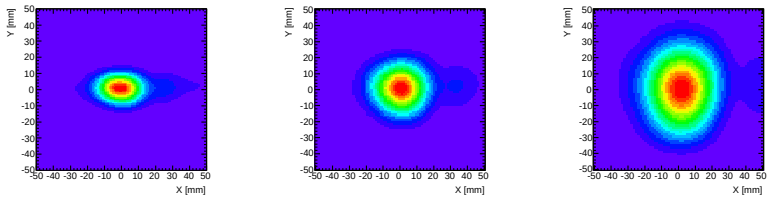

Figure 2.8: Calculated output pattern of FU CW G1. Left figure is power distribution at 200 mm from the output window. Middle figure is at 400 mm. Right figure is at 700 mm.

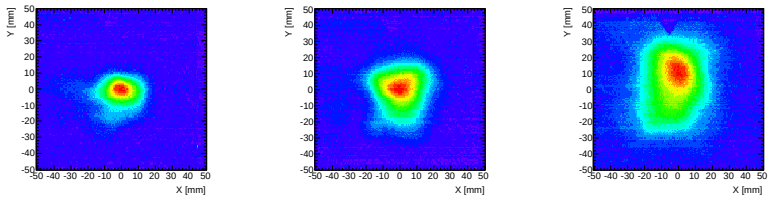

Figure 2.9: Measured output pattern of FU CW G1. Left figure is power distribution at 200 mm from the output window. Middle figure is at 400 mm. Right figure is at 700 mm.

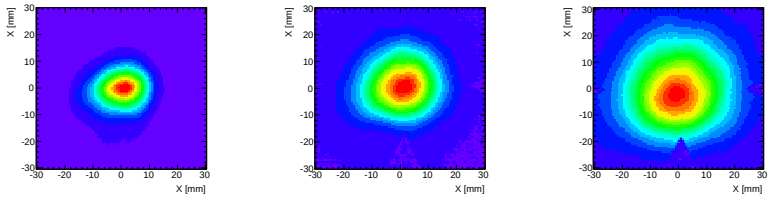

Figure 2.10: Measured power distribution of Gaussian beam. Left figure is power distribution at 600 mm from M2. Middle figure is at 750 mm. Right figure is at 900 mm.

2.2.2 Fabry-Pérot Resonant Cavity

Output of the gyrotron is at most 550 W, and the Ps-HFS direct transition needs over 10 kW. A Fabry-Pérot resonant cavity is developed to obtain such high equivalent power. In this section, a general theory of this resonant cavity is derived, and then specific problems for millimeter-wave radiation are discussed.

Theory of the Fabry-Pérot resonant cavity

A Fabry-Pérot resonant cavity is composed of two parallel mirrors. Figure 2.11 shows a schematic view of the cavity. An electromagnetic wave whose electric field is denoted as $E_{\rm in}$ is introduced from the left-hand side. A front mirror (left hand side) is a half mirror of which the reflection coefficient of amplitude is r_f and transmission one is t_f. For simplicity, r_f and t_f are assumed to be independent of the propagation direction. A right-bound propagating wave in the cavity is denoted as E_r and a left-bound one is denoted as E_l. A reflected wave from the cavity is $E_{\rm re}$. An end mirror (right hand side) whose reflection coefficient is r_e has a very small transmission t_e to sample E_r. A transmitted wave is denoted as $E_{\rm tr}$. Boundary conditions for these electric fields are

$$E_{\rm tr}(d) = t_e E_r(d), \tag{2.6}$$
$$E_{\rm re}(0) = -r_f E_{\rm in}(0) + t_f E_l(0). \tag{2.7}$$

Note that the negative signs come from phase shift of π by reflection at each mirror.

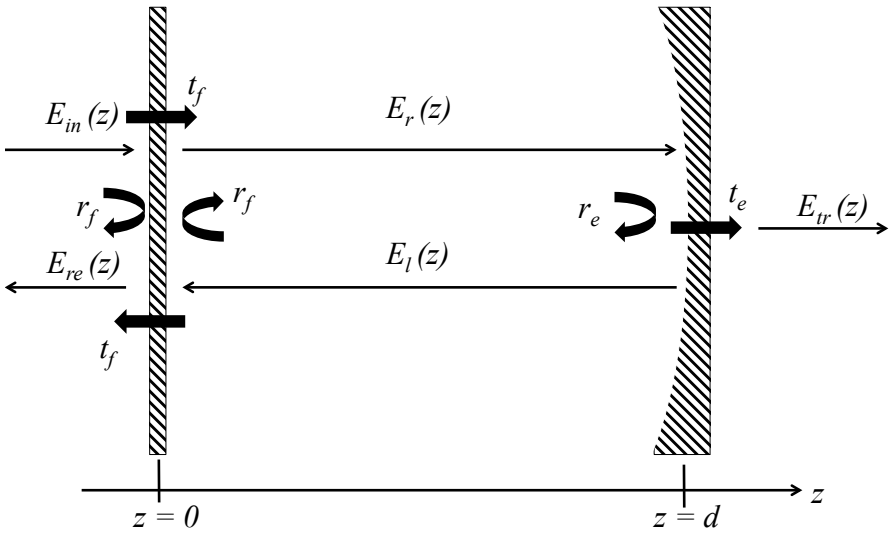

Figure 2.11: Schematic view of a Fabry-Pérot resonant cavity.

Let us consider the simplest case, a monochromatic plane wave (angular frequency ω and wave number k) case. The right-bound propagating wave in the

cavity can be expressed as

$$E_r(z) = t_f E_{\rm in}(0) e^{ikz} \sum_{j=0}^{\infty} \left[r_e r_f e^{2ikd} \right]^j = \frac{t_f E_{\rm in}(0) e^{ikz}}{1 - r_f r_e e^{2ikd}}. \tag{2.8}$$

In the same way, the left-bound propagating wave in the cavity is

$$E_l(z) = t_f r_e E_{\rm in}(0) e^{-ik(z-2d)} \sum_{j=0}^{\infty} \left[r_e r_f e^{2ikd} \right]^j = \frac{t_f r_e E_{\rm in}(0) e^{-ik(z-2d)}}{1 - r_f r_e e^{2ikd}}. \tag{2.9}$$

According to the boundary conditions Eq. (2.6), (2.7), the transmitted wave and the reflected wave can be calculated as

$$E_{\rm tr}(z) = t_e E_r(d) e^{ik(z-d)} = \frac{t_f t_e}{1 - r_f r_e e^{2ikd}} E_{\rm in}(0) e^{ikz} \tag{2.10}$$

and

$$E_{\rm re}(z) = \left[-r_f E_{\rm in}(0) + t_f E_l(0) \right] e^{-ikz} = \left[-r_f + \frac{t_f^2 r_e e^{2ikd}}{1 - r_f r_e e^{2ikd}} \right] E_{\rm in}(0) e^{-ikz}, \tag{2.11}$$

respectively.

Using power reflection coefficients $R_f = r_f^2$, $R_e = r_e^2$ and transmission coefficients $T_f = t_f^2$, $T_e = t_e^2$, transmitted power $P_{\rm tr} \propto |E_{\rm tr}|^2$ and reflected power $P_{\rm re} \propto |E_{\rm re}|^2$ are expressed as

$$\frac{P_{\rm tr}}{P_{\rm in}} = \frac{T_f T_e}{(1 - \sqrt{R_f R_e})^2} \frac{1}{1 + F \sin^2 kd}, \tag{2.12}$$

$$\frac{P_{\rm re}}{P_{\rm in}} = \frac{\left[\frac{\sqrt{R_f} - (T_f + R_f)\sqrt{R_e}}{1 - \sqrt{R_f R_e}} \right]^2 + (T_f + R_f) F \sin^2 kd}{1 + F \sin^2 kd}. \tag{2.13}$$

where $P_{\rm in} \propto |E_{\rm in}|^2$ is input power from the gyrotron oscillator, and F is defined as

$$F = \frac{4\sqrt{R_f R_e}}{(1 - \sqrt{R_f R_e})^2}. \tag{2.14}$$

This cavity resonates in the case that cavity length d is half-integer multiple of wavelength λ ($k = 2\pi/\lambda$) as shown in Fig. 2.12.

One does not know the reflection and transmission coefficients of each mirror which determine property of the cavity. Two *observable* parameters are introduced in stead of these coefficients. The first one is finesse $\mathcal{F}$ defined as

$$\mathcal{F} = \frac{\pi}{2} \sqrt{F} \sim \frac{2\pi}{1 - R_f R_e}. \tag{2.15}$$

Using Full Width at Half Maximum (FWHM) of P_{tr} at one resonance, $\mathcal{F}$ can be obtained as

$$\mathcal{F} = \frac{\pi}{\mathrm{FWHM\,[radian]}} = \frac{\mathrm{FSR\,[\mu m]}}{\mathrm{FWHM\,[\mu m]}}, \tag{2.16}$$

where FSR is Free Spectral Range which means a separating distance of resonances as shown in Fig.2.12. Note that $\mathcal{F}$ is related to cavity quality factor Q and number of axial nodes n

$$\mathcal{F} = \frac{Q}{n}. \tag{2.17}$$

The other parameter is an input coupling coefficient β. To define β, we introduce an input reflection coefficient $|\rho_{\mathrm{in}}|$ defined as

$$|\rho_{\mathrm{in}}| = \frac{\sqrt{P_{\mathrm{re}}(\text{on resonance})}}{\sqrt{P_{\mathrm{re}}(\text{off resonance})}} = \frac{\dfrac{\sqrt{R_f} - (T_f + R_f)\sqrt{R_e}}{1 - \sqrt{R_f R_e}}}{\dfrac{\sqrt{R_f} + (T_f + R_f)\sqrt{R_e}}{1 + \sqrt{R_f R_e}}}. \tag{2.18}$$

Then, β is expressed as

$$\beta = \frac{1 - |\rho_{\mathrm{in}}|}{1 + |\rho_{\mathrm{in}}|} < 1 \qquad \text{(under coupling)} \tag{2.19}$$

$$\beta = \frac{1 + |\rho_{\mathrm{in}}|}{1 - |\rho_{\mathrm{in}}|} > 1 \qquad \text{(over coupling)}. \tag{2.20}$$

β corresponds to effective power input into the resonator, and is obtained by measuring reflected power. One should determine under or over coupling before calculating β.

Cavity gain is expressed as a function of finesse $\mathcal{F}$ and coupling β. At first, round-trip reflectance ρ is introduced as a function of $\mathcal{F}$

$$\rho(\mathcal{F}) = R_f R_e = \left[\left(1 + \frac{\pi^2}{2\mathcal{F}^2}\right) - \sqrt{\frac{\pi^2}{2\mathcal{F}^2}\left(1 + \frac{\pi^2}{2\mathcal{F}^2}\right)}\right]^2 \sim 1 - \frac{2\pi}{\mathcal{F}}. \tag{2.21}$$

The last approximation is valid if $\mathcal{F} >> 1$ i.e. $\rho \sim 1$. If we assume under coupling, ratio T_f/R_f is expressed as a function of β and ρ

$$\frac{T_f}{R_f} = \frac{1}{\sqrt{\rho(\mathcal{F})}} \frac{\beta\,[1 - \rho(\mathcal{F})]}{1 + \beta\sqrt{\rho(\mathcal{F})}} \tag{2.22}$$

Next, accumulated equivalent power P_{acc} inside the cavity can be expressed as

$$\frac{P_{\mathrm{acc}}(z)}{P_{\mathrm{in}}} = \frac{|E_r + E_l|^2}{|E_{\mathrm{in}}|^2} = T_f \frac{\left(\frac{1+\sqrt{R_e}}{1-\sqrt{R_f R_e}}\right)^2 - \frac{1}{\sqrt{R_f}} F \sin^2 k(z-d)}{1 + F \sin^2 kd} \tag{2.23}$$

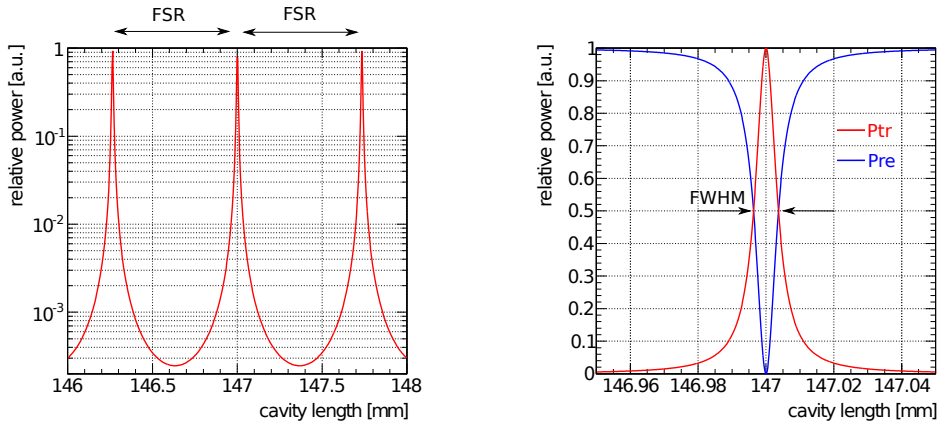

Figure 2.12: Calculated resonances of the Fabry-Pérot resonant cavity. The left shows neighboring resonances. The right represents comparison of $P_{\rm tr}/P_{\rm in}$ (red line) and $P_{\rm re}/P_{\rm in}$ (blue line). λ is 1.47 mm, $\mathcal{F}$ is 100, and β is 1 (critical coupling).

Cavity gain G at resonance is defined by averaging accumulated power $\langle P_{\rm acc}\rangle$

$$G = \frac{\langle P_{\rm acc}\rangle}{P_{\rm in}}\bigg|_{\rm reso} = \frac{1}{d}\int_0^d T_f \frac{\left(\frac{1+\sqrt{R_e}}{1-\sqrt{R_f R_e}}\right)^2 - \frac{1}{\sqrt{R_f}} F\sin^2 k(z-d)}{1+F\sin^2 kd} dz\bigg|_{\rm reso} \tag{2.24}$$

$$= \frac{T_f}{1+F\sin^2 kd}\left[\left(\frac{1+\sqrt{R_e}}{1-\sqrt{R_f R_e}}\right)^2 - \frac{2\sqrt{R_e}}{(1-\sqrt{R_f R_e})^2}\left(1+\frac{\sin 2kd}{2kd}\right)\right]\bigg|_{\rm reso}$$

$$\sim \frac{T_f(1+R_e)}{(1-\sqrt{R_f R_e})^2}. \tag{2.25}$$

The last approximation is valid if cavity length d is much longer than wavelength. From Eq. (2.21) and Eq. (2.22), we obtain

$$G(\mathcal{F},\beta) = \frac{\sqrt{\rho(\mathcal{F})}}{(1-\sqrt{\rho(\mathcal{F})})^2}\frac{\beta\left[1-\rho(\mathcal{F})\right]}{1+\beta\sqrt{\rho(\mathcal{F})}}\left(1+\frac{1}{R_e}\right). \tag{2.26}$$

If the resonance is over coupling, just replace β with $1/\beta$. Since R_e is usually very close to unity, cavity gain can be uniquely determined by observable $\mathcal{F}$ and β.

So far, we considered response of a Fabry-Pérot cavity against a plane wave. In order to stabilize resonance, the cavity should resonate a Gaussian beam [23]. The cavity has a plane mirror (front mirror) and a concave mirror (end mirror). A Gaussian beam is uniquely determined if beam waist size w_0 and its position are

given. The waist position is at plane mirror, and w_0 is expressed as

$$w_0 = \sqrt{\frac{\lambda}{\pi}\sqrt{d(R-d)}}, \tag{2.27}$$

where R denotes curvature radius of the end mirror and d does cavity length. Resonance has low diffraction loss if condition

$$0 < \left(1 - \frac{d}{R}\right) < 1 \tag{2.28}$$

is fulfilled. A Fabry-Pérot cavity also couples to higher order Gaussian beams (Hermite-Gaussian beam). Input beam should be shaped (for instance with toroidal mirrors) and carefully aligned (with accuracy of 1 mm) not to excite these higher modes (*mode matching*).

Mirror design of the Fabry-Pérot resonant cavity

According to Eq. (2.26), a cavity should be optimized to have higher $\mathcal{F}$ and reasonable β. Coupling β should be near $\beta = 1$ (critical coupling), at which all power is dumped in the cavity. To achieve these conditions, reflectivity and loss of the two mirrors should be considered. The stabilization condition Eq. (2.28) should be considered.

The end mirror should have as high reflectance R_e as possible. A copper concave mirror is selected (expected R_e is 0.9985 and radius of curvature R is 300 mm). Frequency dependence of reflectance is negligible from 201 GHz to 206 GHz. The mirror has a small hole (diameter is 0.6 mm) to monitor transmitted power P_{tr}. Designed cavity length d is approximately 156 mm, which satisfies Eq. (2.28) with $R = 300$ mm.

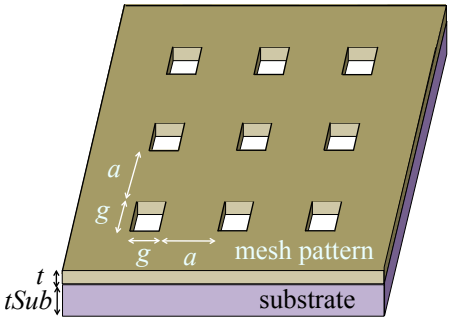

Figure 2.13: Segmental view of mesh-mirror structure on a substrate.

The front mirror is the half mirror which has high R_f and low loss $L_f = 1 - R_f - T_f$. Although in the optical range high reflectance is achieved with coating of multiple thin layers of dielectric materials, they are too lossy and useless in the millimeter-wave region. Instead, a thin mesh mirror made of gold was developed.

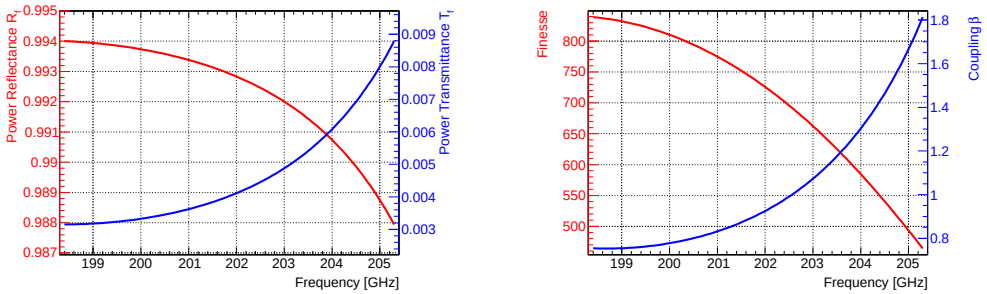

Figure 2.14: Simulated property of the mesh mirror using CST MW Studio. (left) Comparison of reflectance (red line) and transmittance (blue line). (right) Comparison of finesse (red line) and coupling (blue line).

Figure 2.13 shows a schematic view of a mesh pattern. It is a thin (thickness t) gold film with many holes, of which line width is a and gap interval is g. The mirror has high reflectivity with $g << \lambda = 1.47\,\mathrm{mm}$, and periodical holes prevent diffraction loss of a Gaussian beam at the same time. Designed t is 1 μm, which is thicker than skin depth of gold around 200 GHz (0.18 μm) and is enough thin to reduce ohmic loss when a millimeter wave passes through this mirror.

The mesh is too thin to be free-standing. It is put on a substrate with thickness $tSub$ using photo-lithography and liftoff technique. A high-resistivity silicon was selected as a base material. Its thermal conductivity (150 $\mathrm{WK^{-1}m^{-1}}$) has adequate cooling power with water cooling. A problem is that high refractive index (3.54) of silicon severely interferes reflectivity of the gold mesh. Reflectance inevitably depends on frequency. Optimization was needed to obtain reasonable cavity gain with minimum frequency dependence.

Mesh parameters (a, g, and $tSub$) were carefully optimized using CST MW Studio [53]. A plane wave was calculated with Frequency Domain Solver under periodic boundary conditions. The left side in Fig. 2.14 shows the result of the simulation, of which optimized parameters are a=200 μm, g=140 μm, and $tSub$=1960 μm (t=1 μm). According to Eq. (2.15) and Eq. (2.19), expected finesse and coupling are obtained (R_e = 0.9985) and plotted in the right side of Fig 2.14. Finesse is always over 450, and coupling is near critical ($\beta \sim 1$). Expected gain is shown in Fig. 2.15, and is about 400 around 203 GHz. Note that frequency dependence of gain is only 10% around 203.4 GHz regardless of strong frequency dependence of finesse. If input power is 300 W, accumulated power is expected to be over 100 kW. Figure 2.16 shows a photograph of the fabricated gold mesh on the silicon base. A blank space around the mesh is for water cooling. Validation of the simulation needs a resonance test of the Fabry-Pérot cavity with a cavity length control. This is described in the next section.

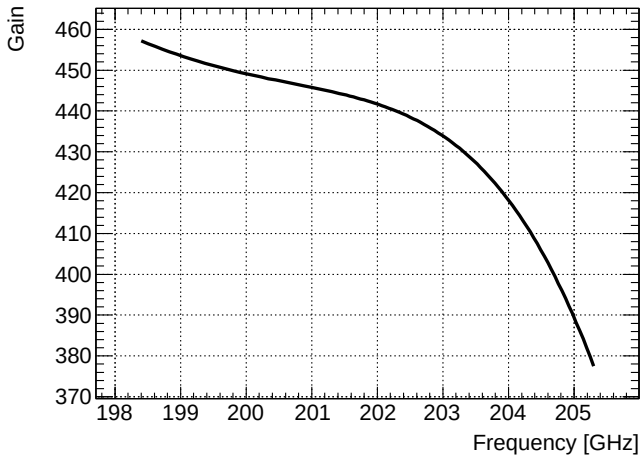

Figure 2.15: Expected Gain of the Fabry-Pérot cavity in case of plane wave input.

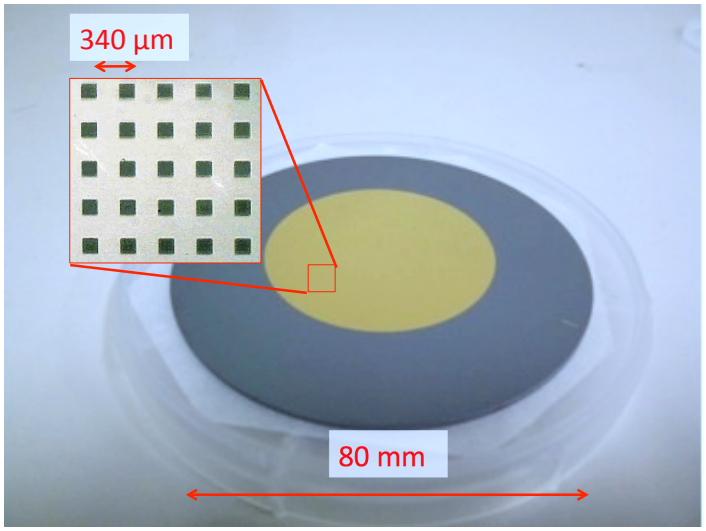

Figure 2.16: Photograph of gold mesh on silicon substrate.

Test of the Fabry-Pérot resonant cavity

A cavity length control requires a long travelling range ($\sim$ 1 mm) and high resolution ($< 1\,\mu$m) at the same time. The Fabry-Pérot cavity resonates when cavity length d is half-integer multiple of wavelength $\lambda = 1.47$ mm as shown in the left side of Fig. 2.12. One has to search the exact resonant point by changing cavity length more than FSR. Cavity length should also stay at the resonant point with precision of better than FWHM as shown in the right side of Fig. 2.12. Simulated finesse $\mathcal{F} > 450$ corresponds to FWHM of shorter than 1.5 μm.

The end mirror is mounted on a special X-axis stage which satisfies above requirements (NANO CONTROL TS102-G). It is an SIDM$^{\mathrm{TM}}$ (Smooth Impact Drive Mechanism) actuator using the piezoelectric element as a driving force. Figure 2.17 shows the principle of SIDM operation. In coarse movement, the X-stage moves like an inchworm using friction of the piezoelectric element and inertia of the X-stage to achieve 15 mm travel distance. In slight movement, the position can be controlled at a nanometer level by applying voltage to the piezoelectric element.

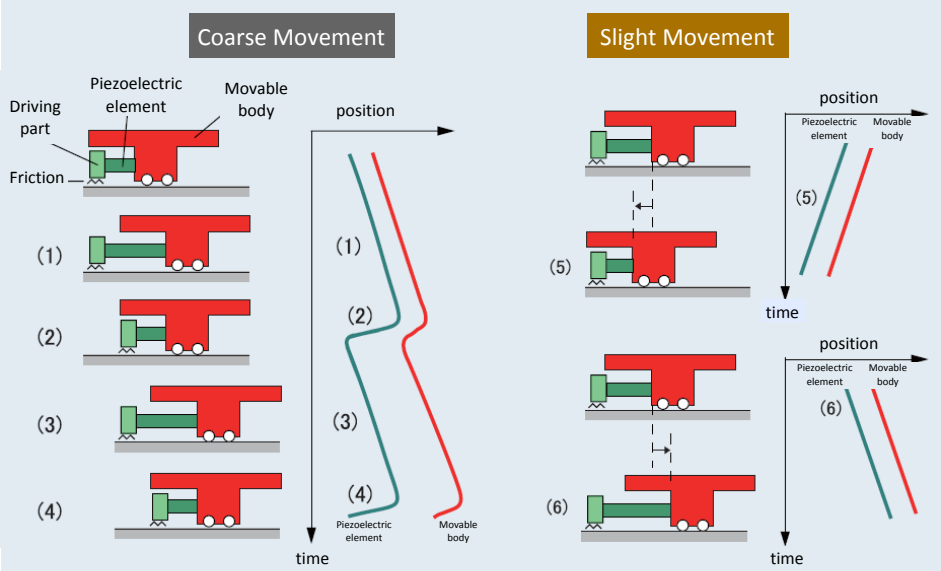

Figure 2.17: Principle of operation of an SIDM$^{\mathrm{TM}}$ (Smooth Impact Drive Mechanism) actuator.

Transmitted power P_{tr} and reflected power P_{re} should be monitored to control cavity length. There are many power sensors in the millimeter-wave region, such as a Golay cell, a Schottky barrier diode, a bolometer, and a thermopile detector. A detector should withstand 100 mW-class millimeter-wave radiation and also have a fast time response to catch up with the gyrotron pulse operation (60 ms, 5 Hz). Most of the sensors saturate or respond slowly compared with our need.

A pyroelectric detector is selected that is a thermal detector made of lithium tantalate ($LiTaO_3$) and satisfies above requirements. Lithium tantalate is a pyro-

electric crystal whose ends become oppositely charged when heated. The output current of a pyroelectric detector, which is almost proportional to a change in temperature, is converted to voltage output via an operational amplifier and a feedback resistance. A dynamic range can be controlled by changing the resistor (100 MΩ, 470 MΩ, 1 GΩ are usually used). Figure 2.18 shows a photograph of the pyroelectric detector (Spectrum Detector Inc. SPH-49). Though expected to be small, frequency dependence of the pyroelectric detector is unknown and discussed in Sec. 2.2.3.

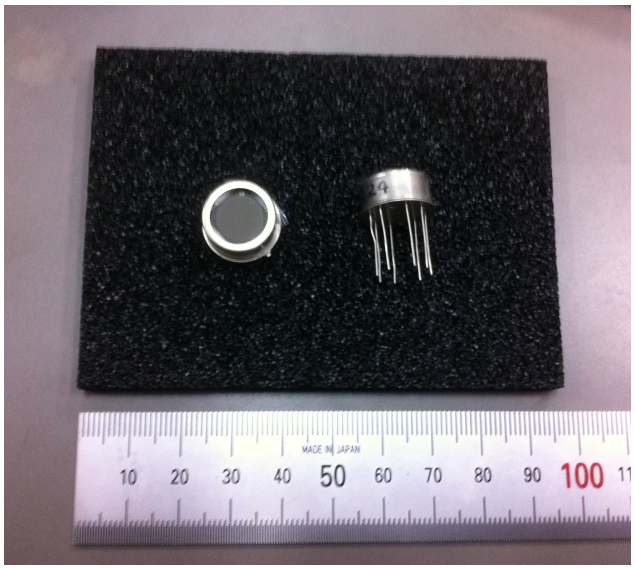

Figure 2.18: Pyroelectric detectors (Spectrum Detector Inc. SPH-49).

Figures 2.19 show a setup of the Fabry-Pérot resonant cavity including the piezoelectric stage and the pyroelectric detectors. The front mirror, optimized gold mesh, is fixed at the beam waist position of the Gaussian beam. The end mirror, copper concave mirror, is mounted on the piezoelectric stage placed 156 mm away from the front mirror. A Gaussian beam from the gyrotron is split into two ways by a beam splitter (it is not shown in Fig. 2.1). 99% of the beam goes to the Fabry-Pérot cavity, and 1% is sampled by a pyroelectric detector as an incident beam (output voltage = V_{in}). A reflected beam from the cavity is again split and sampled by another pyroelectric detector (output voltage = V_{re}). These two detectors are arranged not to reflect the beam back to the gyrotron because the reflected beam causes undesired interference. A part of accumulated power passes through a small hole (diameter is 0.6 mm, and length is 0.5 mm) at the center of the end mirror. The other pyroelectric detector measures this transmitted power (output voltage = V_{tr}).

Figure 2.20 shows a result of the resonance test at 203.7 GHz. Measured FWHM was about 1.7 μm, and according to Eq. (2.16), corresponding finesse is about

430 (expected value is 600). The coupling coefficient was 0.23 (expected value is 1.2). One cannot explain this inconsistency with either underestimation of reflectance or additional loss. It turned out that the monochromatic assumption in the theory is too ideal for the gyrotron used to test the Fabry-Pérot cavity. The line-width and drift shown in Fig.2.6 reduce effective finesse and coupling. As a result, the simulation of the mesh mirror cannot to be validated by a measurement with the current gyrotron. Moreover, the power estimation inside the Fabry-Pérot resonant cavity needs a new method instead of using the gain formula given by Eq. (2.26). This new method is described in the next section.

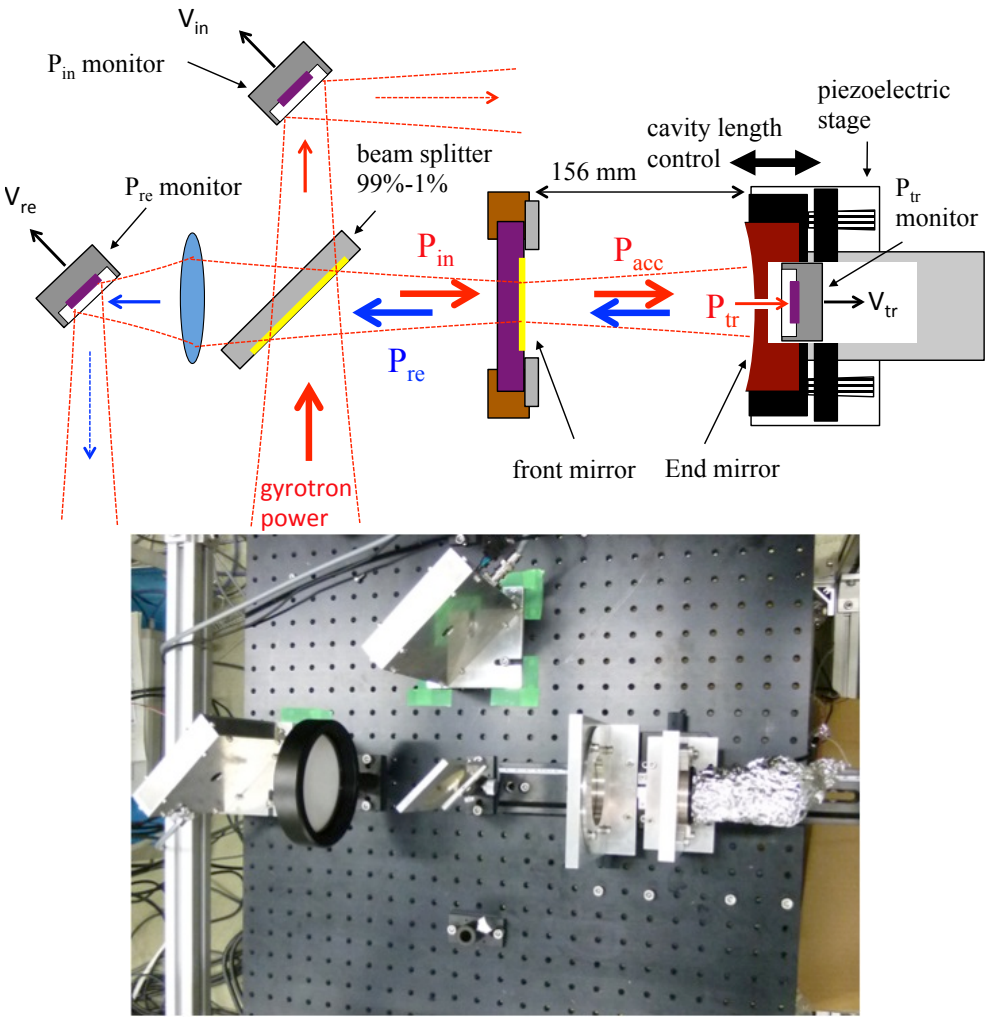

Figure 2.19: Schematic view and photograph of Fabry-Pérot cavity arrangement (top view).

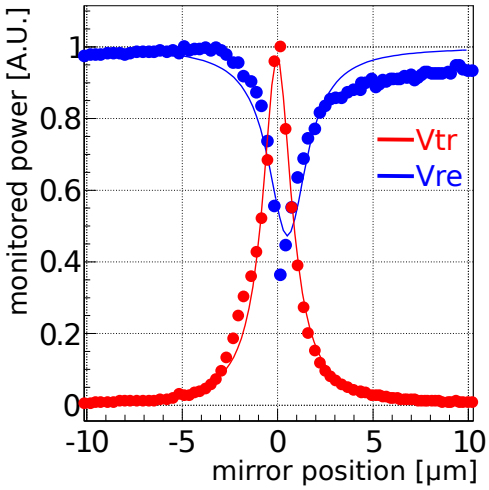

Figure 2.20: Measured resonance of the Fabry-Pérot cavity arrangement. The red points are voltage of transmitted power V_{tr}, and the blue points are that of reflected power V_{re}. The solid lines are the best fitting results of each data. The peak position is adjusted to the origin of the horizontal axis. Input frequency is 203.7 GHz.

2.2.3 Estimation of Accumulated Power

Transmitted power samples a part of accumulated power according to the boundary condition Eq. (2.6)

$$P_{\mathrm{tr}} = T_e \frac{1}{1+R_e} P_{\mathrm{acc}}. \tag{2.29}$$

This formula is valid even if input electromagnetic waves are not perfectly monochromatic. Transmittance of the end mirror through a small hole T_e is too complicated to be calculated. It is also non-trivial to estimate a response of the pyroelectric detector and interference of the transmitted beam in the base material of the detector and the end mirror. An absolute power-calibration factor C including all difficulties mentioned above is defined as

$$P_{\mathrm{acc}} = \frac{1+R_e}{T_e} P_{\mathrm{tr}} = C V_{\mathrm{tr}}. \tag{2.30}$$

C depends on frequency and is experimentally determined as follows:

- Prepare a *known* Gaussian beam with a shape correction
- Simultaneously measure V_{tr} and power of the Gaussian beam P_{in} using a chopper
- Correct reflection effects from the end mirror.

Details of the measurement are described from the next section.

Shape correction with a PVC sheet and an IR camera

The only choice of the high-power Gaussian beam is one from the gyrotron. The shape of the radiation is well converted and is almost a perfect Gaussian beam. However, it is necessary to correct shape difference mainly due to limited accuracy of millimeter-wave beam alignment (more or less 3 mm). The left figure of Fig. 2.21 shows a typical measured mode pattern, and the right figure shows a theoretical calculation. The data were fitted by bi-Gaussian, and were appeared to have larger beam waist size than the prediction by factor of 1.4 and center displacement of 1 mm. They were corrected as follows. Temperature of the fitted function at the origin T_0 was obtained, and temperature T inside three standard deviations was integrated. Then, a hole-to-beam power ratio R_{beam} was calculated as

$$R_{\mathrm{beam}} = \frac{\pi r_{\mathrm{hole}}^2 T_0}{\int_0^{2\pi} d\theta \int_0^{3\sigma} T dr}, \tag{2.31}$$

where r_{hole} denotes radius of the small hole and is 0.3 mm. Systematic errors were obtained by displacing the origin within the accuracy of alignment, 3 mm, and calculating minimum and maximum relative change of R_{beam}

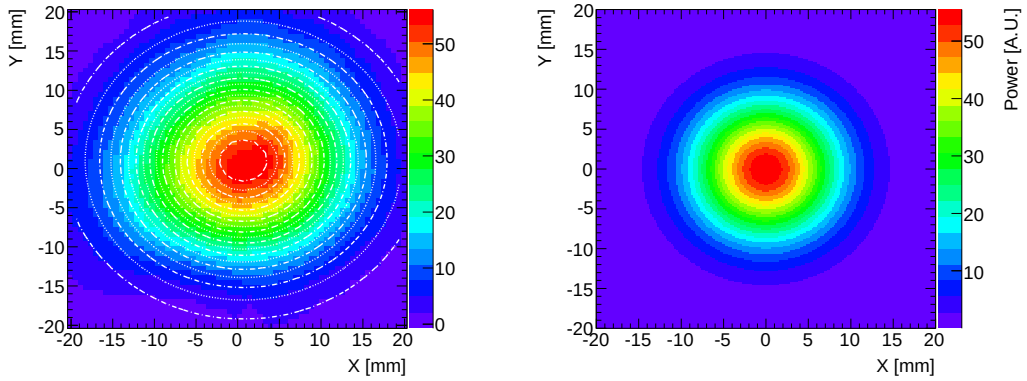

Figure 2.21: Mode pattern at the end mirror. (left) Measured mode pattern by taking temperature distribution of a PVC plate with an IR camera. White line is a fitted bi-Gaussian function. (right) Theoretical mode pattern in the Fabry-Pérot resonant cavity.

A hole-to-cavity-mode power ratio in the Fabry-Pérot cavity R_{cavity} was esti-

mated by integrating a theoretical function

$$R_{\mathrm{cavity}} = \frac{\int_0^{r_{\mathrm{hole}}} \exp\left(-2(r/w_{\mathrm{z}})^2\right) r\mathrm{d}r}{\int_0^{\infty} \exp\left(-2(r/w_{\mathrm{z}})^2\right) r\mathrm{d}r} \cdot \frac{1}{1+R_{\mathrm{e}}} \tag{2.32}$$

$$= \left\{1 - \exp\left[-2(r_{\mathrm{hole}}/w_{\mathrm{z}})^2\right]\right\} \frac{1}{1+R_{\mathrm{e}}}, \tag{2.33}$$

where w_{z} denotes beam size at the end mirror expressed as

$$w_{\mathrm{z}} = \sqrt{\frac{\lambda}{\pi} R \sqrt{\frac{d}{R-d}}}. \tag{2.34}$$

Table 2.3 summarizes examples of measured shape ratios at the same position as the end mirror in the Fabry-Pérot cavity; therefore, $R_{\mathrm{beam}} \sim R_{\mathrm{cavity}}$ is expected. All R_{beam}s look consistent with each other, and also in good agreement with R_{cavity}.

frequency	R_{cavity}	R_{beam}
201.83	6.10×10^{-4}	$6.91^{+0.03}_{-0.35} \times 10^{-4}$
202.64	6.12×10^{-4}	$6.16^{+0.08}_{-0.39} \times 10^{-4}$
203.51	6.15×10^{-4}	$6.05^{+0.06}_{-0.35} \times 10^{-4}$
204.55	6.18×10^{-4}	$6.49^{+0.02}_{-0.28} \times 10^{-4}$
205.31	6.21×10^{-4}	$6.29^{+0.13}_{-0.44} \times 10^{-4}$

Table 2.3: Example of the measured shape correction for some frequencies. Measurements were performed at the end mirror position in the Fabry-Pérot cavity.

Simultaneous measurement of V_{tr} and P_{in}

The gyrotron is in pulse operation (duty ratio 30% and a repetition rate 5 Hz). For simultaneous measurement, output power should be divided into two optical paths. A beam splitter like one used to sample P_{in} and P_{re} (See Fig. 2.19) is useless because its frequency dependence is unknown. A chopper was developed to synchronously divide gyrotron pulse into two as shown in Fig. 2.22. At one phase, the Gaussian beam hits a Teflon box to be absorbed by water, and raises water temperature (ΔT). At the other phase, the Gaussian beam hits the end mirror to be detected by a pyroelectric detector (V_{tr}). No power leak was observed at the chopper. An effective duty ratio is 15% and a repetition rate is 2.5 Hz. The pulse width is still 60 ms so that response time effects of pyroelectric detector are the same as the original case.

Reflection at the Teflon box is 5% (measured and assigned as a systematic uncertainty) and others are all dumped inside the box filled with 46 ml water. A

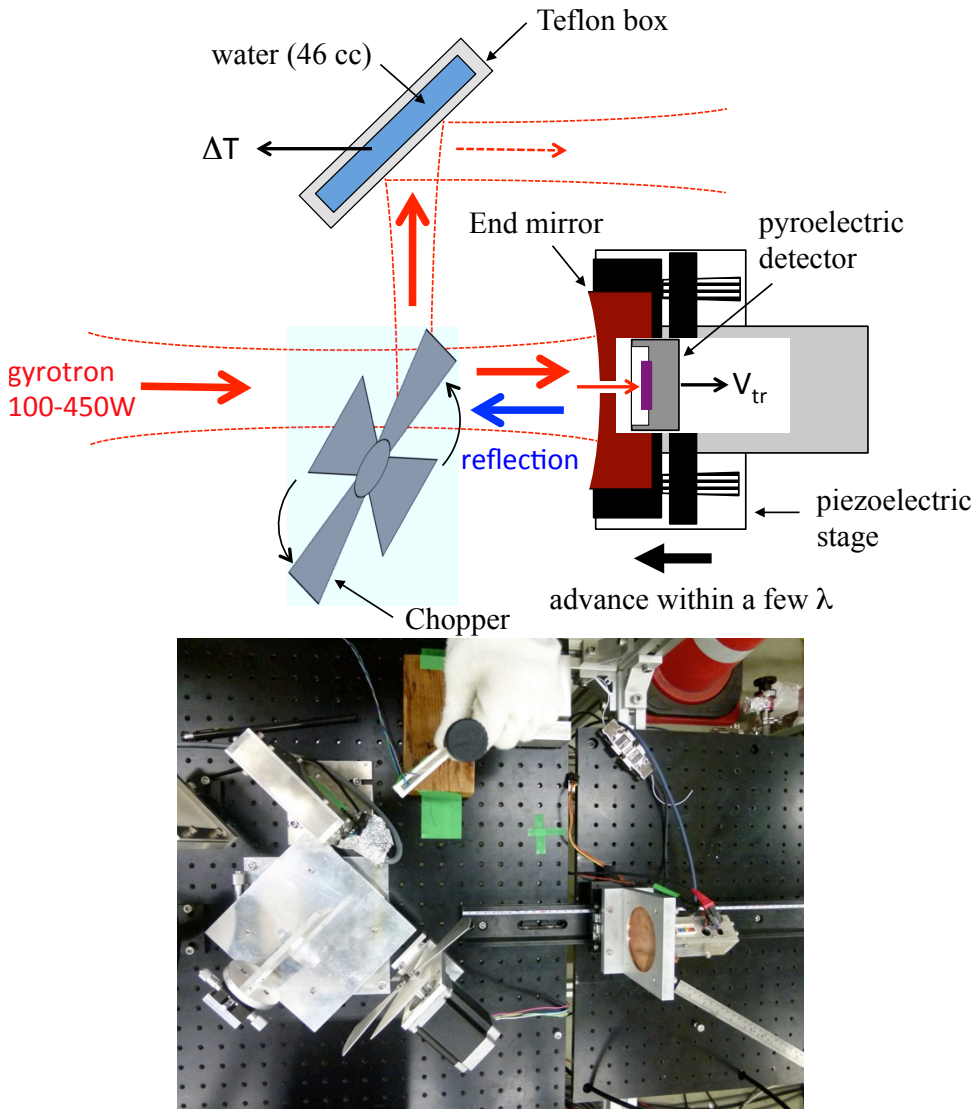

Figure 2.22: Schematic view and photograph of simultaneous measurement of V_{tr} and P_{in} (top view).

temperature increase of water, carefully stirred with a stick, was measured with a resistance thermometer Pt100 during the experiment (60 sec). The left figure in Fig. 2.23 shows a typical result of the temperature increase of water. The data were fitted by a function including thermal diffusion of water, which is expressed as

$$f(t < t_0) = T_0 \tag{2.35}$$

$$f(t > t_0) = T_0 + (T_{\rm inf} - T_0)\left[1 - e^{-\alpha(t-t_0)}\right], \tag{2.36}$$

where t_0 is a start time, T_0 is initial temperature, $T_{\rm inf}$ is asymptotic temperature after long time, and α is a constant determining velocity of thermal diffusion. Input power is expressed as

$$P_{\rm in} = \frac{(T_{\rm inf} - T_0) \times \alpha \times 4.2 \times 46}{0.95 \times {\rm duty}/2}, \tag{2.37}$$

where 0.95 means the transmittance of the Teflon box, and duty ratio is divided by 2 corresponding to chopping. In case of Fig. 2.23, $P_{\rm in} = 280$ W.

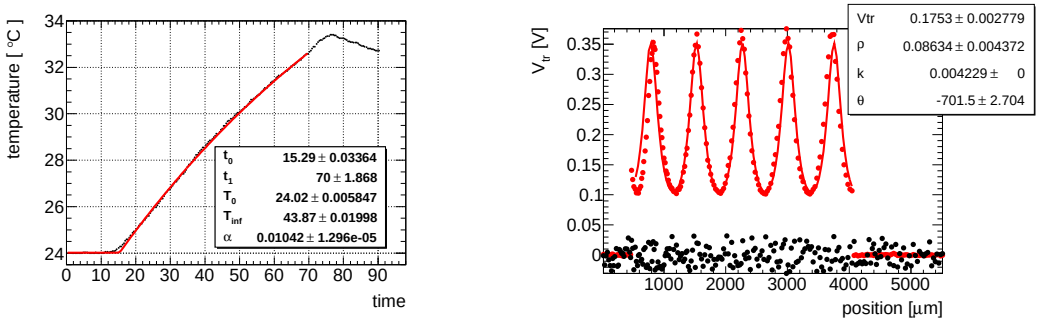

Figure 2.23: Data fitting for the power calibration. (left) Measurement of $P_{\rm in}$ with the temperature increase of water. Black points are measured data, and a red line is the best fit. (right) Measurement of $V_{\rm tr}$ by moving the piezoelectric stage near the mesh mirror position. Black points are data when the chopper is closed, and red points are measured data. A red line is the best fit.

Systematic uncertainty of this measurement was estimated as follows:

- Reflectivity of the Teflon box is 5%/95%.
- Accuracy of the amount of water is 2 ml/46 ml.
- Accuracy of time measurement is 2 s/60 s.
- Accuracy of temperature measurement is 0.2 °C/10 °C.

They are combined with square sum.

Transmitted power $V_{\rm tr}$ was measured at the different phase of the chopper. The reflected beam at the end mirror is again reflected at the RF cavity in the gyrotron or the output window to make up a standing-wave. The piezoelectric stage advanced within a few wavelength to measure the standing-wave. The standing-wave formula Eq. (2.12) was used here to fit $V_{\rm tr}$ and re-written as

$$f(x) = \frac{V_{\rm tr}}{[1-\sqrt{\rho}]^2 + 4\sqrt{\rho}\sin^2[k(x-\theta)]}, \tag{2.38}$$

where ρ is round-trip reflectance, and k is wave number and fixed. The right figure of Fig. 2.23 shows the result of this fitting.

Correction of the reflection effect

There is one problem due to reflection at the end mirror other than the standing-wave production. The reflected beam from the end mirror reduces oscillation efficiency only in measuring $V_{\rm tr}$. One assumes no-reflection in gyrotron oscillation described in Sec. 2.2.1. Reflected radiation changes boundary conditions (See Eq. (A.7) for detail), and disturbs the electric field in the RF cavity. This phenomenon is affected by both electron-beam alignment and reflection conditions, and the same phenomenon is reported in a MW-class gyrotron [49].

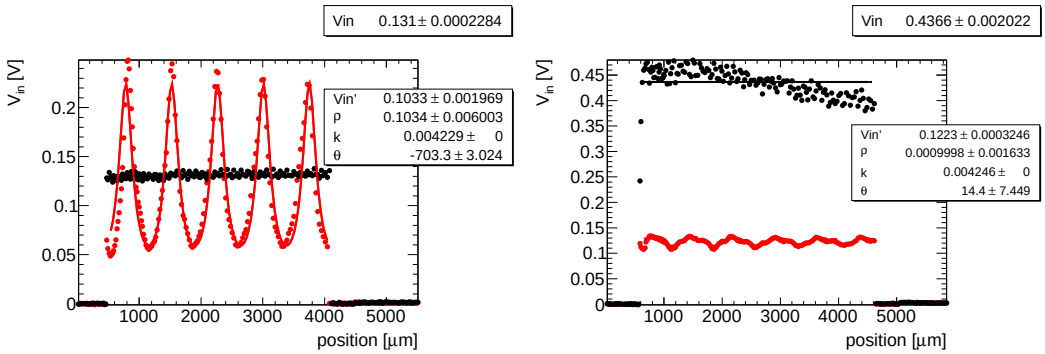

Figure 2.24: Data fitting for the reflection correction. Black points are data in phase of $P_{\rm in}$ measurement (no reflection), and red points are data in that of $V_{\rm tr}$ measurement. Solid lines are the best fits for each data. The end point mirror moves a few wavelength near the mesh mirror position of the Fabry-Pérot cavity. (left) Small correction case. (right) Large correction case.

This effect was corrected by sampling incident power ($V_{\rm in}$) with the beam splitter shown in Fig. 2.19 before the chopper. Although splitting efficiency itself is unknown, one can use it to give $V_{\rm tr}$ a relative correction at the same frequency. $V_{\rm in}$ at $V_{\rm tr}$ measurement (defined as $V'_{\rm in}$) was fitted by Eq. (2.38), while $V_{\rm in}$ at the water measurement phase was fitted by a constant. $P_{\rm in}$ value was corrected with

$V'_{\rm in}/V_{\rm in}$ to simulate the real value $P'_{\rm in}$ in measuring $V_{\rm tr}$ with reflection. Figures 2.24 show two typical results of $V_{\rm in}$ measurement at different conditions. Systematic uncertainties were propagated from fitting errors of $V_{\rm tr}$, $V'_{\rm in}$ and $V_{\rm in}$.

Result of the measurement for calibration constant C

Summarizing above discussion, the calibration constant C is expressed as

$$C = \frac{P_{\rm acc}}{V_{\rm tr}} = \frac{R_{\rm beam}}{R_{\rm cavity}} \frac{P'_{\rm in}}{V_{\rm tr}} = \frac{R_{\rm beam}}{R_{\rm cavity}} \frac{V'_{\rm in}}{V_{\rm in}} \frac{P_{\rm in}}{V_{\rm tr}}. \tag{2.39}$$

We measured calibration constant C at three different distances (600 mm, 750 mm, 900 mm from the toroidal mirror M2) to check the reflection correction with $V_{\rm in}$. Examples of C measurements are listed in Table 2.4. In case of 201.83 GHz, reflection correction $V'_{\rm in}/V_{\rm in}$ is almost independent of the distance, and C is within one standard deviation. Reflection corrections of 202.64 GHz differ by factor of five for independent four measurements; however, C is still within two standard deviations. It means the reflection correction is necessary to obtain proper C values, and works well in all cases.

frequency	distance	$\frac{R_{\rm beam}}{R_{\rm cavity}}$	$P_{\rm in}$ [W]	$\frac{V'_{\rm in}}{V_{\rm in}}$	$V_{\rm tr}$ [mV]	C [kW/V]
201.83 GHz	600 mm	$1.880^{+0.195}_{-0.367}$	280(22)	0.793	17.53(28)	$23.7\ ^{+3.1}_{-5.0}$
201.83 GHz	900 mm	$0.516^{+0.002}_{-0.015}$	239(19)	0.864	5.41(09)	$19.7\ ^{+1.6}_{-1.7}$
202.64 GHz	600 mm	$1.842^{+0.077}_{-0.242}$	271(21)	0.634	18.04(15)	$17.5\ ^{+1.6}_{-2.7}$
202.64 GHz	600 mm	$1.638^{+0.007}_{-0.196}$	582(46)	0.280	10.92(07)	$24.4\ ^{+2.7}_{-3.7}$
202.64 GHz	900 mm	$0.505^{+0.002}_{-0.015}$	240(18)	1.010	5.42(05)	$22.5\ ^{+1.8}_{-1.8}$
202.64 GHz	900 mm	$0.583^{+0.002}_{-0.039}$	484(38)	0.388	4.17(03)	$26.3\ ^{+2.1}_{-2.7}$

Table 2.4: Example of C measurement and $V_{\rm in}$ correction.

The results are all averaged for all frequencies and distances, and summarized in Table 2.5 and Fig. 2.25. C becomes roughly increasing in decreasing frequency because transmittance of an evanescent mode is reduced (cutoff frequency is about 290 GHz). A discrete structure near 203 GHz may be due to interference behind the end mirror, and is expected to give a proper result if one fixes the mirror structure. The value of C is tested with an independent method in Sec. 4.1, and obtained consistent results.

A systematic error was given by square root of the sum of squares of $R_{\rm beam}$, $P_{\rm in}$, $V_{\rm tr}$, $V_{\rm in}$, and $V'_{\rm in}$. In addition, standard deviation of each C value for different conditions was combined in a similar way to introduce remaining fluctuations in each measurement. A systematic error in C measurement directly affects the Ps-HFS value. The purpose of this experiment, the first direct measurement, can be achieved with this uncertainty. In the future, one should improve the precision by

100 times to address the observed discrepancy of Ps-HFS. A possible improvement is discussed in Sec. 4.3.

frequency	C [kW/V]	relative accuracy
180.56	$32.4^{+7.8}_{-9.4}$	27%
201.83	$23.2^{+3.4}_{-4.0}$	16%
202.64	$23.4^{+4.5}_{-4.9}$	20%
203.00	$14.6^{+2.2}_{-2.3}$	15%
203.25	$13.0^{+1.5}_{-1.7}$	12%
203.51	$10.2^{+1.3}_{-1.5}$	14%
204.56	$11.3^{+2.3}_{-2.5}$	21%
205.31	$11.4^{+1.4}_{-1.6}$	14%

Table 2.5: Measured absolute calibration constant C.

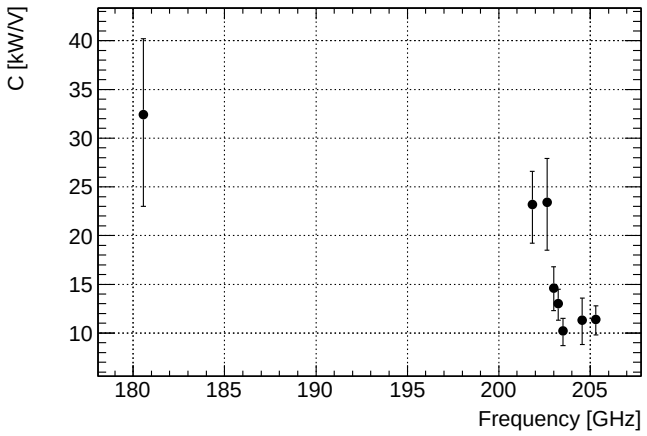

Figure 2.25: Result of C measurement.

2.2.4 Power Stabilization

Accumulated power in the Fabry-Pérot resonant cavity should be stabilized to properly determine the cross-section of the Ps-HFS transition. Resonant power is a result of output power of the gyrotron, stability of output frequency, and length of the Fabry-Pérot cavity. The former two are automatically determined by non-linear plasma-wave interaction in the gyrotron. Controllable parameters

are magnetic field strength, electron-beam current, electron-beam trajectories, and length of the Fabry-Pérot cavity.

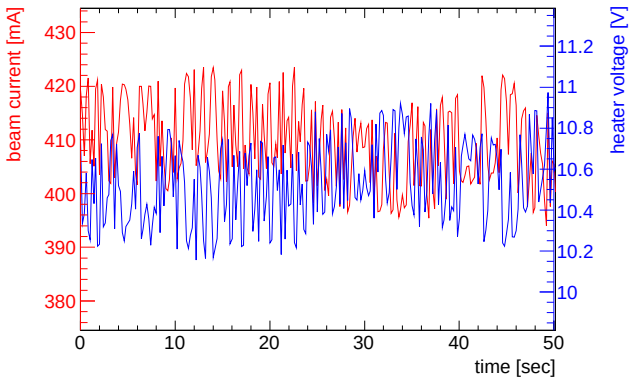

Figure 2.26: Electron beam current stabilized by heater-voltage feedback.

Stabilization of electron beam current

Electron beam current I_b in the gyrotron is controlled with heater temperature at the beam-emitter ring (thermionic electron emission). Heater temperature is around 1000°C if one imposes voltage $V_\mathrm{H} \sim 10\,\mathrm{V}$ to the heater. I_b was stabilized with Proportional Integral (PI) control method. The voltage of the heater was controlled with its AC high-power supply (MATSUSADA SRJ500) which can communicate with the PC via RS232C. The output voltage of the power supply V_AC was determined by the following equation.

$$V_\mathrm{AC}(n) = V_\mathrm{AC}(n-1) + K_\mathrm{P}(I_\mathrm{b}(n-1) - I_\mathrm{b}(n)) + K_\mathrm{I}(I_\mathrm{b}^\mathrm{target} - I_\mathrm{b}(n)), \qquad (2.40)$$

where $V_\mathrm{AC}(n)$ is the supply voltage set at the n-th operation, $I_\mathrm{b}(n)$ is the beam current at the n-th measurement, K_P is a proportional gain, K_I is an integral gain, and $I_\mathrm{b}^\mathrm{target}$ is a target voltage. K_P is set to 40 and K_I is set to 0.08 (Typical voltage is $V_\mathrm{AC} \sim 135$ V corresponding to $V_\mathrm{H} \sim 10$ V, $I_\mathrm{b} \sim 400$ mA). Figure 2.26 is a monitor plot of I_b and V_H with this stabilization system. It was achieved that the gyrotron beam current was stable within ±10 % for both a short time (1 minute) and a long time (one day). Gyrotron oscillation gradually becomes stable and outputs steady power by constant beam current. Note that output power itself is not a proper parameter to be stabilized because of strong non-linearity in the high-power gyrotron operation. As is mentioned in Sec. 2.2.1, output power can be a multivalued function of I_b in case of nearly hard excitation [46].

Stabilization of resonance of the Fabry-Pérot resonant cavity

Cavity length is varied without moving the piezoelectric X-stage due to the fluctuation of the temperature of the gas chamber and long-term frequency drift of gyrotron. Cavity length should be controlled to accomplish on-resonance for long time. Accumulated power integrated with one pulse (60 ms) was stabilized as follows. Two thresholds $V_{\rm high}$ and $V_{\rm low}$ were defined, and cavity length was controlled so that $V_{\rm tr}$ was between $V_{\rm high}$ and $V_{\rm low}$. Cavity length was rescanned to search the resonant position only when the $V_{\rm tr}$ falled below $V_{\rm low}/2$. Figure 2.27 is a monitor plot of $V_{\rm tr}$ and the mirror position.

Even if cavity length is well controlled, accumulated power in one pulse is not necessarily stabilized because line-width (a few MHz) and frequency drift (about 20 MHz) are broader than bandwidth of the Fabry-Pérot cavity. Control of cavity length cannot catch up with such a fast fluctuation. This resulted in power fluctuation in pulses depending on condition of gyrotron operation. This effect was inevitable with the current gyrotron, and was corrected in data analysis described in Sec. 3.4.

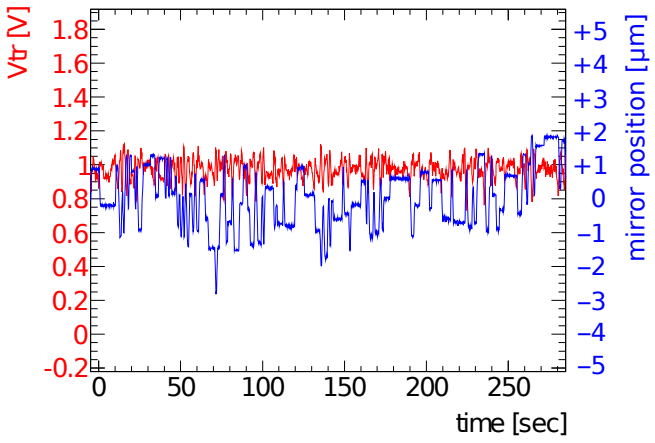

Figure 2.27: Accumulated power stabilized by control of the mirror position.

2.3 Positronium Assembly and γ-ray Detectors

Photographs of a Ps assembly and γ-ray detectors are shown in Fig. 2.28. Figure 2.29 and 2.30 show top and side view of a schematic picture of a gas chamber, respectively. Ps is formed by a positron from a ^{22}Na source and an electron in a gas molecule. If it is formed in a beam region of the Fabry-Pérot cavity, the transition from o-Ps to p-Ps occurs. γ rays from Ps decays are detected by γ-ray detectors.

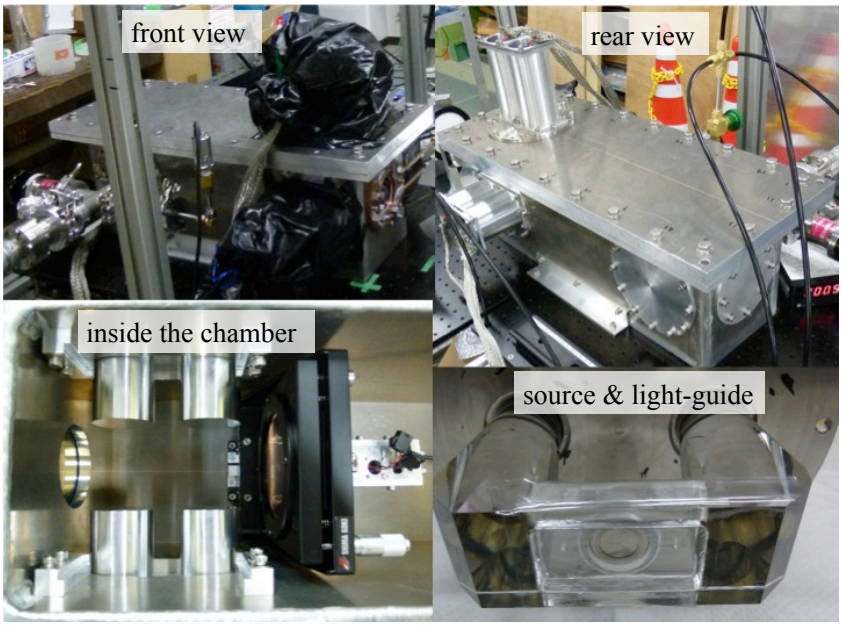

Figure 2.28: Photograph of the chamber.

2.3.1 Positronium Formation Assembly

A ^{22}Na positron source is mounted on a UV-transparent acrylic light-guide shown in Fig. 2.28. The source emits a positron (end point energy is 546 keV, probability is 90%), then consecutively emits one 1275 keV γ ray. A thin plastic scintillator (NE102, thickness = 0.1 mm) is placed next to the source to tag emission time of a positron. Optical photons go through the light-guide which is divided into right and left to reach two photo-multipliers (PMT) shown in Fig. 2.30 as Pla-0 and Pla-1. Coincidence of two PMTs reduces accidental events from dark current or electric noise. A fine-mesh type PMT (HAMAMATSU R5924-70, 2 inch) is used to reduce effects of a remaining magnetic field (1 mT) of the superconducting magnet in the gyrotron. A lead plate (thickness = 20 mm) shields 1275 keV γ rays and 511 keV ones from positrons annihilating near the source.

The gas chamber is filled with 1 atm gas. The gold mesh mirror on a silicon substrate is used as a window of the gas chamber. The silicon substrate is not

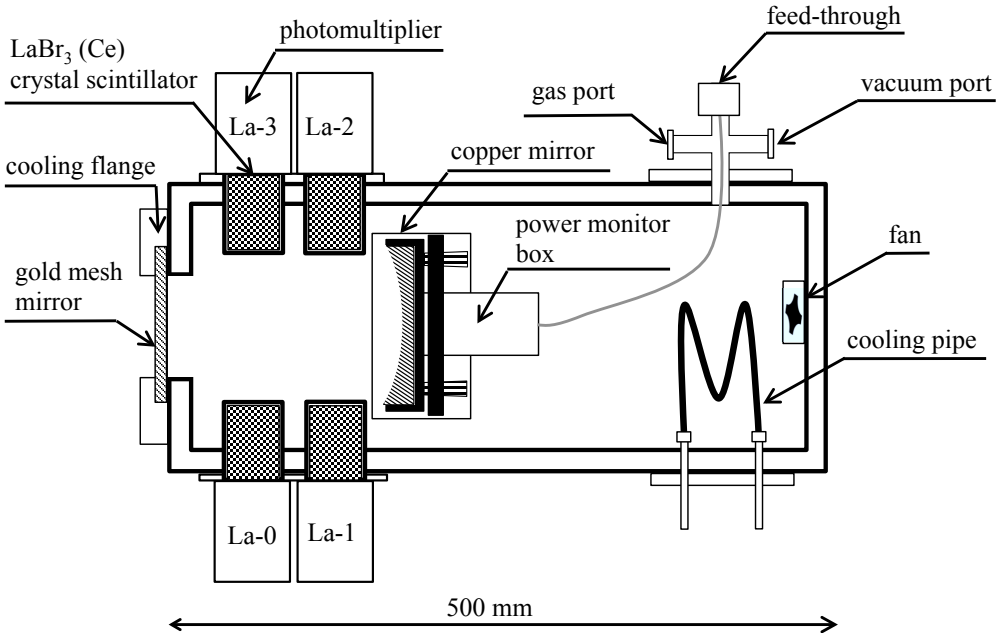

Figure 2.29: Schematic picture of a gas chamber (top view).

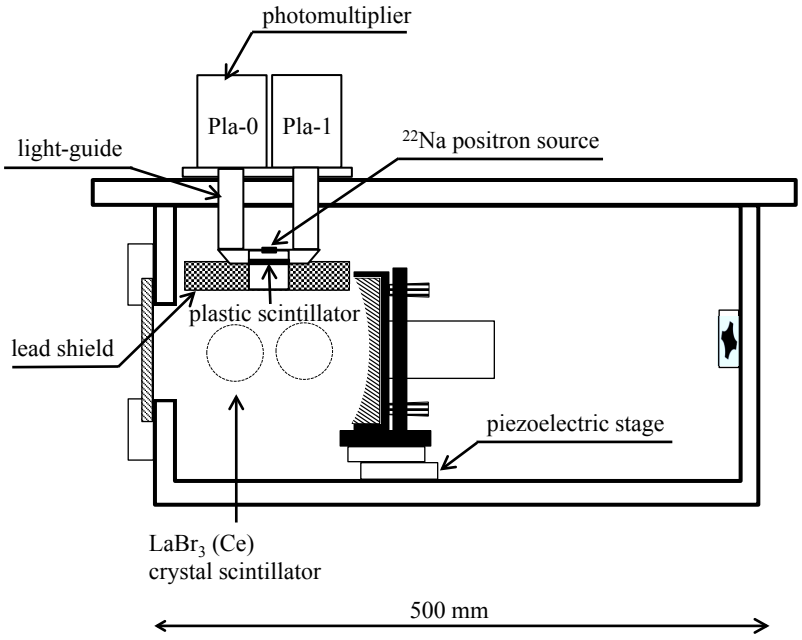

Figure 2.30: Schematic picture of a gas chamber (side view).

transparent to optical photons so that it plays a role of a light shielding for the plastic scintillator and the light-guide. Gas temperature is cooled with a cooling pipe (20°C water flow) and a fan in the chamber as shown in Fig. 2.29. A positron decelerates as ionizing gas molecules and finally stops in the chamber. The number of stopping positrons at the beam region is about 2% of all emitted positrons and 7% of positrons tagged by the plastic scintillator. About half of the stopping positrons becomes Ps. 25% of the formed Ps is p-Ps and immediately (lifetime = 125 ps) decays into two γ rays (511 keV). 75% of them is o-Ps and is alive long time. Since 7.9% of o-Ps annihilates in colliding with an electron in a gas molecule (pick-off annihilation), lifetime of o-Ps is reduces from 142 ns to 131 ns. Neopentane gas was selected to eliminate backgrounds, and is discussed in more detail in the next section.

2.3.2 Selection of Gas

Gas selection was one of the most important points in this experiment. Mixed gas of nitrogen and isobutane was used in previous measurements [54]. It appeared that a non-negligible systematic error remains in this gas. We consider gas effects divided into following three steps:

- Reduction of slow positron
- Power absorption by gas
- Positron acceleration by millimeter waves and collision with gas molecules

These are described in the following sections.

Slow positron annihilation

According to the Ps formation theory by Ore, a positron (ionization potential = 6.8 eV) can produce Ps if its kinetic energy E satisfies

$$I_{1\mathrm{st}} - 6.8\,\mathrm{eV} < E < E_{\mathrm{ex}}, \tag{2.41}$$

where $I_{1\mathrm{st}}$ and E_{ex} are the first ionization potential and excitation energy of the gas molecule, respectively. This condition is called *Ore gap*. If kinetic energy of a positron is too small, the positron cannot capture an electron to become a Ps atom. Less than half of positrons stopped in gas can make Ps. The others become *slow positron* and remain in gas. The annihilation rate of slow positron is expressed as

$$\Gamma_{\mathrm{slow}} = \pi r_0 c n Z_{\mathrm{eff}}, \tag{2.42}$$

where r_0 is the classical radius of electron, n is number of density of gas, and Z_{eff} is the effective electron number which contributes to the annihilation. Z_{eff} depends on gas molecules listed in Table 2.6 [55][56].

Figure 2.31 shows time spectra of slow positron and o-Ps in 1 atm nitrogen separated with energy information. When a part of o-Ps transits into p-Ps, its decay looks the same as slow positron (back-to-back 2γ rays of 511 keV). Signal to noise ratio (S/N) is too low to observe this transition in case of pure nitrogen. Lifetime of slow positron should be smaller than that of o-Ps.

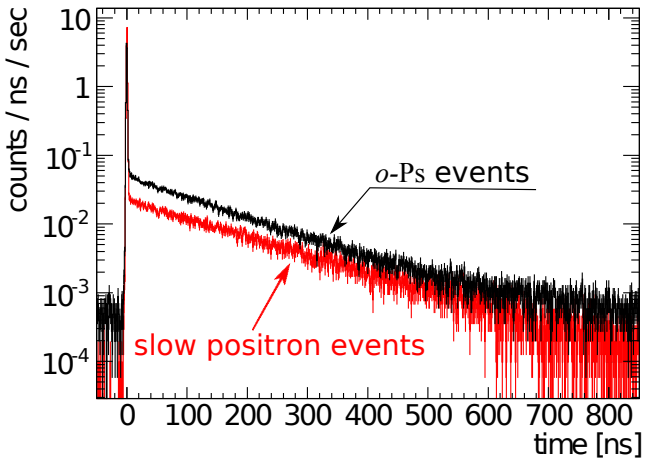

Figure 2.31: Time spectra of slow positron and o-Ps in 1 atm nitrogen. The red line shows slow positron (lifetime = 167 ns) by selecting back-to-back 511 keV γ ray. The black line shows o-Ps (lifetime = 133 ns in nitrogen) by selecting Compton-free (from 360 keV to 450 keV) γ ray.

According to Table 2.6, alkane molecules are favored because of its short lifetime of slow positron. Isobutane gas was used as a quencher of slow positron in some experiments [38][54]. However, it is not proper to use pure isobutane in our experiment because of power absorption described in the next section.

Absorption of 203 GHz radiation

Polyatomic gases have rotational levels and vibrational levels as an internal degree of freedom. If a molecule also has an electric dipole moment d, it absorbs electromagnetic radiation via transitions between these levels. In case of 203 GHz (wavelength = 1.47 mm) radiation, the rotational transitions should be considered. The vibrational transitions are higher than 1 THz and can be ignored.

Energy difference ΔE between rotational levels is expressed as [57]

$$\Delta E = 2 \cdot \frac{\hbar^2}{2I}(J+1) = 2B(J+1), \tag{2.43}$$

gas	Z_{eff}	lifetime [ns]	B [GHz]	d [Debye]
Ar	33.8	147.9	no	0.00
N_2	30.5	163.9	59.91	0.00
CO_2	54.7	91.4	11.70	0.00
methane	142	35.2	157.13	0.00
isobutane	14,400	0.35	7.789	0.132
neopentane	21,400	0.23	4.4 (calc.)	0.00

Table 2.6: Property of gas (1 atm).

where I is a moment of inertia around one axis, and $J = 1, 2, 3, ...$ is a rotational quantum number. $B = \hbar^2/2I$ is called rotational constant, and measured or calculated for many molecules. B and d for some gas molecules often used in Ps experiments are listed in Table 2.6 [58][59]. Isobutane has absorption lines near 203 GHz, which are at 186.9 GHz, 202.5 GHz and 218.1 GHz.

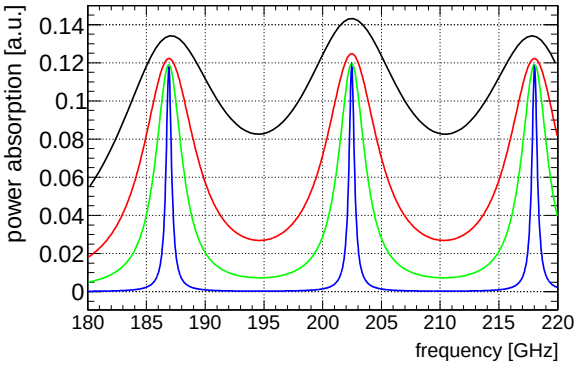

Figure 2.32: Calculated frequency dependence of power absorption by isobutane. Black line is 2 atm, red is 1 atm, green is 0.5 atm and blue is 0.1 atm.

If the absorption line is sharp enough, gyrotron frequency can be tuned to keep away from the absorption peaks. Line-width Δf of the power absorption is broadened by collisions of gas molecules, and is expressed as [57]

$$\Delta f = 2 \times \frac{1}{2\pi\tau} \tag{2.44}$$

$$\tau = \frac{1}{\sigma v_{\text{rel}} n} \tag{2.45}$$

where τ is lifetime of one rotational level determined by the collision, σ is a cross-section of the collision, v_{rel} is relative velocity between the gas molecules, n is

number of density of the gas molecule. If we assume elastic scattering and approximate isobutane radius as 3.5Å, σ is $\sim 1.5 \times 10^{-18}\,\mathrm{m}^2$. In case of 1 atm and 300 K, $v_{\mathrm{rel}} = 465$ m/s and $n = 2.45 \times 10^{25}$ m^{-3}. Estimated Δf is about 5.4 GHz, which covers from 197 to 209 GHz as shown in Fig. 2.32. It is fatal that power absorption by pure isobutane causes depression of finesse of the Fabry-Pérot cavity. Although pure isobutane was studied in detail in other experiments [38], it is improper to be used in this experiment.

Positron acceleration by millimeter waves

So far we rejected to use pure nitrogen and pure isobutane because of slow positron and power absorption, respectively. However, mixed gas of nitrogen and isobutane seems to work well. Slow positron lifetime is 3.4 ns (1.9 atm nitrogen and 0.1 atm isobutane), and power absorption is strongly suppressed by pressure broadening by mixed nitrogen. This mixed gas was previously used in the first observation of the Ps-HFS transition at 202.9 GHz [54]. A new systematic problem becomes apparent when we measure the Ps-HFS resonance curve. The high-power millimeter-wave field ($E \sim 200$ kV/m at 20 kW accumulation) used increases the amount of Ps formed.

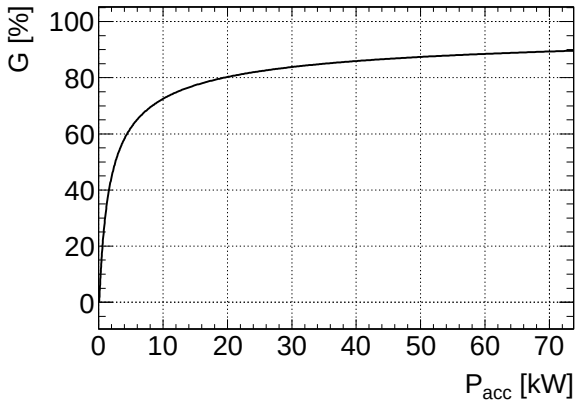

Figure 2.33: Increase of positronium formation with random walk model of positron acceleration with millimeter-wave radiation.

It was reported in the first indirect measurement of Ps-HFS that Ps formation probability in nitrogen gas increases under high-power microwaves [24]. It was interpreted that slow positrons are accelerated to the energy over the lower edge of Ore gap defined by Eq. (2.41). This effect was studied in detail using a static electric field [60][61], but not done for high frequency fields so far. The same phenomenon by a millimeter wave was firstly observed in this experiment. A positron is accelerated

or decelerated by a millimeter wave due to the Lorentz force. Since frequency of this interaction is about 200 GHz, mean energy gain of positron in *vacuum* is very small (about 1 meV). However, in about 1 atm gas, the energy gain can exceed the Ore gap due to collisions (a few ps cycle) between a positron and gas molecules. These collisions randomize the phase of a positron in acceleration and a part of positrons statistically obtains kinetic energy of a few eV within several ns. A simple theory with a random-walk model is derived in Appendix B. Figure 2.33 shows simulated positronium formation probability G in case of 1 atm nitrogen gas. It is clearly seen that an increase of Ps formation probability can occur in high-power millimeter-wave radiation.

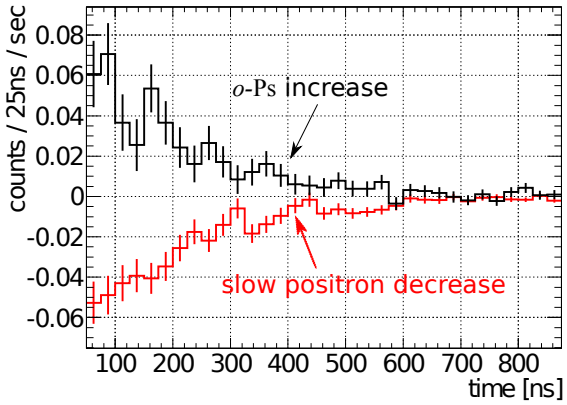

Figure 2.34: Time spectra of increase of positronium formation in 1 atm nitrogen gas by millimeter-wave radiation. Millimeter-wave radiation of equivalent power $P_{\mathrm{acc}} = 24\,\mathrm{kW}$ is confined in the Fabry-Pérot cavity.

The increase of Ps formation was observed as shown in Fig. 2.34, in which o-Ps events increase while slow positron ones decrease by high-power millimeter waves (24 kW). Slow positron events were selected by an energy cut 511 keV $^{+3\sigma}_{-2\sigma}$ whose energy is from 360 keV to 450 keV, and o-Ps events were selected by an energy cut from 360 keV to 450 keV (Compton free from the 511 keV signal). The Ps formation increase was probed by subtracting beam OFF events from ON ones (See Sec. 3.3.4). In case of simple gas like argon or nitrogen, the increase of Ps formation was observed. The same phenomenon occurred in mixed gas of nitrogen and isobutane. We cannot use gas containing nitrogen in this experiment. In contrast, Ps did not increase in *pure* alkane gas as suggested in [60][61]. An accelerated positron excites many internal modes (rotation and vibration) of complex gas molecules at inelastic scattering to drastically reduce energy gain. Since isobutane absorbs 203 GHz radiation, the only remaining possibility is pure neopentane.

2.3.3 γ-ray Detectors

Four $LaBr_3$ (5% Ce) crystal scintillators (Saint-Gobain Crystals, BriLanCe^{TM} 380) are placed around the beam region denoted as La-0, La-1, La-2, and La-3 (Fig. 2.29). Figure 2.35 shows a photograph of the scintillators. Size of $LaBr_3$(Ce) crystal are ϕ 1.5 inch $\times$ 2.0 inch. The crystals are covered with an aluminum housing (0.5 mm thick). They are connected to PMT (HAMAMATSU R5924-70). Assemblies of the crystals and PMTs are out of the gas chamber protected against contamination of neopentane.

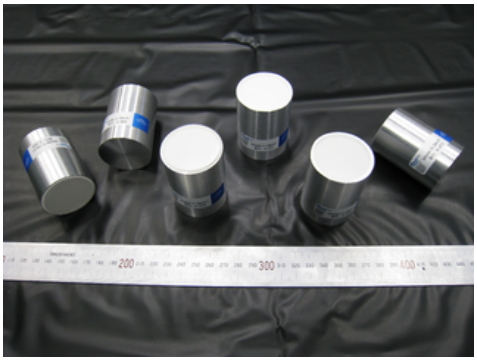

Figure 2.35: Photograph of $LaBr_3$(Ce) crystals

The annihilation γ-rays were detected using a coincidence pair of scintillators. Four back-to-back pairs are (La-0, La-2), (La-0, La-3), (La-1, La-2), and (La-1, La-3). The number of events of each pair is almost the same because Ps formation region in gas is wide (about 100 mm), and shape of 203 GHz beam accumulated in the Fabry-Pérot cavity is long (156 mm). The energy resolution is higher than other inorganic scintillators (about 4% in FWHM), and together with back-to-back coincidence, two 511 keV γ-ray annihilation events can be enhanced by tight energy selection. Its fast time response (τ = 16 ns) is also appropriate for experiments with high statistics compared with semiconductor detectors like a Germanium crystal. High Z of La gives higher stopping power than a NaI scintillator. The characteristics of the scintillator are summarized in Table 2.7.

Light yield [photons/keVγ]	63
Primary decay time [ns]	16
Density [g/cm^3]	5.08
Wavelength of emission max [nm]	380
Refractive index @ emission max	1.9
Thickness for 50 % attenuation (662 keV) [cm]	1.8

Table 2.7: Properties of $LaBr_3$(Ce) scintillator

2.4 Electronics and Data Acquisition

2.4.1 Overview

A data acquisition (DAQ) and control system consist of two parts, a detector part and an optics part. The detector part is comprised of the NIM standard modules and the CAMAC system to acquire electric signals from PMTs of the plastic scintillator and the $LaBr_3$(Ce) detectors. The optics part controls the optical system and monitors experimental conditions (power, temperature, pressure, gyrotron parameters, a position of the piezoelectric stage, etc.). It consists of a data logger (HIOKI 8420-50), a piezoelectric X-stage (NANO CONTROL TS102-G), pyroelectric detectors, an ADC (National Instruments NI PCI-6225, 16 bits, 250 kHz), and an interlock (OMRON PLC Cj1). All data are sent to a Linux computer (PC) and stored in a hard disk drive. Figure 2.36 is a schematic view of the whole DAQ system.

The resonant peak of the Fabry-Pérot cavity is searched by moving the piezoelectric stage, whose driver is connected to the PC via RS232C. Cavity length is controlled so that the cavity can stay on resonance. Once the cavity stays on resonance, then the electron-beam current I_b is stabilized by controlling the heater voltage of the MIG (Sec. 2.2.4). The AC voltage of the heater is supplied by Matsusada Precision SRJ500 and its output voltage is remote-controlled from the PC via RS232C. Accumulated power in the cavity gradually becomes stable as steady gyrotron oscillation achieved with the constant beam current.

After the stabilization, the PC sends a start command to the CAMAC controller (Toyo Corp. CC/NET), and the detector part begins to acquire data. All the CAMAC modules are cleared and the latch is released by the reset signal from the output register. This makes all the systems active and the controller waits the interrupt signal, so-called LAM (Look-At-Me) signal from a charge-sensitive ADC (CAEN C1205). The interrupt signal comes only when the trigger condition is satisfied. The data acquisition is triggered when back-to-back γ-ray signals from the $LaBr_3$(Ce) scintillators are coincident within 40 ns and then when this coincidence is within -100 ns to 1100 ns of the timing of the plastic scintillators. The charge-sensitive ADC (CAEN C1205) measures energy information of the $LaBr_3$(Ce) detector. Two charge-sensitive ADCs (PHILLIPS 7167 and REPIC RPC-022) are used to measure energy information of the plastic scintillator with different gate length. Time information of the plastic and $LaBr_3$(Ce) scintillators is recorded using a direct clock (2 GHz) count type TDC (KEK GNC-060). After the reading procedures, the controller saves the data through NFS and starts the next event cycle.

Environmental conditions (temperature, pressure) are recorded with the data logger (HIOKI 8420-50). The incident (Vin), reflected (Vre) and transmitted (Vtr) power are monitored with the pyroelectric detectors as shown in Fig. 2.19. Signal waveforms of the pyroelectric detectors (duty ratio 30%, a repetition rate 5 Hz, pulse width 60 ms) are read with the ADC (NI PCI-6225) whose sampling

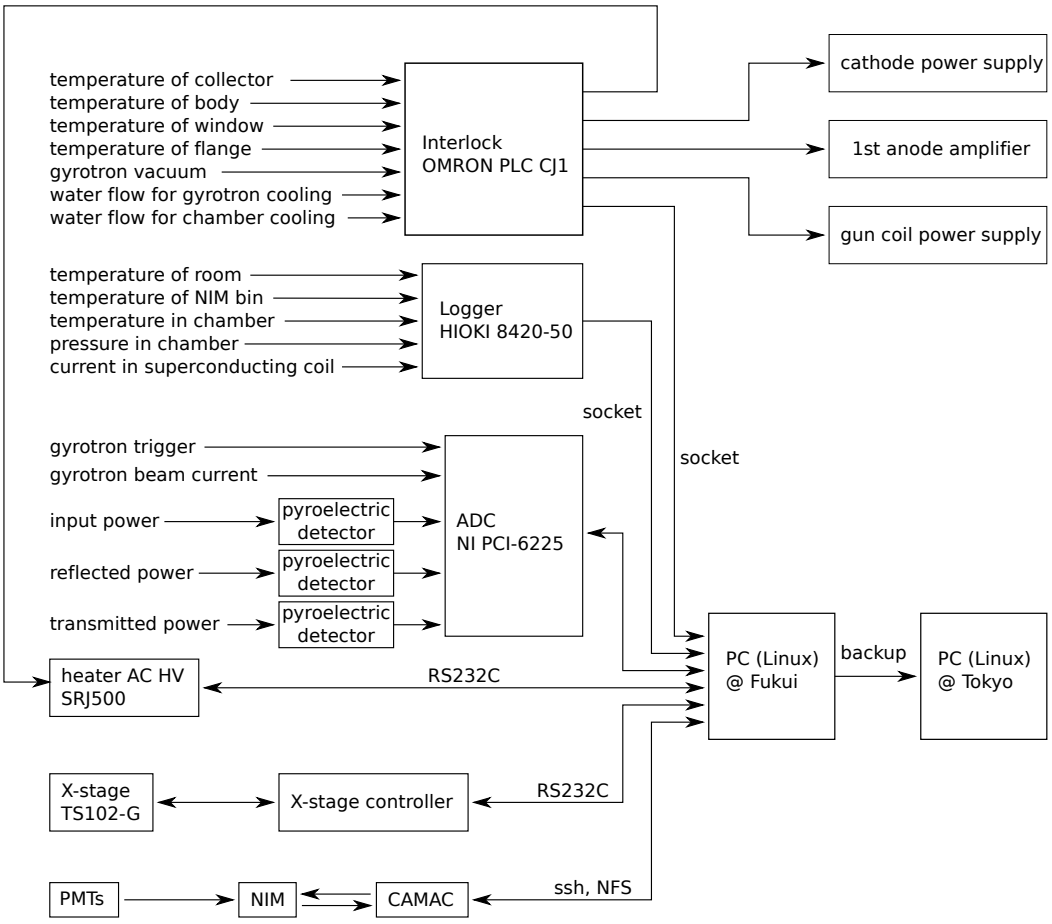

Figure 2.36: The schematic view of the whole DAQ system.

rate is set to 0.5 Hz. The trigger pulse for the gyrotron output and the level of the electron-beam current (I_b) are also recorded with the same ADC. These data per gyrotron trigger are recorded to the PC every 100 cycles.

Some parameters important for safety operations are recorded with an Interlock (OMRON PLC Cj1). The interlock shuts down a cathode power supply, a voltage amplifier of 1^{st} anode, a gun-coil power supply, and a heater power supply in case of a bad operation or a sudden blackout. Temperatures of different parts of the gyrotron are monitored to check abnormal electron-beam trajectories and prevent components from thermal destruction. Gyrotron vacuum is monitored not to expose the emitter surface of the MIG to accidental out-gassing. Water-cooling flow and temperature are also checked. These data per five seconds are sent to the PC independently of the other DAQ systems.

Details of the detector part are described in the following sections.

2.4.2 Electronics for the Plastic Scintillator

A circuit diagram for the plastic scintillator is shown in Fig. 2.37. Two PMTs for the plastic scintillator are operated at +2215 V (Pla-0) and +2250 V (Pla-1). High voltage are supplied by a positive high voltage module (iseg NHQ204M). Their gains are 3.4×10^7 (Pla-0) and 3.8×10^7 (Pla-1).

Output of the PMT is divided into three lines by a linear fan-out module (RIS-0255). One of the divided signals is fed into a discriminator (KN246). The threshold value of the discriminator is set to 25 mV, which corresponds about 1 photoelectron. The others are used to measure the signal amplitude with a charge-sensitive ADC (PHILLIPS 7167) of short gate (60 ns) and a charge-sensitive ADC (REPIC RPC-022) of long gate (1000 ns). All analog transmission lines are covered with electric shield, and are prepared as short as possible to reduce electric noise from gyrotron's pulse operation.

One of the outputs of the discriminator is delayed by 200 ns and then provides a stop signal for the TDC (KEK GNC-060). The other output is used to make a coincidence signal of the two PMTs (Pla-and). Dark current and another accidental noises are suppressed by requiring the coincidence. The coincidence signal is used to make a common start signal of the TDC (KEK GNC-060), a short gate signal of the charge-sensitive ADC (PHILLIPS 7167), a long gate signal of the charge-sensitive ADC (REPIC RPC-022), a fast clear, and a main trigger. These are described in a trigger section.

2.4.3 Electronics for the γ-ray Detectors

A circuit diagram for the γ-ray detectors is shown in Fig. 2.38. High voltages of the four PMTs (HAMAMATSU R5924-70) are supplied by a positive high-voltage module (MATSUSADA HEER-3R10) and distributed by a voltage divider (technoland 201A-SHV). The high-voltage values are +1450 V for La-0, +1330 V for La-1, +1230 V for La-2, and +1290 V for La-3.

Output of the PMT is divided into two lines by a linear fan-out module (RIS-255). One of the divided signals is fed into a discriminator (KN246). The threshold value is set to 90 mV corresponding to about 50 keV. The other signal is used to measure the signal amplitude with a charge-sensitive ADC (CAEN C1250)of 150 ns gate width.

One of the outputs of the discriminator is delayed by 200 ns and then provides a stop signal for the TDC (KEK GNC-060). The other output is fed by a logic fan-in/fan-out module, and then sent to a coincidence logic unit. The output of the logic unit becomes the back-to-back coincidence signal of the four γ-ray detectors (La-b2b). The La-b2b signal is used to make a gate signal of the charge-sensitive ADC (CAEN C1205) and the main trigger.

2.4.4 Electronics for the Trigger System

A circuit diagram for the trigger system is shown in Fig. 2.39. The coincidence signal from the two PMTs for the plastic scintillator (Pla-and) is widened to 1200 ns (Pla-gate). The La-b2b signal is delayed by 100 ns, and as coincidence with Pla-gate, it triggers data acquisition (main trigger). The main trigger is also a gate signal of the charge-sensitive ADC (CAEN C1205) to record energy information of the $LaBr_3$(Ce) detectors. The trigger signal provides a latch start at the same time. The latch signal vetos the subsequent gate signals and fast clear signals. After all the data are read and saved, the latch reset signals are produced by an output register of CAMAC.

The short and long gate signals for the ADCs for the plastic scintillator are produced by Pla-gate independently of the main trigger. The data are cleared by the clear signal (fast clear) unless the main trigger signal is produced. The Pla-gate also produces the common start signal for the TDC. The TDC data is cleared by the fast clear in the same way.

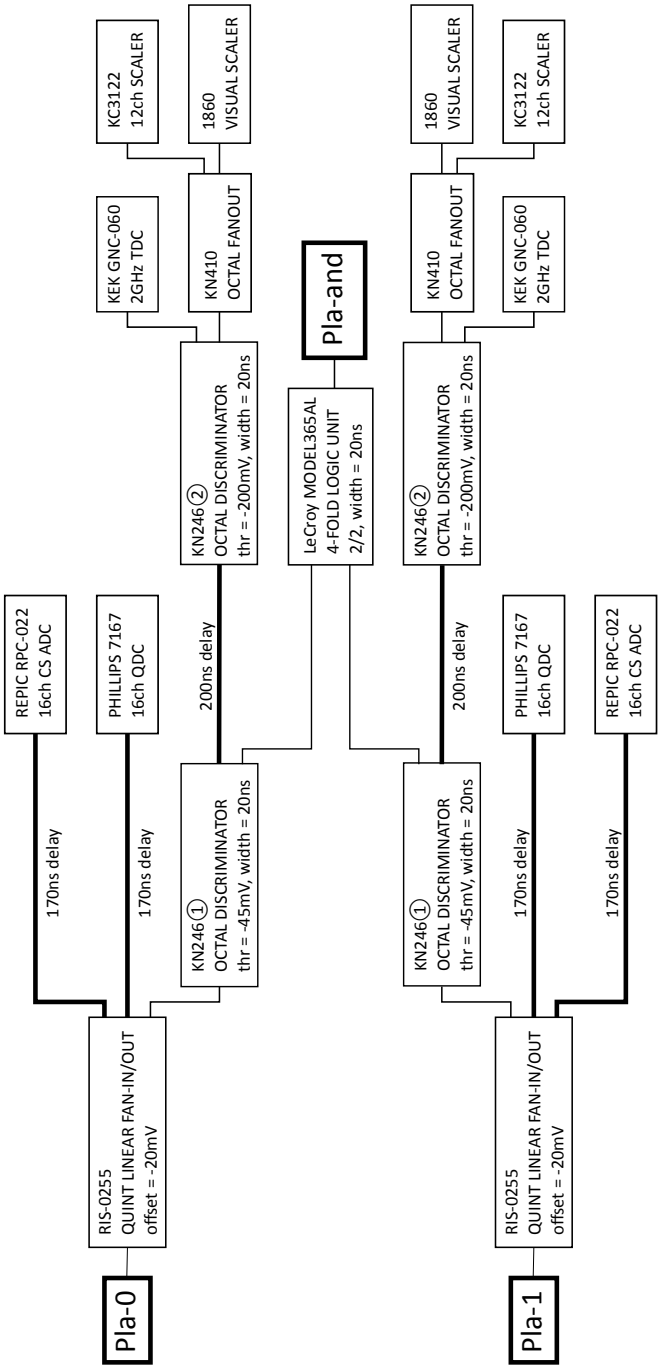

Figure 2.37: Circuit diagram for plastic scintillator system.

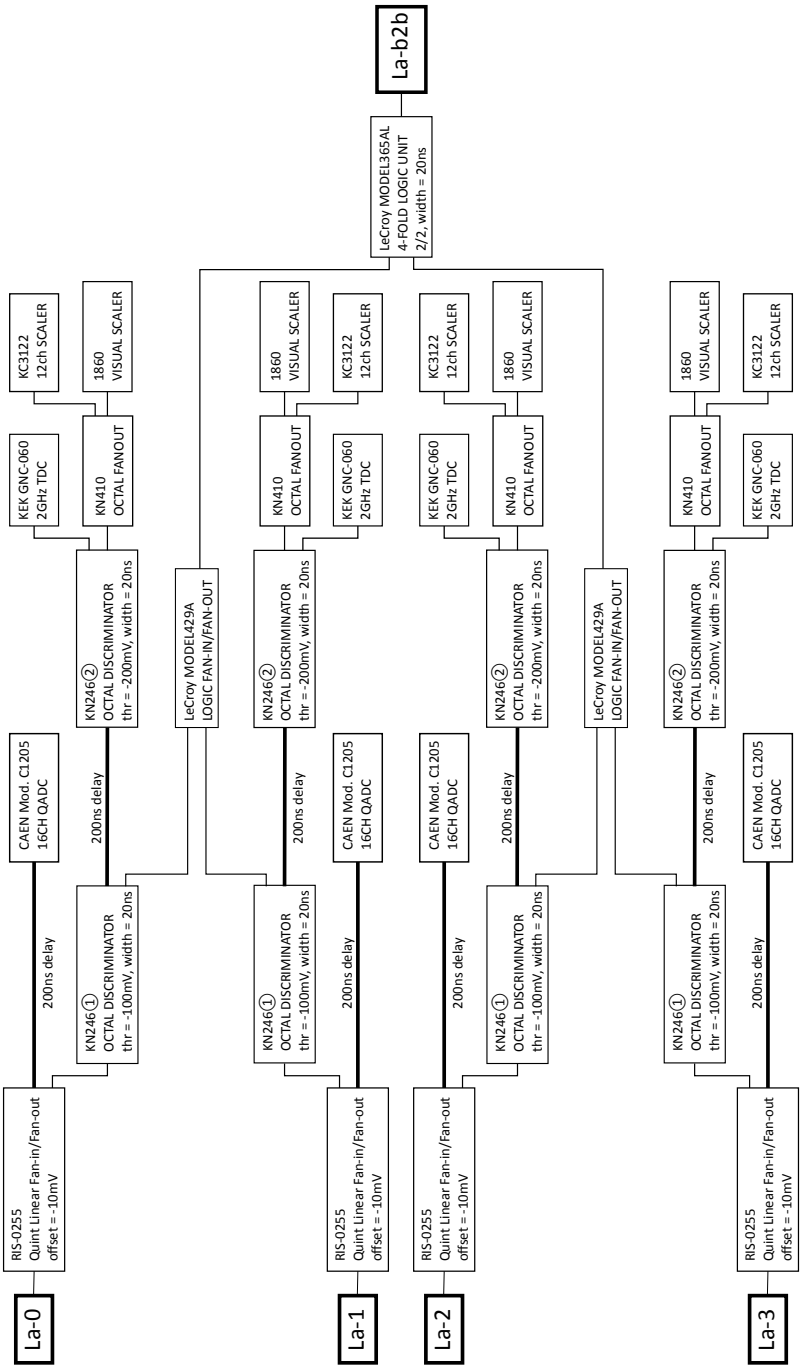

Figure 2.38: Schematic diagram of electronics for γ-ray detector system.

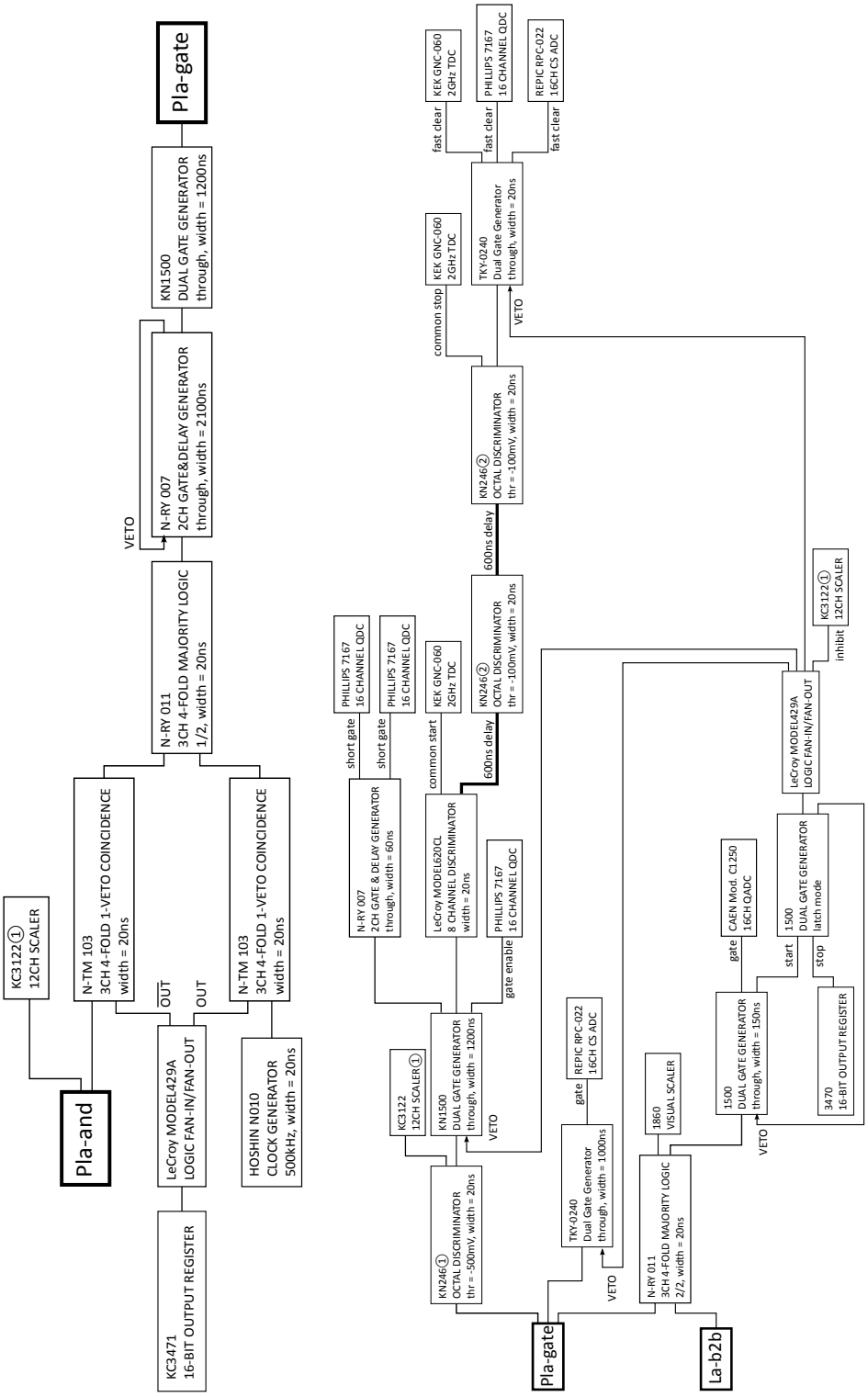

Figure 2.39: Schematic diagram of electronics for trigger system.

Chapter 3

Analysis

This chapter is organized as follows. First, A summary of acquired data is described. The data calibration and offline trigger selections are described next. The transition signals are obtained after some event selections. The reaction cross-section $\sigma(\omega)$ at one frequency point is obtained by comparing this signal amount with a Monte Carlo simulation. Then, $\sigma(\omega)$ is fitted by a Breit-Wigner function. Finally, systematic uncertainties are considered to obtain a result.

3.1 Acquired Data

Table 3.1 summarizes acquired data for analysis. This experiment was performed from May to December in 2013. Data sets are divided into 12 RUNs corresponding to different frequencies and power conditions. The RUN with the same frequency is named to have the same alphabet. We measured 201.83 GHz, 203.51 GHz, 205.31 GHz, 202.64 GHz, 204.56 GHz, and 203.00 GHz (203.25 GHz) in chronological order. Reference RUNs (B-0, C-0, D-0, E-0, F-0) were also acquired without resonating the Fabry-Pérot cavity to check systematic troubles. A decrease of the trigger rate in chronological order is due to contamination of neopentane gas to the acrylic light-guide and the plastic scintillator. Corrections of this effect is described in Sec. 3.3.2 and Sec. 3.4.4.

Data for each RUN are divided into some SETs by 30 minutes, and pedestal data are taken between two SETs. Calibration including some corrections are carried out for each SET. This short time (30 min) for each DAQ guarantees that fluctuation and drift of the measured quantities by environments do not propagate over one SET.

A gyrotron is in pulse operation of duty ratio 30% and a repetition rate 5 Hz, and background levels are slightly different between beam ON and OFF. Data analysis was carried out separately for beam ON and OFF events. Then, the difference is assigned as systematic uncertainties (It turns out to be negligibly small compared with other systematic uncertainties in Sec. 3.5.4).

RUN ID	frequency	power	date (dd/mm)	live time	trigger rate
A-1	201.83 GHz	21.6 kW	14/05-15/05	6.7×10^4 sec	667 Hz
A-2	201.83 GHz	22.2 kW	15/05-16/05	6.7×10^4 sec	669 Hz
B-0	202.64 GHz	0.0 kW	28/09	7.0×10^4 sec	531 Hz
B-1	202.64 GHz	23.4 kW	26/09-28/09	1.1×10^5 sec	540 Hz
C-0	203.25 GHz	0.0 kW	12/12	7.2×10^4 sec	485 Hz
C-1	203.00 GHz	20.6 kW	03/12-04/12	6.6×10^4 sec	494 Hz
C-2	203.25 GHz	16.8 kW	04/12-05/12	6.8×10^4 sec	489 Hz
C-3	203.25 GHz	24.5 kW	10/12-11/12	9.9×10^4 sec	491 Hz
D-0	203.51 GHz	0.0 kW	02/08	2.6×10^4 sec	608 Hz
D-1	203.51 GHz	36.5 kW	25/07-27/07	7.2×10^4 sec	627 Hz
D-2	203.51 GHz	67.4 kW	01/08	1.2×10^4 sec	627 Hz
D-3	203.51 GHz	30.9 kW	01/08	1.3×10^4 sec	628 Hz
D-4	203.51 GHz	19.0 kW	01/08-02/08	1.4×10^4 sec	616 Hz
D-5	203.51 GHz	79.3 kW	02/08	1.3×10^3 sec	610 Hz
E-0	204.56 GHz	0.0 kW	14/10-15/10	2.3×10^5 sec	530 Hz
E-1	204.56 GHz	14.5 kW	12/10-13/10	6.1×10^4 sec	526 Hz
E-2	204.56 GHz	24.6 kW	14/10	6.0×10^4 sec	530 Hz
F-0	205.31 GHz	0.0 kW	14/09	5.8×10^4 sec	530 Hz
F-1	205.31 GHz	23.8 kW	13/09-14/09	1.0×10^5 sec	565 Hz
F-2	205.31 GHz	23.4 kW	16/09-17/09	8.0×10^4 sec	598 Hz
G-0	180.59 GHz	40.5 kW	16/10-18/10	1.2×10^5 sec	523 Hz

Table 3.1: Data sets for analysis

3.2 Calibration and Offline Trigger

3.2.1 Energy Calibration and Correction of the Plastic Scintillator

Energy information of the plastic scintillator was calibrated to the number of photoelectrons (p.e.) detected with a PMT. Two charge data, measured with a short-gate (60 ns) and a long-gate (1000 ns), were independently processed in this calibration. Charge difference of these two were used to reduce accidental events in Sec. 3.3.2.

Charge miscollection of the short-gate energy depending on the signal amplitude was corrected to obtain the original signal amplitude. Six histograms of the long-gate energy were prepared for each short-gate energy divided into 5 p.e. width from 15 p.e. to 45 p.e., and were fitted with Landau distributions. Then, peaks of the Landau distributions were fitted by a second polynomial function to obtain the most probable charge miscollection with the short-gate. Figure 3.1 shows a 2D energy plot of the plastic scintillator before and after the correction.

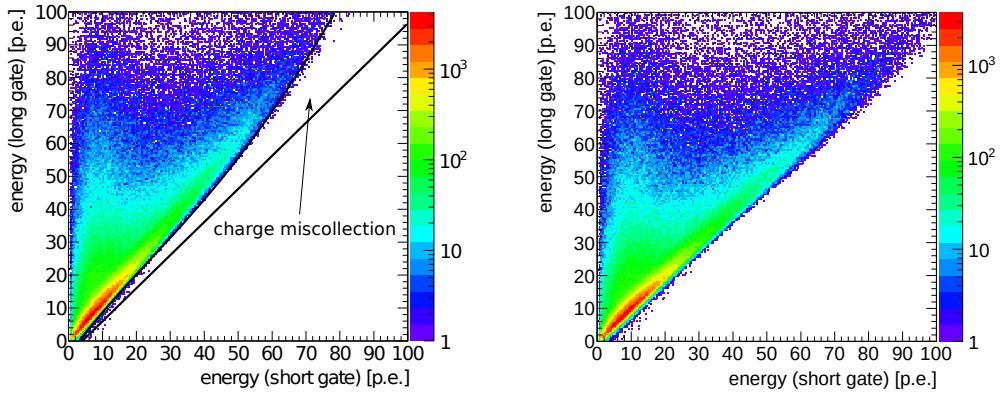

Figure 3.1: 2D plot of the plastic scintillator energy measured with the short-gate and the long-gate. (left) Before the charge correction. (right) After the correction.

3.2.2 Energy Calibration of the $LaBr_3$(Ce) Scintillator

Energy information of $LaBr_3$ (Ce) crystal scintillators was calibrated to make a positron annihilation peak become 511 keV. Pedestal peaks and annihilation peaks were fitted by Gaussian functions. Figure 3.2 shows a calibrated spectrum of a single detector (La-0). Fitted resolutions are summarized in Table 3.2.

3.2.3 Time Calibration

An absolute scale of the TDC (KEK GNC-060) was determined by an external clock source of 2 GHz (accuracy is 1 ppm). A full range of a time spectrum

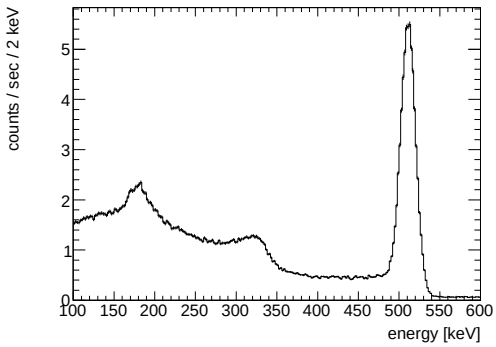

Figure 3.2: Energy spectrum of a $LaBr_3$ (Ce) scintillator (La-0).

Number	σ_{pedestal}	σ_{511}
La-0	0.62 keV	9.00 keV
La-1	0.59 keV	7.84 keV
La-2	0.60 keV	8.01 keV
La-3	0.53 keV	8.46 keV

Table 3.2: Energy resolution of $LaBr_3$ (Ce) crystal scintillators

was determined by a common stop signal delayed 1200 ns from a common start signal. To determine of the time origin, we made use of the prompt events fitted by a Gaussian function. Since the prompt peak consists of p-Ps decay, positron annihilation, and others, it appears as a sharp peak and exactly stands at decay time $t = 0$. Time walk corrections described in Sec. 3.2.4 and Sec. 3.2.5 were also carried out to accurately calibrate time spectrum.

3.2.4 Time-Walk Correction of the $LaBr_3$(Ce) Scintillator

Signal risetime depends on its amplitude, and results in time walk of $LaBr_3$(Ce) signals as shown in the left side of Fig. 3.3. Time-walk was corrected to obtain a proper time spectrum with the following method. Time histograms were prepared for each energy divided by 25 keV from 100 keV to 600 keV, and each prompt peak was fitted by a Gaussian function. Fitted centers were then fitted by

$$f(x) = p_0 + \frac{p_1}{E} + p_2 E, \tag{3.1}$$

where E denotes the energy deposit in the $LaBr_3$(Ce) scintillator. The correction value for each energy was determined by this function, and the result of this correction is shown in the right side of Fig. 3.3

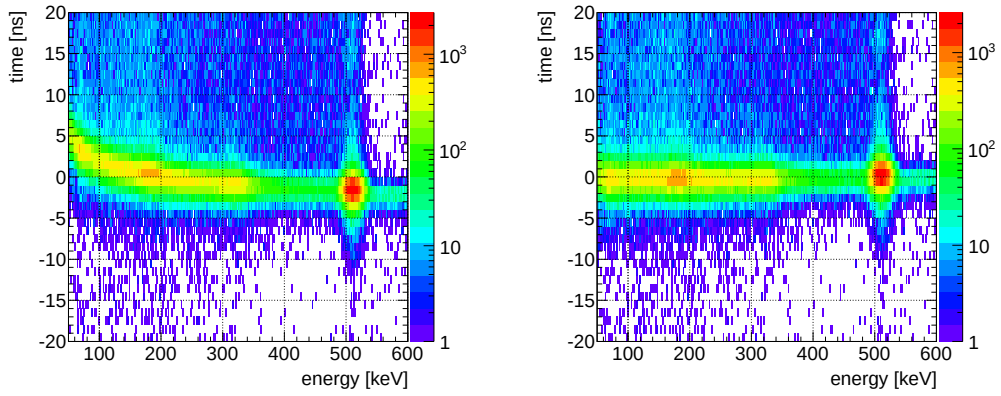

Figure 3.3: 2D plots of time vs energy deposited in one $LaBr_3$(Ce) scintillator. (left) Before the time-walk correction. (right) After the correction.

3.2.5 Time-Walk Correction of the Plastic Scintillator

There is also a non-negligible time lag in plastic-scintillator signals as shown in the left figure of Fig. 3.4. Time-walk corrections of the plastic scintillator were also carried out. Pla-0 and Pla-1 signals were combined and divided into 16 regions from

4 p.e. to 100 p.e. Prompt time peaks for these regions were fitted by Gaussian functions. The peak centers were fitted by

$$f(E) = p_0 + \frac{p_1}{E} + p_2 E + p_3 E^2, \tag{3.2}$$

where E denotes the number of summed photoelectrons of Pla-0 and Pla-1. The correction value for each energy was determined by this function, and the result of this correction is shown in the right side of Fig. 3.4

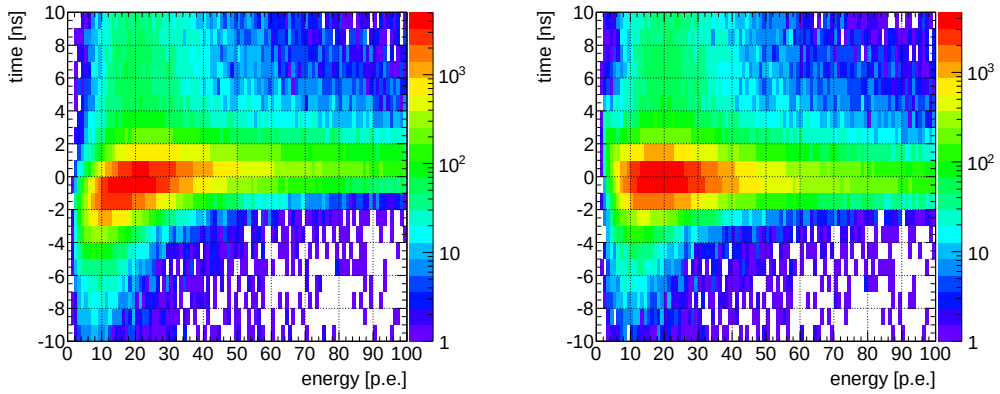

Figure 3.4: 2D plots of time vs energy deposited in the plastic scintillator. (left) Before the time-walk correction. (right) After the correction.

3.2.6 Offline Trigger Cuts

Offline trigger cuts are required before event selections for the transition signal.

e^+ tagging

A threshold for energy deposits in the plastic scintillator was set to 1 p.e. both for Pla-0 and Pla-1. And both two, Pla-0 and Pla-1 of the short-gate, were required to balance with each other.

$$\left|\sqrt{E_{\mathrm{Ps-0}}} - \sqrt{E_{\mathrm{Ps-1}}}\right| < 3\sigma \tag{3.3}$$

These requirements eliminate cross-talk noise and events in which a positron hits an edge of the scintillator. Figure 3.5 shows the 2D plot of Pla-0 and Pla-1 with the e^+ tagging condition. Times of signal detection with Pla-0 and Pla-1 were also required to coincide within 3 standard deviations as shown in the left side of Fig. 3.6.

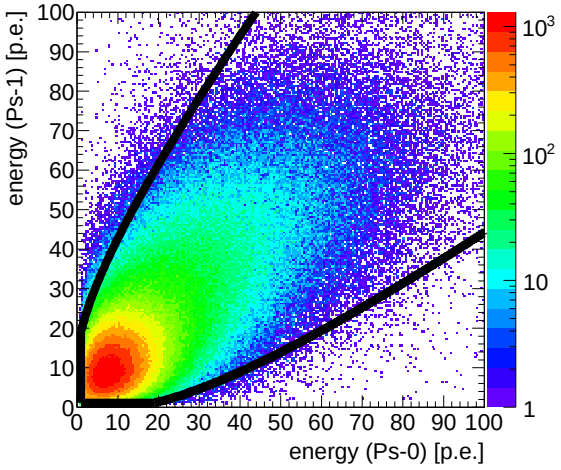

Figure 3.5: 2D energy spectrum of plastic scintillator. The region inside black lines is selected.

Back-to-back γ-ray Hits

It was required that γ rays hit only two back-to-back $LaBr_3(Ce)$ scintillators whose energy deposits were over 100 keV. Events in which energy deposits of over three

scintillators exceed 100 keV were eliminated. These conditions reduce contamination of three γ-ray decay of o-Ps and accidental γ rays (1275 keV and 511 keV) from the positron source. Times of signal detection with back-to-back $LaBr_3(Ce)$ crystals were also required to coincide within 3 standard deviations as shown in the right figure of Fig. 3.6.

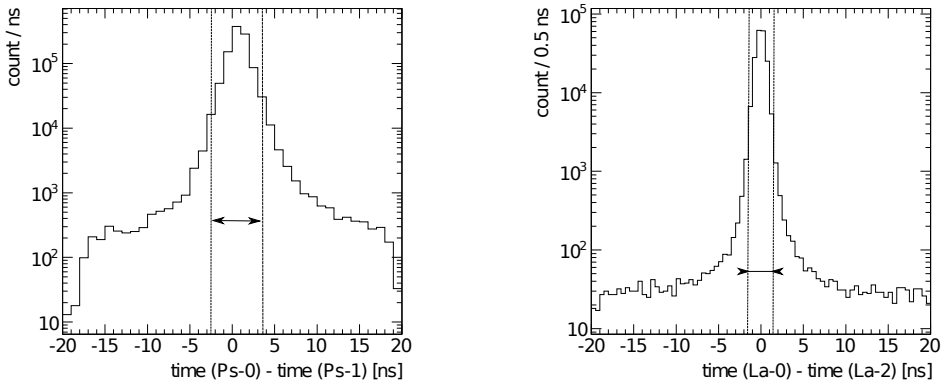

Figure 3.6: Time coincidence. (left) Between Pla-0 and Pla-1. (right) Between La-0 and La-2. Cut region is shown as dashed black lines.

An example of event rates after each selection is summarized in Table 3.3. About 59 % of the online-triggered events pass the offline trigger cuts.

selection	rate [Hz]
online trigger	667.34(18)
e^+ tagging : energy cut	660.91(18)
e^+ tagging : time coincidence	618.89(17)
back-to-back γ-ray hits : energy cut	410.12(14)
back-to-back γ-ray hits : time coincidence	391.33(14)

Table 3.3: Summary of the event rates by offline trigger cuts (RUN ID A-1).

3.3 Event Selection

Event selections are needed to measure the amount of the direct transition signals. The signal is delayed two back-to-back γ rays of 511 keV. Three selections were required:

- Time window (delayed coincidence)
- Accidental rejection
- γ-ray energy cut

There are two remaining backgrounds after these three event selections: three γ-ray contamination and pick-off annihilation. They all are discussed in the following sections.

3.3.1 Time Window

The offline-triggered data contain backgrounds of a prompt peak at $t = 0$ and accidental events as shown in Fig. 3.7. They were eliminated with a time window from 50 ns to 250 ns. This range of the time window was determined with Monte Carlo simulations to obtain the best signal-to-noise ratio (S/N) in case of 30 kW accumulation. S/N was improved by factor of six by this cut.

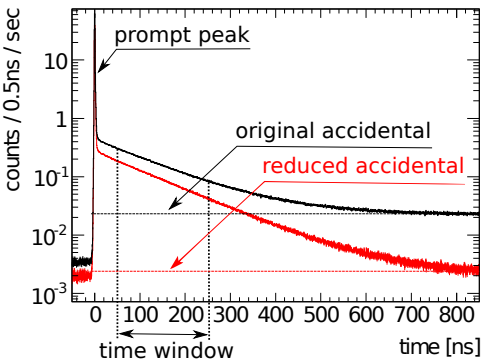

Figure 3.7: Time spectrum obtained by time difference of the $LaBr_3(Ce)$ signal and plastic scintillator one. Time window for delayed coincidence is shown as a region between two black dashed lines. The black and red solid lines show before and after accidental rejection, respectively.

3.3.2 Accidental Rejection

A part of accidental background due to pileup events of the plastic scintillator still remains after requiring the time window (Fig. 3.7). We made use of charge difference of the plastic scintillator signal measured with the short-gate and the long-gate. The left side of Fig. 3.8 shows a scatter plot of energy deposits measured with the short-gate and the long-gate. The long-gate stores more charges than the short-gate in case of accidental pileup events (shown as a triangle region) while these two charges balance with each other in signal events. A cut condition used was

$$-5\sigma_{\mathrm{long-gate}} < E_{\mathrm{long-gate}} - E_{\mathrm{short-gate}} < 3\sigma_{\mathrm{long-short}}. \tag{3.4}$$

as shown in the right figure of Fig. 3.8. The peak width of the $E_{\mathrm{long-gate}} - E_{\mathrm{short-gate}}$ spectrum changes in chronological order because contamination of neopentane to the light-guide gradually decreases amount of light from the plastic scintillator. Table 3.4 summarizes $\sigma_{\mathrm{long-short}}$ of each frequency.

Figure 3.7 compares time spectra before and after the accidental rejection cut. S/N was enhanced by a factor of two. Events in an accidental time window from 750 ns to 850 ns were subtracted from that in the signal time window (from 50 ns to 250 ns) to reduce the remaining accidental background which was very small.

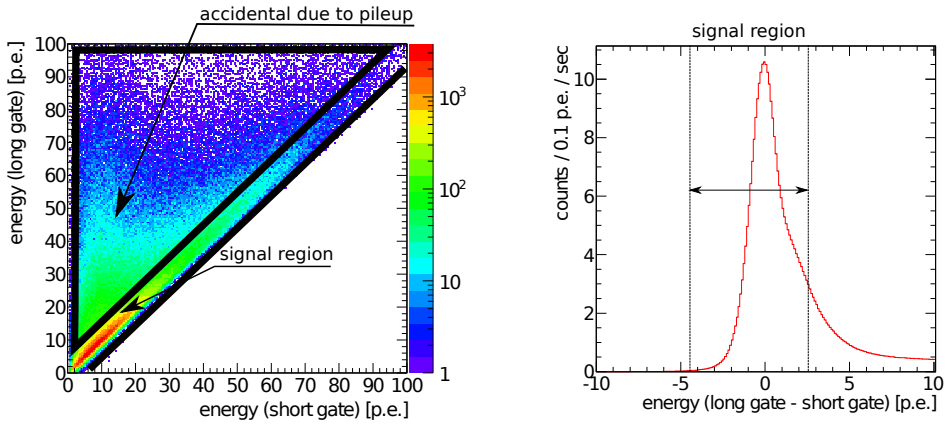

Figure 3.8: Cut condition of accidental rejection of the plastic scintillator. (left) 2D plots of energy deposits measured with the short-gate and the long-gate. (right) Difference of energy deposits measured with the short-gate and the long-gate. The signal region is expressed as a region between two black lines.

frequency	ID	$\sigma_{\mathrm{long-short}}$
201.83 GHz	A-1, A-2	0.90 p.e.
202.64 GHz	B-0, B-1	0.47 p.e.
203.00 GHz	C-0, C-1, C-2, C-3	0.53 p.e.
203.51 GHz	D-0, D-1, D-2, D-3, D-4, D-5	0.73 p.e.
204.56 GHz	E-0, E-1, E-2	0.50 p.e.
205.31 GHz	F-0, F-1, F-2	0.63 p.e.
180.59 GHz	G-0	0.51 p.e.

Table 3.4: Summary of the peak width of $\sigma_{\mathrm{long-short}}$.

3.3.3 γ-ray Energy Cut

Large background from three γ-ray contamination exists without energy cuts. An energy cut around 511 keV was required

$$511\,\mathrm{keV} - 2\sigma_{511} < E_\gamma < 511\,\mathrm{kev} + 3\sigma_{511}. \tag{3.5}$$

Figure 3.9 shows predicted energy spectra required this cut only at the *opposite* side of the back-to-back pairs. Four back-to-back pairs (La-0, La-2) (La-0, La-3) (La-1, La-2) (La-1, La-3) were combined (Fig. 2.29). When the cut condition was also required at *this* side of the pairs (shown as dashed lines in Fig. 3.9), S/N was improved by a factor of 70 compared with no energy cuts.

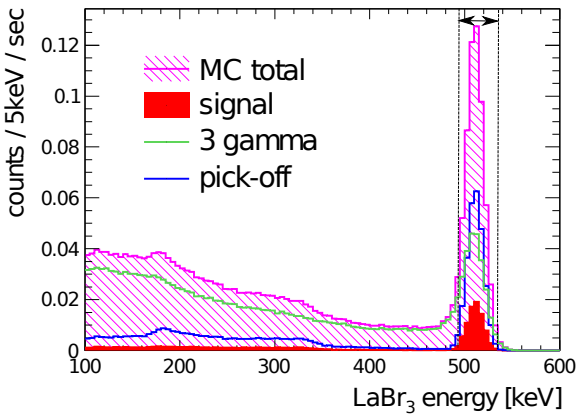

Figure 3.9: Expected energy spectrum of $LaBr_3$ (Ce) scintillators with Monte Carlo simulation. f =203.4 GHz and P_{acc}=20 kW. 511 keV is required at the opposite side of the back-to-back pairs.

3.3.4 Direct Transition Signal and Background Estimation

Although we required some event selections, remaining backgrounds shown in Fig. 3.9 are still dominant contribution to the 511 keV peak, and the transition signal is about 10% of total events. Three γ-ray contamination background is due to decays of non-transiting o-Ps. According to kinematics, a part of this decay is very similar to two γ decays of 511 keV, and is inseparable with non-segmented crystals. Pick-off background is caused by annihilation between a positron in o-Ps and an electron in a gas molecule. This is mainly two γ-ray annihilation, and inevitable in use of gas as an electron source.

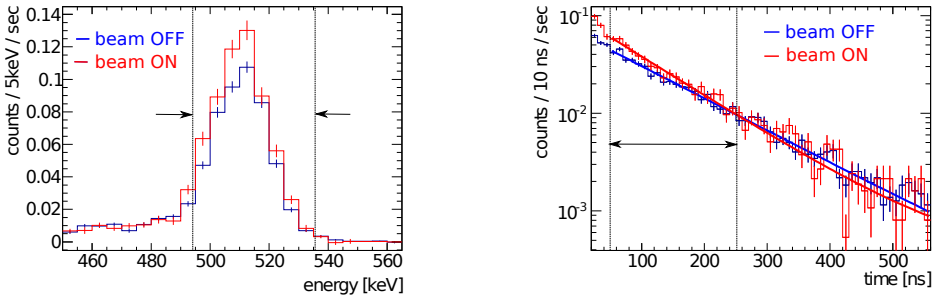

Figure 3.10: Histograms after event selections. Histograms of RUN D-2 are shown as an example. (left) Energy spectrum. (right) Time spectrum. Solid lines show the best fit.

Remaining backgrounds were estimated with real data. The gyrotron was in pulse operation of duty ratio 30% and a repetition rate 5 Hz. Background events were obtained with beam OFF events, and the transition signal was obtained by subtracting OFF rate from ON rate. Since beam ON and OFF are within 200 ms sequentially, one can safely ignore that environmental conditions such as temperature do not change between beam OFF and ON.

Figure 3.10 compares energy and time spectra of beam OFF and beam ON events. The beam OFF and ON spectra were normalized with the prompt peak of the time spectra, which was consistent with livetime normalization. A clear enhancement around 511 keV for beam ON events was obtained (the left side). At the same time, lifetime of beam ON events decreases from beam OFF events because of the transition (the right side). The amounts of the direct transition signals for each RUN are summarized in Table 3.5. The transition was observed in high-power RUNs, and not in 0 kW RUNs. No signals at far off-resonance point with high power (G-0) guarantees that there is no fake signals from unexpected systematic effects. Corrections of power fluctuations are needed to obtain the proper resonance curve (the reaction cross-section $\sigma(\omega)$). This method is discussed in the next section.

RUN ID	frequency	power	ON rate	OFF rate	ON − OFF
A-1	201.83 GHz	21.6 kW	520.2(5.2)	498.9(3.3)	21.2(6.1)
A-2	201.83 GHz	22.2 kW	525.0(5.2)	510.0(3.4)	14.9(6.2)
B-0	202.64 GHz	0.0 kW	340.5(4.2)	331.8(2.7)	8.8(5.0)
B-1	202.64 GHz	23.4 kW	383.3(3.5)	361.6(2.2)	21.7(4.2)
C-0	203.25 GHz	0.0 kW	414.6(7.5)	406.9(4.9)	7.8(8.9)
C-1	203.00 GHz	20.6 kW	379.5(4.5)	350.5(2.9)	29.0(5.4)
C-2	203.25 GHz	16.8 kW	362.0(4.4)	337.4(2.8)	24.6(5.2)
C-3	203.25 GHz	24.5 kW	397.0(3.8)	358.1(2.4)	38.9(4.5)
D-0	203.51 GHz	0.0 kW	414.6(7.5)	406.9(4.9)	7.8(8.9)
D-1	203.51 GHz	36.5 kW	499.0(4.9)	452.5(3.1)	46.5(5.8)
D-2	203.51 GHz	67.4 kW	547.8(12.4)	454.5(7.3)	93.3(14.4)
D-3	203.51 GHz	30.9 kW	481.4(11.1)	432.3(7.0)	49.1(7.0)
D-4	203.51 GHz	19.0 kW	460.3(10.7)	423.7(6.6)	36.6(12.6)
D-5	203.51 GHz	79.3 kW	495.2(11.5)	416.4(7.0)	78.8(13.4)
E-0	204.56 GHz	0.0 kW	369.5(4.8)	374.8(3.1)	−5.3(5.7)
E-1	204.56 GHz	14.5 kW	372.1(4.7)	358.9(3.0)	13.1(5.6)
E-2	204.56 GHz	24.6 kW	408.9(5.0)	390.3(3.2)	18.6(5.9)
F-0	205.31 GHz	0.0 kW	399.5(7.5)	395.4(4.9)	4.1(8.9)
F-1	205.31 GHz	23.8 kW	431.7(3.8)	412.6(2.5)	19.1(4.6)
F-2	205.31 GHz	23.4 kW	420.1(4.3)	416.4(2.8)	3.7(5.1)
G-0	180.59 GHz	40.5 kW	374.4(3.4)	375.9(2.2)	−1.7(4.3)

Table 3.5: The amount of the transition signal. Rates are shown in mHz.

3.4 Analysis for Ps-HFS

In this section, we consider space-time fluctuations of accumulated power and detection efficiency to obtain the reaction cross-section curve of Ps-HFS. A Monte Carlo simulation (MC) is introduced to estimate detection efficiency. The transition signal (the ON − OFF rate) is affected by the decreasing trigger rate; therefore, S/N (normalized by the OFF rate) is compared with MC. Ps-HFS, lifetime of p-Ps, and the Einstein A coefficient of the Ps-HFS transition are simultaneously determined. This is the first direct measurement of Ps-HFS and p-Ps lifetime.

3.4.1 Preparation of MC Samples

Geant4 simulations were performed after the experiments with proper condition of temperature and gas pressure. To save time, MC is divided into two parts. Firstly, stopping positions of positrons were simulated (10^6 events) as shown in Fig. 3.11. Secondly, γ rays were simulated from the obtained distribution of the

positron-stopping position. We simulated two γ annihilation for signal and pick-off events (25×10^6 events) and three γ annihilation for o-Ps events (500×10^6 events). Different sets of MC were prepared for all RUNs.

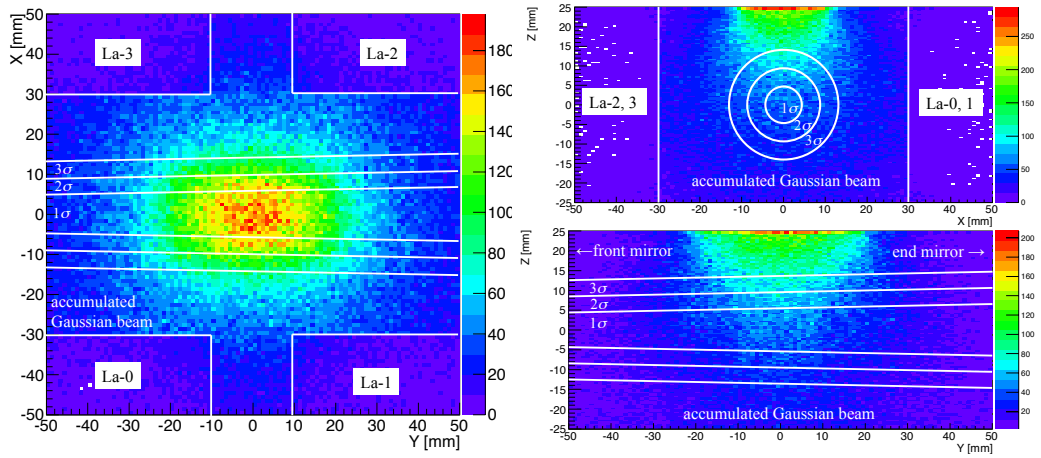

Figure 3.11: Position distribution of Ps formation with MC. (left) Top view. (top right) Cross-sectional view of the Fabry-Pérot cavity. (bottom right) Side view of the Fabry-Pérot cavity. See Fig. 2.29 and Fig. 2.30 as a reference.

3.4.2 Correction of Space Fluctuation

Shape effects of the Gaussian beam and the standing-wave reduce transition probability compared with an expectation with averaged power. The shape of the Gaussian beam is shown in Fig. 3.11 with white lines. A detection efficiency of γ rays was estimated by making different MC histograms corresponding to the position of Ps formation divided into 25 parts from 0σ to 5σ, and summing them with power weight of the Gaussian distribution. The shape of the standing-wave was estimated by simply calculating power weight of $2\sin^2 ky$ and was integrated because this structure is so small (750 μm) that no detectors are sensitive to its geometrical effect.

3.4.3 Correction of Time Fluctuation

Figure 3.12 shows a typical pulse shape recorded with 500 Hz. As is described in Sec. 2.2.4, the electron beam current I_b was stabilized with a feed-back control of the heater voltage. Input power to the Fabry-Pérot cavity V_in was also more or less stable under steady-state gyrotron oscillation with constant I_b. Transmitted power V_tr integrated in one pulse was stabilized by the control of cavity length (Fig. 2.27). However, as shown in Fig. 3.12, V_tr fluctuates in one pulse because of unstable gyrotron frequency (Fig. 2.6). This fluctuation reduces transition probability, and

depends on different gyrotron conditions for each RUN. This effect was estimated by taking a histogram of V_{tr} sampled per 2 ms. Figure 3.13 shows two examples of the obtained histogram filled per 2 ms of this power fluctuation. Frequency linewidth of the gyrotron was stable in RUN A-1 (left), but quite unstable in RUN D-1 (right). The transition probability was corrected by weighting this histogram.

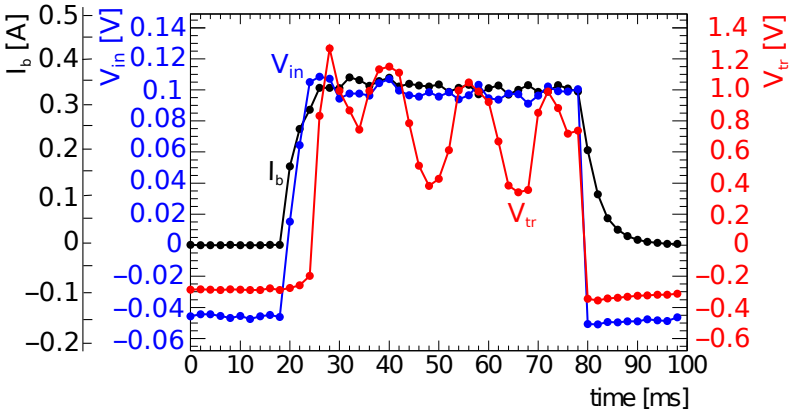

Figure 3.12: Pulse shape of detected power. Beam current I_{b} (black), monitored incident power V_{in} (blue), and transmitted power V_{tr} (red) are shown together.

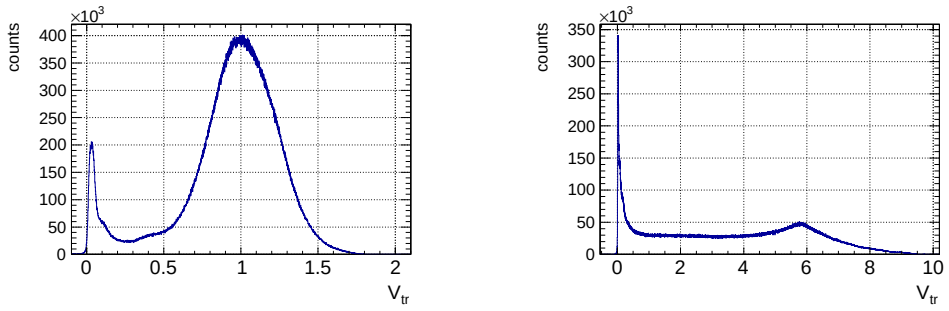

Figure 3.13: Histogram of accumulated power fluctuation in pulse. (left) RUN A-1. (right) RUN D-1.

3.4.4 Calculation of the Reaction Cross-section

Reaction cross-sections of each RUN were calculated by comparing the ratio of transition signals with MC predictions. The obtained detection efficiencies of 2γ rays and 3γ rays with MC are expressed as $\eta_{2\gamma}$ and $\eta_{3\gamma}$, respectively. We also

introduce fraction of the signal ($F_{\rm sig}$) and background, pick-off ($F_{\rm pick}$) and o-Ps ($F_{\rm o\text{–}Ps}$), using Eq. (1.26), (1.27), and (1.28).

$$F_{\rm sig} = \frac{1}{4}\Gamma_{\rm tran}(P)\int_{t0}^{t1} dtN_{1,0} \tag{3.6}$$

$$F_{\rm pick} = \frac{1}{4}\Gamma_{\rm pick}\sum_{m=-1,0,1}\left[\int_{t0}^{t1} dtN_{1,m}\right] \tag{3.7}$$

$$F_{\rm o\text{–}Ps} = \frac{1}{4}\Gamma_{\rm o\text{–}Ps}\sum_{m=-1,0,1}\left[\int_{t0}^{t1} dtN_{1,m}\right] \tag{3.8}$$

Coefficient 1/4 means that the number of each $|S,m\rangle$ state formed is the same provided Ps is unpolarized. These three fractions are functions of accumulated power because $\Gamma_{\rm tran}$ and $N_{1,0}$ depend on power. Predicted S/N is expressed as

$$n_{\rm ON} = \sum_{\rm P} w_{\rm P}\left\{\eta_{2\gamma}\left[F_{\rm sig}(P)+F_{\rm pick}(P)\right]+\eta_{3\gamma}\cdot F_{\rm o\text{–}Ps}(P)\right\} \tag{3.9}$$

$$n_{\rm OFF} = \eta_{2\gamma}\left[F_{\rm sig}(0)+F_{\rm pick}(0)\right]+\eta_{3\gamma}\cdot F_{\rm o\text{–}Ps}(0) \tag{3.10}$$

$$\mathrm{S/N(MC)} = \frac{n_{\rm ON}-n_{\rm OFF}}{n_{\rm OFF}}, \tag{3.11}$$

where $\sum_{\rm P}$ means corrections of power fluctuation with weight $w_{\rm P}$ described in Sec. 3.4.2 and Sec. 3.4.3. We solved equation of S/N (data listed in Table 3.5) = S/N (MC) taking a reaction cross-section as an unkown variable. The results are listed in Table 3.6. They were fitted by a Breit-Wigner function defined by Eq. (1.32). Figure 3.14 shows the fitting result with statistical errors only. Correlations among three fitting variables ($\Delta_{\rm Ps}^{\rm HFS}$, $\tau_{\rm p\text{–}Ps}$, A) are shown in Fig. 3.15 We estimated the fitting errors as the maximum and the minimun of the correlation region of one standard deviation (red).

Frequency [GHz]	σ [kb]
180.59(10)	−0.45(1.21)
201.83(02)	8.88(2.50)
202.64(04)	18.22(4.99)
203.00(04)	34.18(10.9)
203.25(05)	38.66(7.33)
203.51(02)	29.09(6.02)
204.56(05)	13.07(4.17)
205.31(04)	5.81(2.22)

Table 3.6: Summary of the reaction cross-section.

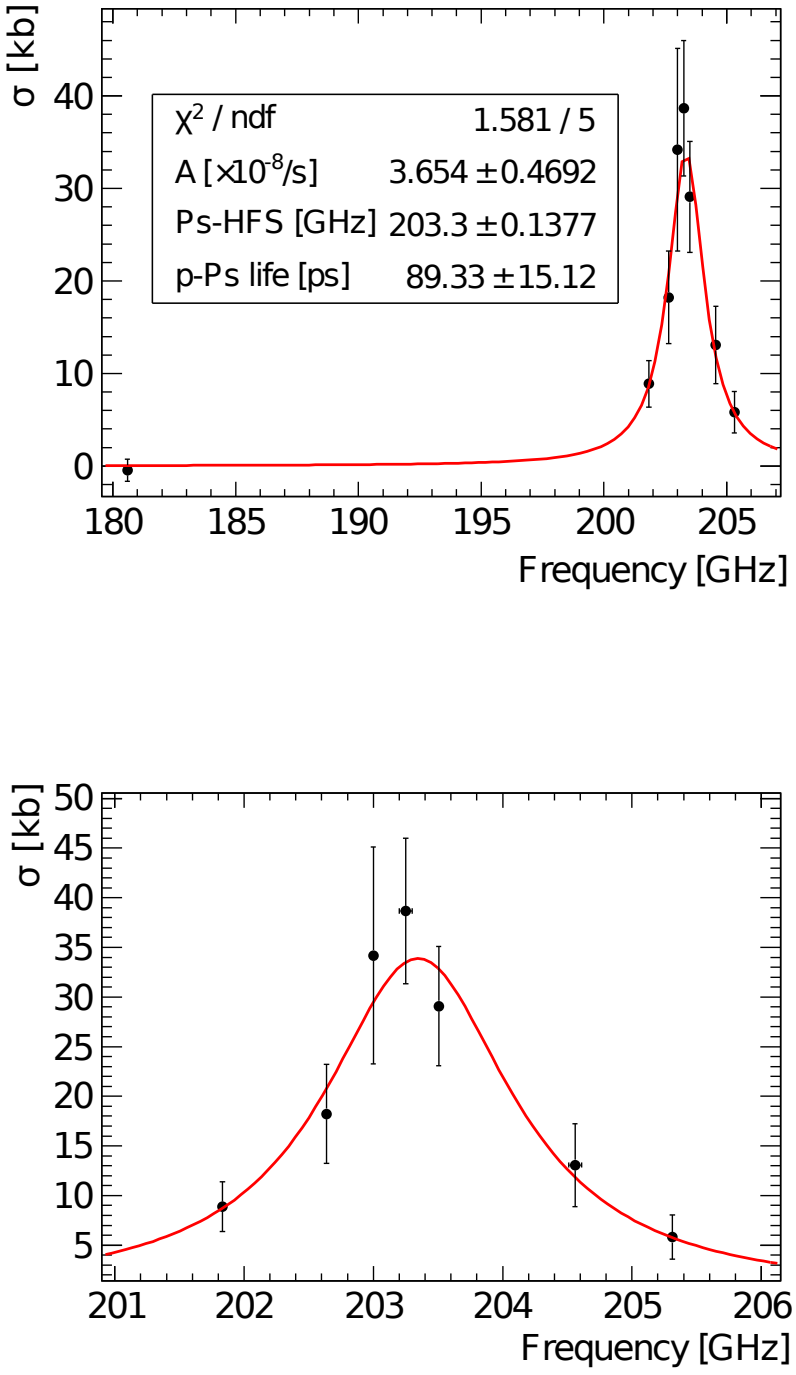

Figure 3.14: Fitting result of measured cross-section of Ps-HFS transition. (top) Full range. (bottom) Enlarged view near the resonance.

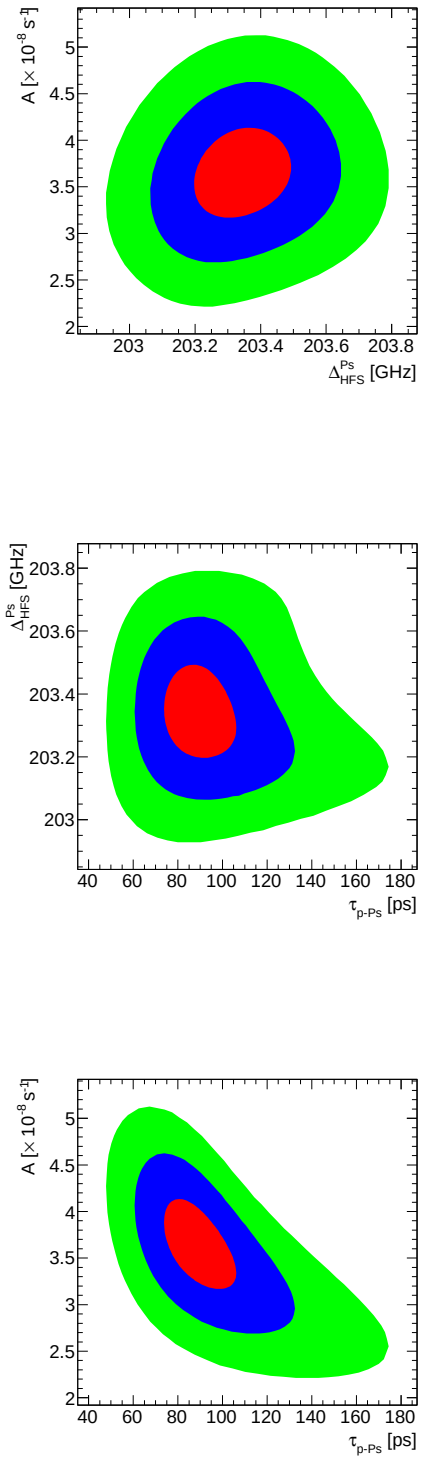

Figure 3.15: Correlation among three fitting variables. The red, blue, green regions are one, two, three standard deviations, respectively.

3.5 Systematic Errors

Systematic errors for the transition signal of each RUN are considered. They are categorized into four types:

- power estimation uncertainty
- gas effect
- Monte Carlo simulation
- another

They are described in the following sections.

3.5.1 Power Estimation Uncertainty

A systematic uncertainty from the power estimation has been already discussed in Sec. 2.2.3 and summarized in Table 2.5. Relative accuracy is better than 21% except for the far off-resonance point F-0. An effect for the Ps-HFS value was estimated by scanning C of each frequency with an asymmetric Gaussian distribution.

3.5.2 Gas Effect

Ps Formation Probability

In this experiment, it turned out that the Ps formation probability is enhanced in use of nitrogen under high-power millimeter-wave radiation (See Sec. 2.3.2). This enhancement can be a systematic error if it still exists in case of neopentane. An energy cut from 360 keV to 450 keV is free from the Compton scattering of 511 keV γ rays, and is required to study an increase of o-Ps.

In off-resonance RUNs (ID = A and F) and the far frequency point G-0, S/N is zero consistent and no Ps increases are observed. In on-resonance RUNs (ID D), a decrease from the Ps-HFS transition o-Ps $\rightarrow$ p-Ps hides the effect of Ps increase. The systematic uncertainty was estimated to be $-0.1\ 06(76)\%$ with G-0 data which is free from the signal contamination. An increase of Ps formation probability may depend on frequency and power. Frequency dependence can be estimated as (See Eq. (B.3))

$$\frac{\overline{\delta E(203\ \mathrm{GHz})}}{\overline{\delta E(180\ \mathrm{GHz})}} \sim \frac{(2\pi \cdot 180\ \mathrm{GHz})^2 + \omega_\mathrm{c}^2}{(2\pi \cdot 203\ \mathrm{GHz})^2 + \omega_\mathrm{c}^2}. \tag{3.12}$$

If we approximate the neopentane molecule as an elastic ball of radius 3.5Å, collision frequency ω_c is about 1 THz at 300 K and 1 atm. The resulting correction factor by frequency change from 180 GHz to 203 GHz is only 0.9. Thus, an increase of Ps formation is zero consistent and negligible.

Pick-off Annihilation Probability

If pick-off annihilation probability depends on beam OFF or ON, it can be a systematic error. The pick-off rate is determined by velocity of Ps, gas density, and the effective electron numbers in a gas molecule which contributes to the annihilation. A neopentane gas molecule does not interact with millimeter-wave radiation at all because it does not have an electric dipole moment (See Table 2.6). Fluctuation of gas density due to heat does not follow a short pulse of gyrotron (60 ms). However, initial velocity of Ps might be affected by millimeter waves because we found positron acceleration by millimeter-wave radiation (See Sec. 2.3.2). Pick-off annihilation probability can be changed by accelerated Ps velocity.

Far off-resonance data of RUN G-0 was used to eliminate signal contamination. We required accidental rejection and Compton free energy selection (from 360 keV to 450 keV). Time spectra were fitted from 50 ns to 850 ns, and obtained pick-off probability $P_{\rm pick} = \Gamma_{\rm pick}/\Gamma_{\rm o\text{-}Ps}$ is

$$P_{\rm pick}({\rm OFF}) = 8.43(17)\% \tag{3.13}$$
$$P_{\rm pick}({\rm ON}) = 8.06(26)\% \tag{3.14}$$

It is consistent with each other. Near off-resonance data (RUN A, F) were also fitted, and no significant differences between beam OFF and ON were observed. Thus, this effect turned out to be negligible in this experiment.

Stark effect

The Ps-HFS value is shifted by the Stark effect due to static electric fields of gas molecules. Since non-thermalization effect can be ignored at the current level of precision, the shifted $\Delta^{\prime {\rm Ps}}_{\rm HFS}$ linearly depends on gas density D as shown in Fig. 3.16

$$\Delta^{\prime {\rm Ps}}_{\rm HFS} = \Delta^{\rm Ps}_{\rm HFS}\left[1 + a(\sigma_{\rm m})D\right], \tag{3.15}$$

where coefficient $a(\sigma_{\rm m})$ is introduced.

Although $a(\sigma_{\rm m})$ of nitrogen (Fig. 3.16) or isobutane was measured in previous experiments, there are no experimental data of $a(\sigma_{\rm m})$ in neopentane gas. We can assume that $a(\sigma_{\rm m})$ is proportional to $\sigma_{\rm m}$ if we ignore non-thermalization effect of Ps (about 10 ppm). An elastic scattering cross-sections $\sigma_{\rm m}$ of nitrogen and neopentane are measured with Doppler-broadening measurements [62]

$$\sigma_{\rm m}^{\rm N_2} = 13.0(0.5)\,{\rm \AA}^2 \tag{3.16}$$
$$\sigma_{\rm m}^{\rm neo} = 228(13)\,{\rm \AA}^2 \tag{3.17}$$

In case of nitrogen gas, the averaged value of $a(\sigma_{\rm m})$ in two independent measurements [30][33] is

$$a^{\rm N_2}(\sigma_{\rm m}) = -28.7(8.7)\ {\rm ppm}\cdot{\rm amagat}^{-1} \tag{3.18}$$

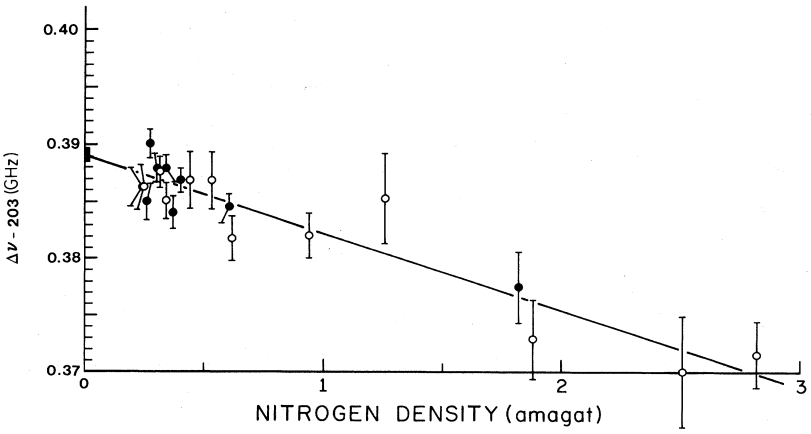

Figure 3.16: Measured Stark shift of $\Delta_{\mathrm{HFS}}^{\mathrm{Ps}}$ vs nitrogen density. The open circles are from [32] and the closed circles are from [33]. The straight line is the best fit [33]

As a result, the value of this effect to neopentane of 1 atm and 300 K is estimated as

$$a^{\mathrm{neo}}(\sigma_{\mathrm{m}}) = a^{\mathrm{N_2}}(\sigma_{\mathrm{m}}) \times \frac{\sigma_{\mathrm{m}}^{\mathrm{neo}}}{\sigma_{\mathrm{m}}^{\mathrm{N_2}}} \times \frac{273}{300} \sim -460 \ \ \mathrm{ppm}. \tag{3.19}$$

The measured Ps-HFS value is corrected by +460 ppm, and ±460 ppm is also assigned as a systematic uncertainty. This is a common systematic error to all RUNs, and was combined at last.

Note that linear extrapolation is invalid if Ps is not well thermalized. This is one of the possible systematic uncertainties in previous measurements (See Sec. 1.5.3) and results in about 10 ppm correction in case of isobutane gas [38]. A similar correction is expected for neopentane because its molecular structure is almost the same as isobutane. It is negligible in this measurement at the current level of precision and should be considered in the future (See Sec. 4.3).

3.5.3 Monte Carlo Simulation

The reaction cross-section was calculated with detection efficiency obtained with the MC simulation. As defined by Eq. (3.11), use of S/N reduces effects from parameters with large uncertainty, such as an absolute source rate, a stopping position in gas, positronium formation probability, or fine structure of energy spectrum. A possible remaining systematic uncertainty is a ratio of detection efficiency $\eta_{2\gamma}/\eta_{3\gamma}$ due to improperly idealized MC modeling. This ratio is nothing but the pick-off annihilation probability P_{pick} of beam OFF events. We estimated systematic errors from MC by comparing pick-off probability obtained from OFF histograms with ones obtained by fitting time spectra. The Compton free energy cut (from 360 keV to 450 keV) and accidental rejection were required to draw time spectra. Table 3.7

summarizes the relative difference of the two pick-off annihilation probabilities. Worst values of the relative difference were assigned as a systematic uncertainty.

RUN ID	frequency	P_{pick} (MC)	P_{pick} (fit)	relative difference
A-1	201.83 GHz	7.46(38)	7.99(18)	6.67(29)%
A-2	201.83 GHz	7.71(39)	7.89(18)	2.34(30)%
B-1	202.64 GHz	7.41(35)	8.50(17)	12.79(23)%
C-1	203.00 GHz	7.84(48)	8.55(21)	8.35(40)%
C-2	203.25 GHz	7.59(47)	9.01(22)	15.78(37)%
C-3	203.25 GHz	8.49(44)	7.91(22)	7.43(34)%
D-1	203.51 GHz	7.96(40)	8.24(18)	3.40(29)%
D-2	203.51 GHz	8.31(92)	8.74(43)	4.89(1.39)%
D-3	203.51 GHz	8.95(98)	7.63(43)	17.25(1.78)%
D-4	203.51 GHz	7.37(80)	8.41(43)	12.40(1.26)%
D-5	203.51 GHz	8.95(99)	9.03(46)	0.88(1.47)%
E-1	204.56 GHz	8.99(53)	9.01(23)	0.25(41)%
E-2	204.56 GHz	7.68(45)	8.32(21)	7.72(38)%
F-1	205.31 GHz	8.75(45)	8.35(16)	4.82(26)%
F-2	205.31 GHz	7.72(39)	8.11(18)	4.79(29)%
G-0	180.59 GHz	7.90(36)	8.43(16)	6.29(23)%

Table 3.7: Comparison of pick-off rate between MC and time spectra.

3.5.4 Another Systematic Uncertainty

Energy Scale and Energy Resolution of γ-ray detectors

If differences of the energy scales and the energy resolutions exist, they make fake signals. In order to estimate this uncertainties, the 511 keV peaks after the energy calibration were fitted again with Gaussian functions. In almost all the RUNs, the difference is zero consistent within statistical uncertainty (less than 2 standard deviation). Three exceptions were found. Since there are 48 samples (12 RUNs and 4 detectors), these three exceptions can be statistical fluctuations. Thus, this effect is negligible in this experiment.

Accidental Rejection Efficiency

If the peaks used for accidental rejection (Fig. 3.8) change their position or width, cut efficiency becomes different between beam OFF and ON. The cut condition was taken loose (from -5σ to 3σ) to reduce this effect. This effect was estimated using data before requiring the back-to-back 511 keV energy cut because the real signal is enhanced with this energy cut and causes the under-estimation of the cut efficiency of beam ON events. It turned out that its contribution is at most $^{+0.68\%}_{-0.22\%}$,

and negligible in calculating Ps-HFS at the current level of precision. Table D.1 summarizes the results of this estimation.

Background Normalization

The remaining background was estimated with beam OFF events. The beam OFF and ON spectra were normalized with the number of events at the prompt peak (from -4.0 ns to 3.0 ns) of time spectra. The prompt peak contains normal positron annihilations, p-Ps events, and slow positron events. These events are statistically independent of ones in time window (from 50 ns to 250 ns). A statistical error of the number of events in the prompt peak becomes a systematic uncertainty. Even in the RUN with the least statistics, the uncertainty due to normalization was only 0.17%. This is negligible in calculating Ps-HFS at the current level of precision. Table D.2 summarizes this uncertainty.

3.5.5 Summary of the Systematic Errors

Table 3.8 summarizes systematic uncertainties for each RUN. Effects of the power estimation uncertainty was estimated by scanning C of each frequency with an asymmetric Gaussian function when we fit the data with MC. The Stark effect (-460 ppm shift for Ps-HFS) is a common systematic error and was considered at last. Other errors were combined with statistical uncertainty of S/N of data and MC. Another uncertainty for each RUN has negligible effect when obtaining Ps-HFS and p-Ps lifetime.

RUN ID	Power Estimation	MC	Accidental Rejection	Normalization
A-1	$+14.7$ / -17.2%	6.67%	0.10%	0.07%
A-2	$+14.7$ / -17.2%	2.34%	-0.10%	0.07%
B-1	$+19.2$ / -20.9%	12.79%	negligible	0.06%
C-1	$+12.7$ / -14.7%	8.35%	-0.23%	0.08%
C-2	$+12.7$ / -14.7%	15.78%	-0.04 %	0.08%
C-3	$+12.7$ / -14.7%	7.42%	-0.07 %	0.07%
D-1	$+12.7$ / -14.7%	3.40%	-0.02%	0.12%
D-2	$+12.7$ / -14.7%	4.89%	0.68%	0.17%
D-3	$+12.7$ / -14.7%	17.25%	-0.02%	0.16%
D-4	$+12.7$ / -14.7%	12.40%	-0.20%	0.15%
D-5	$+12.7$ / -14.7%	0.88%	-0.11%	0.16%
E-1	$+20.4$ / -22.1%	0.25%	0.06%	0.08%
E-2	$+20.4$ / -22.1%	7.72%	0.22%	0.09%
F-1	$+12.3$ / -14.0%	4.82%	0.22%	0.06%
F-2	$+12.3$ / -14.0%	4.79%	0.09%	0.07%
G-0	$+24.0$ / -29.0%	6.29%	0.13%	0.06%

Table 3.8: Summary of systematic uncertainties.

3.6 Result

We obtained the following results from the analysis described in this chapter. Ps-HFS and the Einstein's A coefficient are

$$\Delta_{\mathrm{Ps}}^{\mathrm{HFS}} = 203.39^{+0.15}_{-0.14}\,(\mathrm{stat.}) \pm 0.11\,(\mathrm{syst.})\,\mathrm{GHz} \tag{3.20}$$

$$A = 3.69 \pm 0.48\,(\mathrm{stat.}) \pm 0.29\,(\mathrm{syst.}) \times 10^{-8}\,\mathrm{s}^{-1}. \tag{3.21}$$

This result contains the Stark shift correction. This is the first direct measurement of Ps-HFS. An asymmetric errors mean the correlations among three fitting variables. These two results are consistent with the QED predictions of $\mathcal{O}(\alpha^3 \log \alpha^{-1})$ for Ps-HFS and the tree level calculation for A, within 1 standard deviation

$$\Delta_{\mathrm{HFS}}^{\mathrm{Ps}}(\mathrm{th}) = 203.391\ 69(41)\,\mathrm{GHz}\ [35][36][37] \tag{3.22}$$

$$A(\mathrm{th}) = 3.37 \times 10^{-8}\,\mathrm{s}^{-1}\ [15] \tag{3.23}$$

Lifetime of p-Ps ($\tau_{\mathrm{p\text{–}Ps}}$) is

$$\tau_{\mathrm{p\text{–}Ps}} = 89^{+18}_{-15}\,(\mathrm{stat.}) \pm 10\,(\mathrm{syst.})\,\mathrm{ps} \tag{3.24}$$

This is the first direct measurement of p-Ps lifetime. This result is consistent with the QED prediction of $\mathcal{O}(\alpha^3 \log \alpha^{-1})$ within 1.7 standard deviations

$$\tau_{\mathrm{p\text{–}Ps}}(\mathrm{th}) = 125.164\ 7(2)\,\mathrm{ps}\ [63][64] \tag{3.25}$$

A summary of uncertainties is shown in Table 3.9

	Ps-HFS	p-Ps life	A coefficient
Counting statistics	+740 ppm	+20 %	+13 %
	−690 ppm	−17 %	−13 %
Power estimation uncertainty	430 ppm	10%	7.2%
Stark effect	460 ppm	negligible	negligible
Monte Carlo simulation	280 ppm	5.5%	3.0%
Quadrature sum	+1010 ppm	+23%	+15%
	−980 ppm	−20%	−15%

Table 3.9: Uncertainties in this measurement.

Chapter 4

Discussion

4.1 Consistency Check of Power Estimation

The most problematic systematic error is the uncertainty of power estimation unestablished in the millimeter-wave range. This uncertainty should be checked with a totally independent method from one described in Sec. 2.2.3. In this research, we discovered an unexpected increase of Ps formation probability in gas containing nitrogen molecules (This trouble was solved by using neopentane gas as described in Sec.2.3.2). Therefore, we can estimate accumulated power in the Fabry-Pérot resonant cavity with this increase.

The increase of Ps is statistically limited because of the small detection efficiency of 3γ from the cavity region. Instead, a ratio of the slow positron decrease $f(V_{\rm tr})$ was studied in pure 1 atm nitrogen. Figure 4.1 shows results, in which required cut conditions are the same as that described in Chap. 3. It is difficult to properly fit the data with a toy model shown in Fig. 2.33 because this model ignores inelastic scattering. A few data points cannot constrain complex models with many unknown parameters. Therefore, a simple empirical formula is introduced

$$f(V_{\rm tr}) = \sqrt{C_{\rm rel} V_{\rm tr}} \tag{4.1}$$

The coefficient $C_{\rm rel}$ can be used to estimate power calibration constant C as summarized in Table 4.1. We estimated new C (denoted as C') by fixing $C' = C$ at 201.8 GHz and relatively calculated other C' by $C_{\rm rel}$ ratio. The results are all consistent with the absolute power calibration constant C.

Signal contamination of the Ps-HFS transition is a systematic error for this relative power estimation. One can estimate upper limit of signal contamination using the neopentane data in which no slow positrons exist in time window. In RUN A-1 (off-resonance), the rate of beam OFF events (background) is 499 mHz, and the transition rate is 21 mHz at 21.6 kW. Slow positron data at a similar condition (203.81 GHz, 24.3 kW) has the background rate of 1.82 Hz, and the slow positron decrease rate of 298 mHz. Thus, the signal contamination was estimated at most 10% at off-resonance. In RUN C-2 (on-resonance), the background rate is

453 mHz, and the transition rate is 93 mHz at 67.4 kW. Slow positron data at a similar condition (203.56 GHz, 56.2 kW) has the background rate of 1.66 Hz, and the slow positron decrease rate of 422 mHz. Therefore, the signal contamination was estimated at most 20% at on-resonance. These are less than the errors which have been already assigned to the relative power calibration.

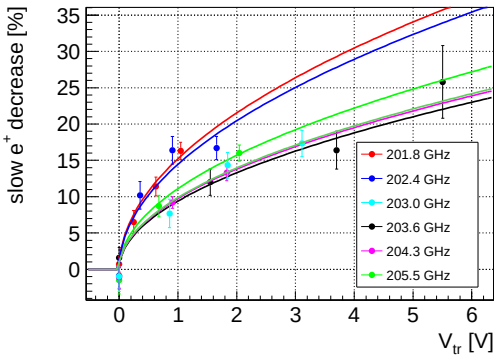

Figure 4.1: Relative power estimation with the slow positron decrease.

Frequency	C_{rel}	C' [kW/V]	C [kW/V]
201.83 GHz	232(28)	23.2 (fixed)	$23.2^{+3.4}_{-4.0}$
202.64 GHz	209(29)	20.9(3.8)	$23.4^{+4.5}_{-4.9}$
203.00 GHz	97(15)	9.7(1.9)	$14.6^{+2.2}_{-2.3}$
203.51 GHz	88(17)	8.8(2.0)	$10.2^{+1.3}_{-1.5}$
204.56 GHz	95(11)	9.5(1.6)	$11.3^{+2.3}_{-2.5}$
205.31 GHz	123(16)	12.3(2.2)	$11.4^{+1.4}_{-1.6}$

Table 4.1: Relative power calibration constant.

4.2 Cut Validation

The result should be independent of the event selection within statistical uncertainties. We slightly changed cut conditions to validate it. Only statistical uncertainties (no Stark effect correction) were considered in the following sections.

4.2.1 Time Window

We required the time window from 50 ns to 250 ns. Table 4.2 summarizes when the upper bound which determines remaining accidental events of this condition is

varied. Integral of fitted time spectra should return a consistent result compared with cut-based values, and is listed in the same table. All results are consistent with each other.

upper bound [ns]	A coefficient [$\times 10^8 s^{-1}$]	Ps-HFS [GHz]	p-Ps life [ps]
200	3.64±0.47	203.29±0.12	97.2±17.3
250	3.65±0.47	203.30±0.14	89.3±15.1
300	3.58±0.47	203.36±0.15	85.6±15.1
350	3.62±0.48	203.43±0.16	77.9±15.2
400	3.79±0.49	203.44±0.15	84.0±15.0
fitting	3.68±0.45	203.33±0.13	86.0±13.9

Table 4.2: Check of time window.

4.2.2 Accidental Rejection

We required accidental rejection condition from -5σ to 3σ to obtain the result. Table 4.3 summarizes when the upper bound which determines remaining accidental events is varied. All results are consistent with each other.

upper bound	A coefficient [$\times 10^8 s^{-1}$]	Ps-HFS [GHz]	p-Ps life [ps]
2σ	3.43±0.49	203.35±0.15	102.5±21.3
3σ	3.65±0.47	203.30±0.14	89.3±15.1
4σ	3.89±0.45	203.37±0.13	85.9±13.0

Table 4.3: Check of the accidental rejection cut.

4.2.3 Energy Cut

We required energy cut condition from -2σ to 3σ to obtain the result. Table 4.4 summarizes when the lower bound which determines 3γ-ray contamination is varied. All results are consistent with each other.

lower bound	A coefficient [$\times 10^8 s^{-1}$]	Ps-HFS [GHz]	p-Ps life [ps]
$3\ \sigma$	3.46±0.49	203.33±0.19	91.3±17.1
2.5σ	3.59±0.48	203.36±0.15	88.9±15.4
$2\ \sigma$	3.65±0.47	203.30±0.14	89.3±15.1

Table 4.4: Check of the energy cut.

4.3 Future Prospects

The Ps-HFS value was directly measured for the first time in this research. The next target is to reach a sufficient level of precision to address the observed discrepancy (15 ppm). Figure 4.2 shows a possible future setup. Three major improvements are required: i) A estimation with a 100 kW-class gyrotron, ii) Ps formation in vacuum, iii) A frequency tunable gyrotron. These three points are all technical challenges for each field, and are described from the next section.

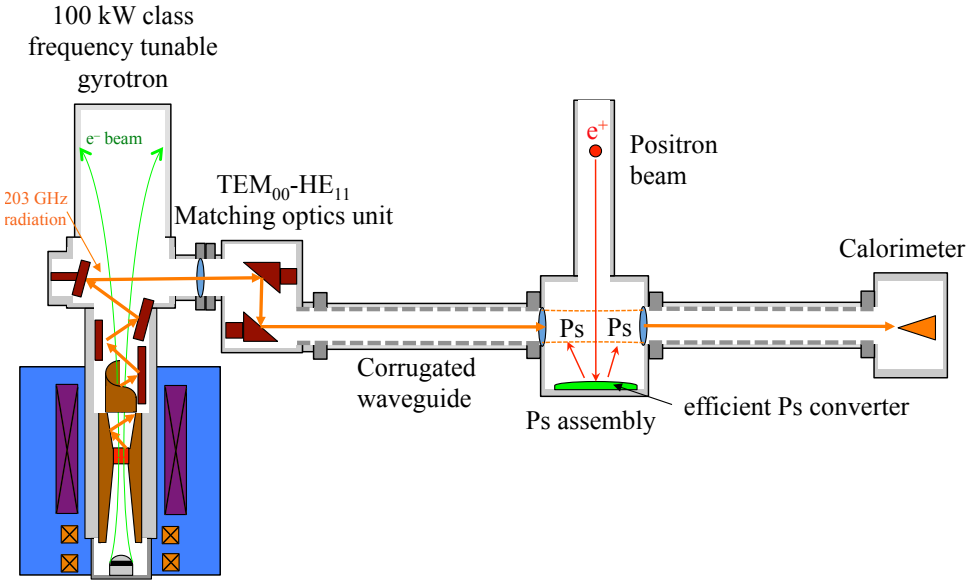

Figure 4.2: Schematic view of a possible future setup.

4.3.1 Power Estimation with 100 kW-Class Gyrotron

According to Table 3.9, one of the dominant errors is from the power estimation uncertainty. We need relative accuracy of better than 0.3% for the power estimation (currently, 10-20%). There are two problems at different levels. One problem is absence of established power standards in the high-power millimeter-wave range. The other problem is the power uncertainty caused by use of the Fabry-Pérot resonant cavity. The only reliable method is to measure REAL power with water temperature under well-controlled interference conditions.

The most realistic solution with current technology is to develop a 100 kW-level gyrotron and abandon the Fabry-Pérot cavity. Real power is always dumped into a calorimeter, in which steady state between water flow and power absorption is achieved as shown in the right hand side of Fig. 4.2. We need essential changes of the power supply, the MIG, the electron beam collector, water cooling systems,the Gaussian converter, and the output window. We should also develop an over-sized

corrugated waveguide system to safely handle really high-power millimeter-wave radiation. It is necessary to correct a phase from TEM_{00} mode (Gaussian beam) to HE_{11} mode (an eigenmode of the corrugated waveguide) with a matching optics unit [65]. Such kind of system is very costly but already be in practice for fusion applications. They are shown in the left hand side of Fig. 4.2.

4.3.2 Ps Formation in Vacuum

Statistics should be improved by over four orders of magnitude. Positrons, without static magnetic fields, are scattered randomly by gas molecules as shown in Fig. 3.11. Small amounts of Ps are formed in a high-power radiation region and contribute to the transition signal. Others are in an exterior region and result in background (pick-off annihilation in gas and o-Ps decay). One requires either focusing Ps in the beam region or eliminating background annihilations. This is impossible with a commercial positron source and gas used in this thesis.

One has some difficulties in use of gas as an electron source. We cannot use gas with really high-power gyrotrons because of discharge problems. Systematic uncertainties (Ps formation increase, Stark effect and non-thermalized Ps discussed in Sec. 1.5.3) from gas should be also eliminated. Any problems due to gas handling are undesirable in precise spectroscopy measurements.

Ps should be formed in vacuum with an intense positron beam. The pick-off background does not exist in vacuum. Three γ-ray contamination from o-Ps decay can be reduced by broadening high-power beam region and collimate the Ps formation region. Ps collimation is also needed to eliminate annihilation at a wall.

There are some intensive studies to produce high Ps yield in vacuum [66][67]. An intense positron beam is produced with tungsten foils irradiated by an electron beam [68]. A positron beam is introduced to a Ps assembly between the corrugated waveguides as shown in middle of Fig. 4.2. An efficient Ps converter which emits Ps into vacuum is required. Some materials with porous structure are candidates for the Ps converter. Another option is use of a Ps beam instead of the positron beam [69]. An well-controlled Ps beam can be easily collimated at the beam region.

4.3.3 Frequency Tunable Gyrotron

In this thesis, oscillation frequency of the gyrotron is changed by replacing the RF cavity. Even though we treated the MIG with the greatest care to protect it from air contamination, replacement of the RF cavity inevitably determines ultimate lifetime of the MIG (less than one year). Irreproducibility of alignment (better than 0.5 mm is required for a few meter size object as described in Appendix A.6) is also problematic for a precision measurement. Gyrotron output frequency should be continuously changed without open a vacuum case.

Theoretically, frequency-tunability can be obtained in use of backward-wave oscillation. In a normal gyrotron operation, the electron beam couples to an axial fundamental mode TE_{mn1} (See Fig A.3 and Table A.1). Other axial modes TE_{mn2},

TE_{mn3}, $\cdots$ have slightly different resonant frequency, but are not excited because of high phase velocity and low Q-factor. Backward-wave oscillation makes use of the Doppler shift of gyrating electrons to continuously connect higher axial modes. Figure 4.3 shows operation conditions of gyro-devices. A dispersion relation of the electron beam including the Doppler shift shown as a solid line in this figure is expressed as

$$\omega = \omega_c + k_z v_{//}, \tag{4.2}$$

where k_z denotes wave number of electrons parallel to the magnetic field, and $v_{//}$ does parallel velocity. A hyperbola represents approximate dispersion relation of the RF cavity (See Appendix A.2 for detail) expressed as

$$\omega_r = c\sqrt{k_z^2 + \left(\frac{j'_{mn}}{R}\right)^2}, \tag{4.3}$$

where R denotes radius of the RF cavity. Oscillation of gyro-devices occurs near the cross points between above two curves. Gyrotron oscillation means $k_z \sim 0$, and is monochromatic. Interaction with backward waves at $k_z < 0$ has a potential to continuously tune output frequency. Such devices are called gyro-BWO.

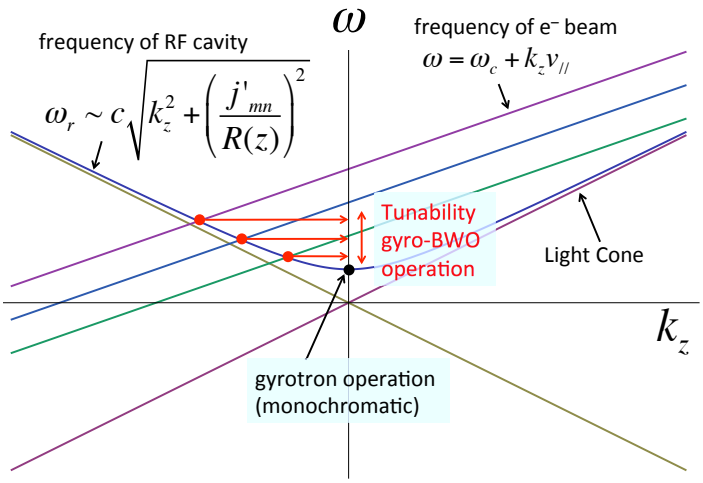

Figure 4.3: Schematic diagram of dispersion relation of electrons and RF cavity.

Many gyro-BWO devices have been tested in independent institutes [70]. Unfortunately, obtained output power is very low (much less than 100 W). High Q-factor for higher axial modes causes inefficient power extraction, and needs complicated internal mode converters. A new idea to get high-power extraction is a reflective gyro-BWO with a tapering RF cavity. The next step in gyrotron development is to test this new device and make it in practical use.

Chapter 5

Conclusion

Ps-HFS was firstly measured with a direct transition method. Measurement of the Ps-HFS is difficult because the Ps-HFS transition is suppressed with finite lifetime of Ps, and Ps-HFS is in the millimeter-wave region. It requires development of a high-power millimeter-wave system, which is a big challenge for current technology of plasma physics and millimeter-wave optics.

A gyrotron oscillator was developed as a high-power (> 100 W) millimeter-wave radiation source. It was a technical challenge to fabricate and control the gyrotron with such high frequency (203 GHz). We changed output frequency of the gyrotron by replacing an internal RF cavity. A long time (more than a week) operations were the first trial with the high-power gyrotron.

A Fabry-Pérot resonant cavity accumulates radiation to equivalent power of about 20 kW to cause the induced transition from o-Ps to p-Ps. In the millimeter-wave range, a great effort was required to design a half mirror with high reflectivity, low loss, and withstanding against high-power dumping. A gold mesh mirror on a silicon substrate was developed.

There are no established methods to measure high-power millimeter-wave radiation today. Accumulated power is, especially, difficult to estimate because cavity finesse (Q-factor) and coupling cannot be measured with rather wide line-width of gyrotron output. This thesis reported a new way to directly measure the accumulated power. We calibrated output of the pyroelectric detector with temperature increase of a water load. We corrected reflected-beam effects which reduced the oscillation efficiency of the gyrotron.

Output power from the gyrotron was stabilized with a feed-back control of the electron-beam current. Accumulated power wan the Fabry-Pérot cavity is also stabilized by controlling length of the cavity. There are inevitable fluctuations in this accumulated power in one pulse because of line-width and drift of the gyrotron frequency. We corrected this effect with a Monte Carlo simulation in analysis.

A Ps formation assembly and γ-ray detectors were carefully arranged to enhance S/N of the direct transition. Use of neopentane gas was a key to reduce an increase of Ps formation probability due to positron acceleration by millimeter-

wave radiation. $LaBr_3(Ce)$ scintillators are used to detect γ rays with high energy resolution.

The reaction cross-section of the Ps-HFS transition is studied using MC, and obtained Ps-HFS value $\Delta_{\rm Ps}^{\rm HFS}$, lifetime of p-Ps $\tau_{\rm p\text{–}Ps}$, and the Einstein A coefficient are

$$\Delta_{\rm Ps}^{\rm HFS} = 203.39^{+0.15}_{-0.14}\,(\text{stat.}) \pm 0.11\,(\text{syst.})\,\text{GHz} \tag{5.1}$$

$$\tau_{\rm p\text{–}Ps} = 89^{+18}_{-15}\,(\text{stat.}) \pm 10\,(\text{syst.})\,\text{ps} \tag{5.2}$$

$$A = 3.69 \pm 0.48\,(\text{stat.}) \pm 0.29\,(\text{syst.}) \times 10^{-8}\,\text{s}^{-1}. \tag{5.3}$$

This is the first direct measurement of Ps-HFS and lifetime of p-Ps. These are consistent with the QED calculations.

Precise but indirect measurements of Ps-HFS were performed in 1970's and 1980's. Recent QED calculations of Ps-HFS differ from the measured value by 3.04(79) MHz (15 ppm), which is unlikely to be due to a statistical fluctuation (3.9 standard deviations). A candidate in the future to test this discrepancy is the direct measurement of Ps-HFS firstly performed in this thesis. Some technical improvements are needed to reach a sufficient level of precision to address the observed discrepancy. This thesis pointed out development of a frequency tunable gyrotron of 100 kW and a method of efficient Ps production in vacuum with a positron beam.

Acknowledgements

This experiment is a collaboration of the University of Tokyo and Fukui University. I would like to thank my collaborators and Ph.D. advisers.

I would like to express my gratitude to my supervisor Prof. Shoji Asai who supported me during past six years. My researcher life suddenly started just two days after I firstly met him. This earlier start resulted in publication of the first paper when I was in the master course. The themes he introduced to me were always very unique. Especially, the experiment reported in this thesis was quite challenging and worthwhile.

I wish to express my gratitude to collaborators in Research Center for Development of Far-Infrared Region, University of Fukui (FIR-FU). Prof. Takatoshi Idehara always encouraged me, and sometimes literally helped me with a screw wrench to adjust the gyrotron. He also gave me many chances to present my study in the international arena. I would like to thank Prof. Yoshinori Tatematsu for developing the new gyrotron oscillator with the internal Gaussian mode converter. It was a great turning point to bring this experiment to a successful conclusion. Prof. Isamu Ogawa was so kind to give me practical advices to operate the gyrotron and measure output frequency. I would like to give my special thanks to Mr. Tomohiro Kanemaki and members in the factory for fabrication of the gyrotron.

I also wish to express my great appreciation to collaborators in the University of Tokyo. Prof. Tomio Kobayashi never complained about this experiment and always encouraged me. Useful discussions with Prof. Haruo Saito pushed on this experiment at the earlier stage when I did not know anything about positronium and its transition. Dr. Toshio Namba looked at me with hard eyes to carry out this experiment in realistic time and cost required. Dr. Taikan Suehara is a pioneer of this experiment. He is always very positive even when we reached a deadlock (it happened every one month in this challenging experiment). He taught never-say-die mind to me. Dr. Takayuki Yamazaki was a great and smart collaborator. He always finished his work before I asked him something. I usually come up with many miscellaneous ideas and sink into a bog. He is mature experimentalist and gives me many useful suggestions. I wish to express my appreciation to Mr. Shigemi Otsuka and members in the factory. Finally, I would like to thank Mr. Akira Ishida and all staffs in department of Physics, and International Center for Elementary Particle Physics for their frequent help.

Bibliography

[1] G. Bennet et al., Phys. Rev. D **73**, 072003 (2006).

[2] R. Pohl et al., Nature **466**, 213 (2010).

[3] R.J. Hill and G. Paz, Phys. Rev. Lett. **107**, 160402 (2011).

[4] T. Namba, Prog. Theor. Exp. Phys. (04D003) (2012).

[5] D. Hagena, R. Ley, D. Weil, G. Werth, W. Arnold, and H. Schneider, Phys. Rev. Lett. **71**, 2887 (1993).

[6] R. Ley, D. Hagena, D. Weil, G. Werth, W. Arnold, and H. Schneider, Hyperfine Interact **89**, 327 (1994).

[7] M.S. Fee, A.P. Mills Jr., S. Chu, E.D. Shaw, K. Danzmann, R.J. Chichester, and D.M. Zuckerman, Phys. Rev. Lett. **70**, 1397 (1993).

[8] M.S. Fee, A.P. Mills Jr., S. Chu, E.D. Shaw, K. Danzmann, R.J. Chichester, and D.M. Zuckerman, Phys. Rev. A. **48**, 192 (1993).

[9] A.H. Al-Ramadhan and D.W. Gidley, Phys. Rev. Lett. **72**, 1632 (1994).

[10] Y. Kataoka, S. Asai, and T. Kobayashi, Phys. Lett. B **671**, 219 (2009).

[11] C. Itzykson and J.B. Zuber, *Quantum Field Theory*, Dover, 2005.

[12] N. Ramsey, Rev. Mod. Phys. **62**, 541 (1990).

[13] A.P. Mills, Jr., Phys. Rev. A **27**, 262 (1983).

[14] L. Mower, Phys. Rev. **142**, 799 (1966).

[15] P. Wallyn, W.A. Mahoney, Ph. Durouchoux, and C. Chapuis, Astrophysical J. **465**, 473 (1996).

[16] R. Loudon, *The Quantum Theory of Light second edition*, Oxford University Press, 1983.

[17] C.J. Foot, *Atomic Physics*, Oxford University Press, 2005.

[18] C. Bischoff, et all, Astrophysical J. **768**, 9 (2013).

[19] A. Wooten and A.R. Thompson, Proc. IEEE **97**, 1463 (2009).

[20] R. Shimano, G. Yumoto, J.Y. Yoo, R. Matsunaga, S. Tanabe, H. Hibino, T. Morimoto, and H. Aoki, Nature Commun. **4**, 1841 (2013).

[21] K. Sakamoto et al., Nucl. Fusion **49**, 095019 (2009).

[22] S.T. Han et al., IEEE Trans. Plasma Sci. IEEE Nucl. Plasma Sci. Soc. **35**, 559 (2007).

[23] A. Yariv and P. Yeh, *Photonics sixth edition*, Oxford University Press, 2005.

[24] M. Deutsch and S.C. Brown, Phys. Rev. **85**, 1047 (1952).

[25] R. Weinstein, M. Deutsch, and S. Brown, Phys. Rev. **94**, 758(H9) (1954).

[26] R. Weinstein, M. Deutsch, and S. Brown, Phys. Rev. **98**, 223(A8) (1955).

[27] V.W. Hughes, S. Marder, and C.S. Wu, Phys. Rev. **106**, 934 (1957).

[28] E.D. Theriot, Jr., R.H. Beers, V.W. Hughes, and K.O H. Ziock, Phys. Rev. A **2**, 707 (1970).

[29] E.R. Carlson, V. W.Hughes, M.L. Lewis, and I. Lindgren, Phys. Rev. Lett. **29**, 1059 (1972).

[30] A.P. Mills, Jr. and G.H. Bearman, Phys. Rev. Lett. **34**, 246 (1975).

[31] E.R. Carlson, V.W. Hughes, and I. Lindgren, Phys. Rev. A **15**, 241 (1977).

[32] P.O. Egan, V.W. Hughes, and M.H. Yam, Phys. Rev. A **15**, 251 (1977).

[33] M.W. Ritter, P.O. Egan, V.W. Hughes, and K.A. Woodle, Phys. Rev. A **30**, 1331 (1984).

[34] R. Karplus and A. Klein, Phys. Rev **87**, 848 (1952).

[35] B.A. Kniehl and A.A. Penin, Phys. Rev. Lett. **85**, 5094 (2000).

[36] K. Melnikov and A. Yelkhovsky, Phys. Rev. Lett. **86**, 1498 (2001).

[37] R.J. Hill, Phys. Rev. Lett. **86**, 3280 (2001).

[38] A. Ishida, T. Namba, S. Asai, T. Kobayashi, H. Saito, M. Yoshida, K. Tanaka, and A. Yamamoto, arXiv:1310.6923 .

[39] V.G. Baryshevsky, O.N. Metelitsa, and V.V. Tikhomirov, J. Phys. B: At. Mol. Opt. Phys. **22**, 2835 (1989).

[40] V.G. Baryshevsky, O.N. Metelitsa, V.V. Tikhomirov, S.K. Andrukhovich, A.V. Berestov, B.A. Martsinkevich, and E.A. Rudak, Phys. Lett. A **136**, 428 (1989).

[41] S. Fan, C.D. Beling, and S. Fung, Phys. Lett. A **216**, 129 (1996).

[42] Y. Sasaki, A. Miyazaki, A. Ishida, T. Namba, S. Asai, T. Kobayashi, H. Saito, K. Tanaka, and A. Yamamoto, Phys. Lett. B **697**, 121 (2011).

[43] D.B. Cassidy, T.H. Hisakado, H.W.K. Tom, and A.P. Mills, Jr., Phys. Rev. Lett. **109**(073401) (2012).

[44] A. Ishida, Y. Sasaki, G. Akimoto, T. Suehara, T. Namba, S. Asai, T. Kobayashi, H. Saito, M. Yoshida, K. Tanaka, and A. Yamamoto, Hyperfine Interactions **212**, 133 (2012).

[45] M.V. Kartikeyan, E. Borie, and M.K.A. Thumm, *Gyrotrons*, Springer, 2003.

[46] G.S. Nusinovich, *Introduction to the Physics of Gyrotrons*, The Johns Hopkins UIniversity Press, 2004.

[47] C.J. Edgcombe, *Gyrotron Oscillators*, Taylor and Francis, 1993.

[48] Y. Tatematsu et al., J. Infrared Milli. Terahz Waves **33**, 292 (2012).

[49] G. Dammertz et al., IEEE Trans. Plasma Sci. **27**, 330 (1999).

[50] T.M. Antonsen, S.Y. Cai, and G.S. Nusinovich, Phys. Fluids B **4**, 4131 (1992).

[51] M.Yu. Glyavin, V.E. Zapevalov, A.N. Kuftin, and A.G. Luchinin, Radiophys. Quantum Elec. **43**, 4 (2000).

[52] K.E. Kreischer, B.G. Danly, P. Woskoboinikow, W.J. Mulligan, and R.J. Temkin, Frequency Pulling and Bandwidth Measurements of a 140 GHz Pulsed Gyrotron, Technical report, Plasma Fusion Center, MIT, Cambridge, 1984, PFC/JA-84-24.

[53] C. C. S. T. AG, CST MW Studio 2011, http://www.cst.com.

[54] T. Yamazaki, A. Miyazaki, T. Suehara, T. Namba, S. Asai, T. Kobayashi, H. Saito, I. Ogawa, T. Idehara, and S. Sabchevski, Phys. Rev. Lett. **108**, 253401 (2012).

[55] K. Iwata, R.G. Greaves, T.J. Murphy, M.D. Tinkle, and C.M. Surko, Phys. Rev. A **51**, 473 (1995).

[56] K. Iwata, R.G. Greaves, and C.M. Surko, Phys. Rev. A **55**, 3586 (1997).

[57] P.W. Atkins, *Physical Chemistry sixth edition*, Oxford University Press, 1998.

[58] D.R. Lide, Jr., and D.E. Mann, J. Chem. Phys. **29**, 4 (1958).

[59] D.R. Lide, Jr., J. Chem. Phys. **33**, 5 (1960).

[60] S. Marder, V.W. Hughes, C.S. Wu, and W. Bennett, Phys. Rev. **103**, 1258 (1956).

[61] W.B. Teutch and V.W. Hughes, Phys. Rev. **103**, 1266 (1956).

[62] M. Skalsey, J.J. Engbrecht, C.M. Nakamura, R.S. Valley, and D.W. Gidley, Phys. Rev. A. **67**, 022504 (2003).

[63] B.A. Kniehl and A.A. Penin, Phys. Rev. Lett. **85**, 1210 (2000).

[64] K. Melnikov and A. Yelkhovsky, Phys. Rev. D **62**, 116003 (2000).

[65] J. Jin, G. Gantenbein, S. Kern, T. Rzesnicki, and M. Thumm, Vac. Elec. Conf. IEEE int. , 271 (2011).

[66] S. Mariazzi, P. Bettotti, S. Larcheri, T. Toniutti, and R.S. Brusa, Phys. Rev. B **81**, 235418 (2010).

[67] F. Moia, R. Ferragut, A. Dupasquier, M.G. Giammarchi, and G.Q. Ding, Eur. Phys. J. D **66**, 124 (2012).

[68] K. Wada et al., Eur. Phys. J. D **66**, 37 (2012).

[69] K. Michishio, T. Tachibana, R.H. Suzuki, K. Wada, A. Yagishita, T. Hyodo, and Y. Nagashima, App. Phys. Lett. **100**, 254102 (2012).

[70] T.H. Chang, T. Idehara, I. Ogawa, L. Agusu, and S. Kobayashi, J. Appl. Phys. **105**, 063304 (2009).

[71] O. Dumbrajs, T. Idehara, T. Saito, and Y. Tatematsu, Jpn. J. Appl. Phys. **51**, 126601 (2012).

[72] B.G. Danly and R.J. Temkin, Phys. Fluids **29**, 561 (1986).

[73] C. C. S. T. AG, CST Particle Studio 2011, http://www.cst.com.

[74] F.F. Chen, *Introduction to Plasma Physics*, Plenum Press, New York, 1974.

[75] O. Dumbrajs, Int. J. Infrared Milli. Waves **15**, 1255 (1994).

Appendix A

Gyrotron Theory

A.1 Calculation Procedure

Gyrotron physics is one of the most interesting topics in plasma physics. It is not practical to quantum-mechanically consider the maser oscillation between Landau levels. Instead, classical consideration using Maxwell's equations and the Lorentz force is usually taken [71][72]. Firstly, we introduce electromagnetic fields in the RF cavity absence of an electron beam. Electron-beam handling is discussed next. Then, interaction between millimeter waves and the electron beam is calculated. This formalism is called a *Cold Cavity* method in which perturbation from electrons to a field profile of radiation is ignored. Another formalism is called a *Self Consistent* method in which electron motion and RF behavior are simultaneously solved. Cold cavity formalism is a good approximation when quality factor of the RF cavity is high enough.

A.2 Theory of the RF Cavity

The RF cavity is an open-ended cylindrical resonator whose resonance angular frequency is ω_{r}. It can be considered as an irregular waveguide, of which radius R varies slowly along the z-axis as shown in Fig A.1. Electrons from the MIG are introduced from the left hand side of this figure, where the resonator is cutoff preventing RF fields from leaking and damaging the MIG. The intermediate region is a flat waveguide of radius R_2 and length L_2. The right side is an output section and open.

The resonant mode of the RF cavity is a solution of Maxwell's equations in a cavity wall. Let us take cylindrical coordinates (r, ϕ, z). Only Transverse Electric (TE) modes are considered because gyrating electrons are coupled with transverse electric fields, not with magnetic fields. Introducing an azimuthal index $\mathrm{m} = 0, \pm1, \pm2, \pm3, \cdots$, a radial index $\mathrm{n} = 1, 2, 3, \cdots$, and an axial index $\mathrm{l} = 1, 2, 3, \cdots$, the eigenmodes of this cavity ($\mathrm{TE}_{\mathrm{mnl}}$ resonant modes) are products of a transverse vector function $\overrightarrow{E}(r, \phi)$ and an axial scalar function $\Psi(z)$. One can approximate the

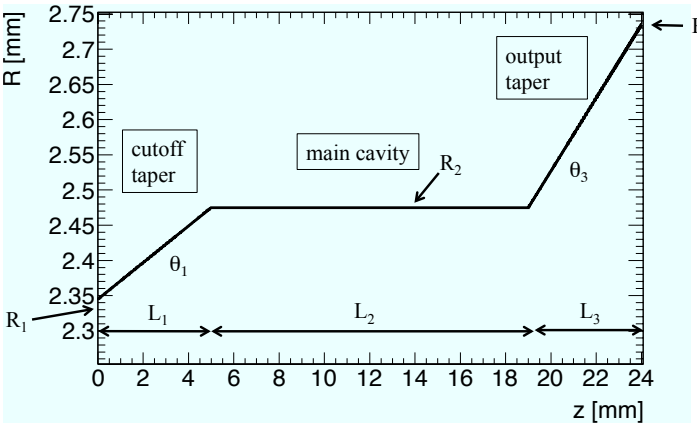

Figure A.1: Cross-sectional geometry of the RF cavity used in FU CW G1.

transverse electric field $\overrightarrow{E}(r,\phi)$ by propagating $\mathrm{TE_{mn}}$ modes in a circular waveguide expressed as

$$E_{\mathrm{r}}(r,\phi) = E_0 m \frac{R}{r} J_{\mathrm{m}}\left(\frac{j'_{\mathrm{mn}}}{R} r\right) \sin(m\phi), \tag{A.1}$$

$$E_{\phi}(r,\phi) = E_0 J'_{\mathrm{m}}\left(\frac{j'_{\mathrm{mn}}}{R} r\right) \cos(m\phi), \tag{A.2}$$

$$E_{\mathrm{z}}(r,\phi) = 0, \tag{A.3}$$

where E_0 is normalized strength of the electric field, $J_{\mathrm{m}}(x)$ is the m-th Bessel function of the 1^{st} kind, $J'_{\mathrm{m}}(x)$ is its 1^{st} derivative, and j'_{mn} is the n-th root of $J'_{\mathrm{m}}(x) = 0$. Since taper angles of the cavity are small, changes of $R(z)$ can be ignored, and the mode mixing with another $\mathrm{TE_{m'n'}}$ is also negligible. Figure A.2 shows $\overrightarrow{E}(r,\phi)$ of the $\mathrm{TE_{52}}$ used in this experiment. Note that there are two degenerated states according to sign of the azimuthal index m except for $m = 0$ case, which corresponds to phase rotation around the z-axis. When gyrating electrons exist, this degeneracy is removed to co-rotating or counter-rotating with electron cyclotron motion in a magnetic field.

An axial function $\Psi(z)$ obeys a nonuniform string equation

$$\frac{d^2\Psi(z)}{dz^2} + \zeta_{\mathrm{mn}}^2(z)\Psi(z) = 0, \tag{A.4}$$

$$\zeta_{\mathrm{mn}}(z) = \sqrt{\left(\frac{\omega}{c}\right)^2 - \left(\frac{j'_{\mathrm{mn}}}{R(z)}\right)^2}, \tag{A.5}$$

where $\omega = \omega_{\mathrm{r}}\left(1 + \frac{i}{2Q_{\mathrm{D}}}\right)$ is complex RF frequency, and Q_{D} is a diffraction quality factor. An open-end correction is calculated at cutoff and output sections to estimate ω_{r} and Q_{D} simultaneously. Equation (A.4) is solved numerically under the

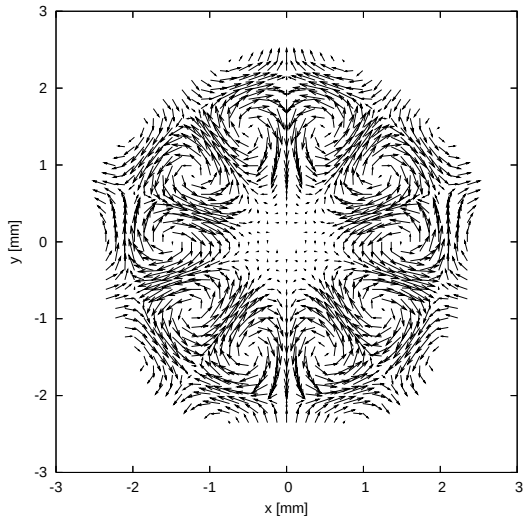

Figure A.2: Transverse structure of the electric field in the RF cavity (TE_{52} mode).

following boundary conditions:

$$\frac{d\Psi}{dz}(0) = i\zeta_{\rm mn}\Psi \tag{A.6}$$

$$\frac{d\Psi}{dz}(z_{\rm out}) = -i\zeta_{\rm mn}\Psi, \tag{A.7}$$

where $z_{\rm out}$ is an end-point of the output taper ($z_{\rm out} = L_1 + L_2 + L_3$). One solves Eq. (A.4) with Eq. (A.6) as an initial condition, for example using the Runge-Kutta formula. Then, two variables ($\omega_{\rm r}$, $Q_{\rm D}$) are varied until the second boundary condition Eq. (A.7) is satisfied. Figure A.3 shows the result of this calculation for the RF cavity in this experiment. Three different lines correspond to different axial indices ($l = 1, 2, 3$). The solution is listed in Table A.1. A quality factor due to Ohmic loss Q_Ω and combined Q are also shown. The Ohmic quality factor is given by

$$Q_\Omega = \frac{R_2}{\delta}\left[1 - \left(\frac{m}{j'_{\rm mn}}\right)\right], \tag{A.8}$$

where $\delta = 0.18\,\mu$m is the skin depth of copper at 200 GHz. In a normal operation of the gyrotron (gyromonotron), TE_{521} (shown as a solid line in Fig. A.3) mode is excited.

Interaction with backward-wave is needed for electrons to couple with higher axial modes. This device is called gyro-BWO, and has potential to continuously tune output frequency. Output power of this device is currently less than 100 W, which is insufficient for the Ps-HFS measurement. A proposal for higher power is suggested in the future prospects (Sec. 4.3).

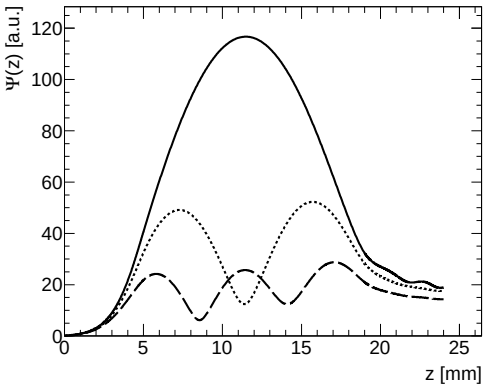

Figure A.3: Axial structure of the electric field in the RF cavity. Solid, dots, and dashed lines show TE_{521}, TE_{522}, TE_{523}, respectively.

mode	frequency [GHz]	Q_D	Q_Ω	Q
TE_{521}	203.01	3200	10600	2500
TE_{522}	203.59	810	10600	750
TE_{523}	204.56	380	10600	370

Table A.1: Resonant frequency and Q_D of three modes shown in Fig. A.3. Cavity parameters are $(L_1, L_2, L_3) = (5\,\text{mm}, 14\,\text{mm}, 5\,\text{mm})$, and $(R_1, R_2, R_3) = (2.345\,\text{mm}, 2.475\,\text{mm}, 2.735\,\text{mm})$.

A.3 Theory of the Electron Beam

An electron beam should be properly controlled and introduced to a right position in the RF cavity to obtain maximum coupling between electrons and the RF fields. A sophisticated method of electron control is developed in gyrotron physics. The simplest approximation is described in this section.

Electrons are emitted from an emitter ring on the cathode, accelerated between 1st and 2nd anodes (Fig. 2.2), and guided by a magnetic field to reach the RF cavity as gyrating where magnetic field strength is maximum (about 7.5 T) as shown in Fig. A.4. At last, the electron beam is dumped by a beam collector (Fig 2.2). Figure A.5 shows electron trajectories simulated by CST PARTICLE STUDIO [73]. Radius of the electron beam is compressed by the strong magnetic field at the cavity.

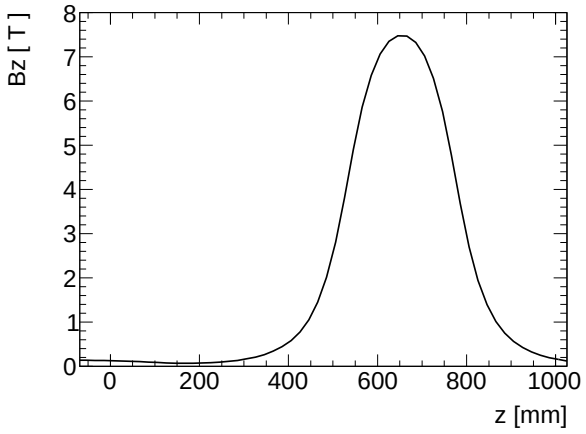

Figure A.4: Simulated magnetic field B_z on the z-axis (by CST PARTICLE STUDIO). The emitter ring is at z=0 mm, and the RF cavity is at 650 mm.

Beam radius R_b should provide maximum electron coupling to the one mode (TE_{mn1}) of the RF cavity discussed in Sec. A.2. This coupling strength is determined by a function

$$G_{mn} = \frac{J^2_{m\mp1}\left(j'_{mn}R_b/R\right)}{(j'^2_{mn} - m^2)J^2_m(j'^2_{mn})}, \tag{A.9}$$

where the sign in $m \mp 1$ corresponds to co-rotating or counter-rotating waves compared with the direction of electron gyration. Figure A.6 shows calculated G_{52}. It is clearly seen that the degeneracy of co- and counter-rotating modes is removed. When one operates a gyrotron oscillator in the counter-rotating TE_{52} mode, R_b should be controlled to be 0.7 of the cavity radius R_2.

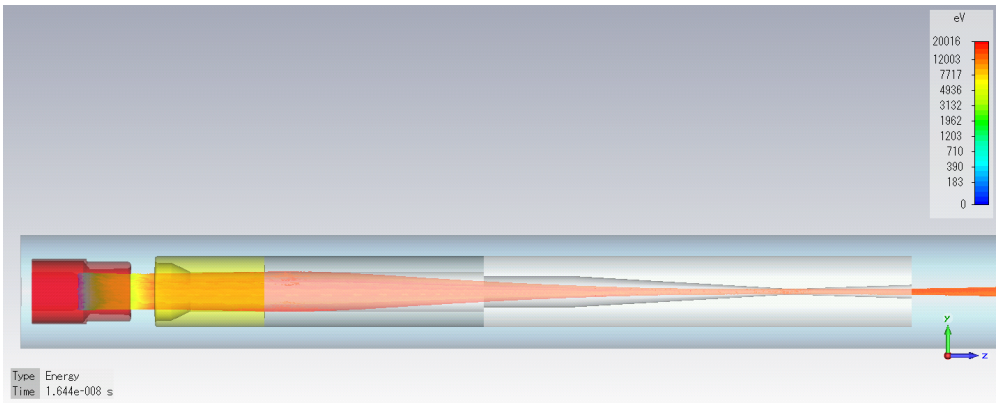

Figure A.5: Simulated electron trajectories from the MIG (by CST PARTICLE STUDIO).

Beam radius R_b is compressed depending on magnetic field strength as demonstrated in Fig. A.5. This adiabatic compression is expressed as

$$R_\mathrm{b}(z) = \sqrt{\frac{B_\mathrm{c}}{B_\mathrm{z}(z)}} R_\mathrm{c}, \tag{A.10}$$

where $B_\mathrm{c} \sim 0.1$ T is $z-$component of the magnetic field at the emitter ring on the cathode, and $R_\mathrm{c} \sim 14$ mm is the ring radius (Fig. 2.2). A factor $b = B_\mathrm{z}(z)/B_\mathrm{c}$ is called compression ratio. B_c is optimized by a normal conducting gun-coil solenoid around the MIG so that R_b becomes the proper value (i.e. 0.7 of the cavity radius),

The magnetic field induced by the gun-coil also affects the $E \times B$ drift near the cathode [74]. The $E \times B$ drift determines initial perpendicular velocity $v_{\perp c}$ of electrons emitted thermally from the cathode surface

$$v_{\perp c} \sim \frac{E_\mathrm{c}\phi_\mathrm{EB}}{B_\mathrm{c}}, \tag{A.11}$$

where E_c is electric field strength at the cathode, and ϕ_EB is the angle between E_c and B_c. E_c is controlled with difference of voltage between cathode ($V_\mathrm{k} \sim -18$ kV) and 1$^\mathrm{st}$ anode ($V_\mathrm{a} \sim -10$ kV). Electrons start gyrating because of this $E \times B$ drift.

According to an adiabatic approximation, the magnetic momentum $m_\mathrm{e} v_\perp^2 / B_\mathrm{z}$ is constant [74]; therefore, $v_\perp$ becomes faster and faster along the trajectory corresponding to the increasing magnetic field (Fig. A.4). Velocity parallel to B_z, $v_{//} = \sqrt{v^2 - v_\perp^2}$ is correspondingly reduced in the RF cavity since total energy is conserved. Energy of cyclotron radiation increases proportionally to $v_\perp^2$. The optimum value of the velocity ratio $\alpha = v_\perp / v_{//}$ (called pitch factor) at the cavity is from 1.2 to 1.5. The pitch factor is controlled with the magnetic field of the gun-coil and 1$^\mathrm{st}$ anode voltage.

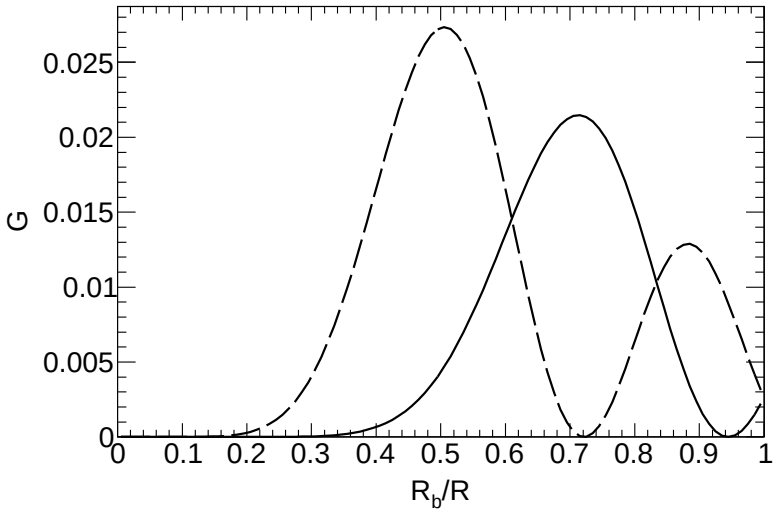

Figure A.6: Coupling factor of the TE_{52} mode. Solid line shows the counter-rotating mode, dashed one shows the co-rotating mode.

A.4 Excitation Theory

So far, RF fields in the RF cavity is obtained, and the optimum electron beam is introduced to the RF cavity. Now we calculate an interaction between them and think of excitation condition of the gyrotron [71]. We focus on a steady-state operation.

Gyrotron oscillation is estimated by calculating electron motion affected by the Lorentz force from the RF fields described in Sec. A.2. Electron's equation of motion in general is

$$\frac{d\mathcal{E}}{dt} = -e\overrightarrow{v}\cdot\overrightarrow{E} \tag{A.12}$$

$$\frac{d\overrightarrow{p}}{dt} = -e\overrightarrow{E} - \frac{e}{c}\overrightarrow{v}\times\overrightarrow{B}, \tag{A.13}$$

where $\mathcal{E} = m_{\mathrm{e}}\gamma c^2$ is energy of electron.

One can consider Eq. (A.13) in a coordinate system with origin at the electron gyrocenter. In complex notation, one denotes $\overrightarrow{p} \rightarrow p_{\mathrm{x}} + ip_{\mathrm{y}} = pe^{i\theta}$, where θ is a relative phase in momentum space between an electron momemtum and the electromagnetic wave. Electron energy and momentum is normalized by initial energy before the interaction (denoted as $m_{\mathrm{e}}\gamma_0 c^2$). Assume constant propagating velocity in the RF cavity, and independent variable is transformed from time to a

normalized axial position expressed as

$$\zeta = \frac{\beta_\perp^2 \omega_c}{2\beta_{//} c} z. \tag{A.14}$$

With the small argument expansion of the Bessel functions in $\overrightarrow{E}(r, \phi)$, resulting equation of motion is

$$\frac{dp}{d\zeta} + ip\left(\Delta + |p|^2 - 1\right) = iG \frac{\Psi(\zeta)}{\sqrt{\int |\Psi|^2 d\zeta}}, \tag{A.15}$$

where Δ is frequency detuning defined as

$$\Delta = \frac{2}{\beta_\perp^2}\left[\frac{\omega_r - \omega_c}{\omega_r}\right], \tag{A.16}$$

and G is coupling parameter defined as

$$G = \frac{1}{2}\sqrt{0.47 \times 10^{-3} \frac{Q_D \cdot P_{out}}{\gamma_0 V_k \eta_{el} \beta_{//} \beta_\perp^2} G_{mn}}. \tag{A.17}$$

Acceleration voltage V_k (cathode voltage), output power P_{out}, and electron efficiency

$$\eta_{el} = \frac{\beta_\perp^2}{2(1 - 1/\gamma_0)} \tag{A.18}$$

are also introduced.

One can understand steady-state gyrotron oscillation by solving Eq. (A.15) for *given* P_{out}. Note that P_{out} determines an absolute value of the RF field which is calculated without a source term in Cold Cavity formalism. The results of Eq. (A.15) for some electrons in different phases are shown in Fig. 2.4. Orbital efficiency is obtained by averaging the results of electrons initially in different phases $p_j(0) = \exp(i\theta_j)$ $(0 < \theta_j < 2\pi,\ j = 1, 2, \cdots, N,)$

$$\eta_\perp = 1 - \frac{1}{N}\sum_j |p_j(\zeta_{out})|^2. \tag{A.19}$$

Then, electron-beam current I_b required to achieve given P_{out} is calculated by

$$P_{out} = V_k \cdot I_b \cdot \eta_\perp \cdot \eta_{el} \cdot \frac{Q_\Omega}{Q_\Omega + Q_D}. \tag{A.20}$$

This is an enegy conservation condition between the electron beam and the RF field. The RF field gains energy from electrons calculated by Eq. (A.15) and Eq. (A.19). Figure A.7 shows an example of the solution for different magnetic field strength. Output power suddenly increases and gradually decreases when one raises magnetic field strength. This is a typical behaviour of the gyrotron oscillator.

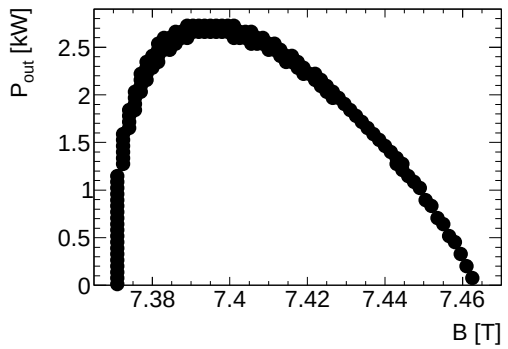

Figure A.7: Calculated output power of the gyrotron. Operation parameters are cathode voltage $V_{\rm k} = -18$ kV, beam current $I_{\rm b} = 500$ mA, magnetic field $B = 7.4$ T, cavity radius $R_2 = 2.475$ mm, beam radius $R_{\rm b} = 0.7 \cdot R_2$, and pitch factor $\alpha = 1.2$.

A.5 Soft and Hard Excitation

There are two oscillation conditions: soft excitation ($\omega_{\rm c} \leq \omega_{\rm r}$) and hard excitation ($\omega_{\rm c} \ll \omega_{\rm r}$). Figures A.8 show calculation of oscillation efficiency $\eta = \eta_{\perp} \cdot \eta_{\rm el}$ for these two conditions. η is a single-valued function of $I_{\rm b}$ in case of soft excitation (left figure). η is a multivalued function of $I_{\rm b}$ in case of hard excitation (right figure). High power is obtained in hard excitation. A difficulty of hard excitation is that the gyrotron start to oscillate at large $I_{\rm b}$, and η increases as $I_{\rm b}$ decreases for a while. After η exceeds ~ 0.1, η increases as $I_{\rm b}$ increases. Stabilization of output power with a simple feed-back control is difficult because of this non-linear behavior of the gyrotron (See Sec. 2.2.4). Moreover, two different η for the same $I_{\rm b}$ and B_0 (the same operation condition) can cause a sudden jump of output power without changing any external parameters. Careful operations are generally required in case of hard excitation.

A.6 Alignment Effect

Gyrotron oscillation is sensitive to displacement between the RF cavity and the electron beam. We introduce starting current $I_{\rm st}$ which is the smallest electron-beam current required for the gyrotron oscillation [72]. $I_{\rm st}$ can be calculated by the method described in Sec. A.4 with a condition $P_{\rm out} > 0$. Change of $I_{\rm st}$ by

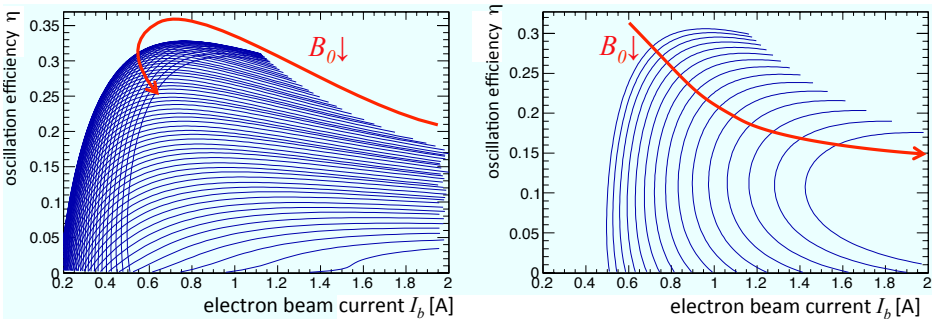

Figure A.8: Oscillation efficiency vs beam current. Left shows soft excitation and right shows hard excitation. A solid line shows oscillation with the same magnetic field or frequency detuning.

displacement d mm is expressed as [75]

$$I_{\rm st}(d) = I_{\rm st}(0)\frac{J^2_{\rm m\pm1}\left(\frac{2\pi}{\lambda}\cdot R_{\rm b}\right)}{\sum_q^{\infty} J_q^2\left(\frac{2\pi}{\lambda}\cdot d\right)\cdot J^2_{\rm m-q\pm1}\left(\frac{2\pi}{\lambda}\cdot R_{\rm b}\right)} \tag{A.21}$$

Results of the calculation are shown in Fig. A.9. In case of no displacement (left), only counter-rotating TE_{52} can oscillate when B_0 is set at 7.45 T and $I_{\rm b}$ is 0.4 A (the same condition as this experiment). In case of displacement of 0.5 mm (right), structure of $I_{\rm st}$ changes and both counter-rotating and co-rotating TE_{52} satisfy $I_{\rm st} > I_{\rm b} = 0.4$ A. These two modes compete with each other, and efficiency of electron's phase bunching is reduced (mode competition). Consequently, careful alignment better than 0.5 mm is required to obtain high-power gyrotron output. This is technically difficult because the size of gyrotron is rather large (Fig. 2.2). This is one of the reason of bad reproducibility of gyrotron operation (Table 2.2). Note that the gyrotron previously used in this experiment [54] is operated in TE_{03} mode of which counter- and co-rotating modes are degenerated. No mode competition occurs. The previous gyrotron is insensitive to the displacement. We select TE_{52} mode because conversion efficiency of the Gaussian mode converter is better than TE_{03} mode. The principle of the converter is described in the next section.

A.7 Theory of Gaussian Mode Converter

Output from the gyrotron RF cavity is $TE_{\rm mn}$ mode in a circular waveguide. One has to convert it to a linearly polarized Gaussian beam (TEM_{00} mode) to accumulate it in the Fabry-Pérot cavity [47]. This is achieved by a Gaussian mode converter developed in application for plasma heating.

When we consider the time-averaged Poynting vector using Eq. (A.1), the energy flux of $TE_{\rm mn}$ modes can be treated as *rays* bouncing along the inside wall of a

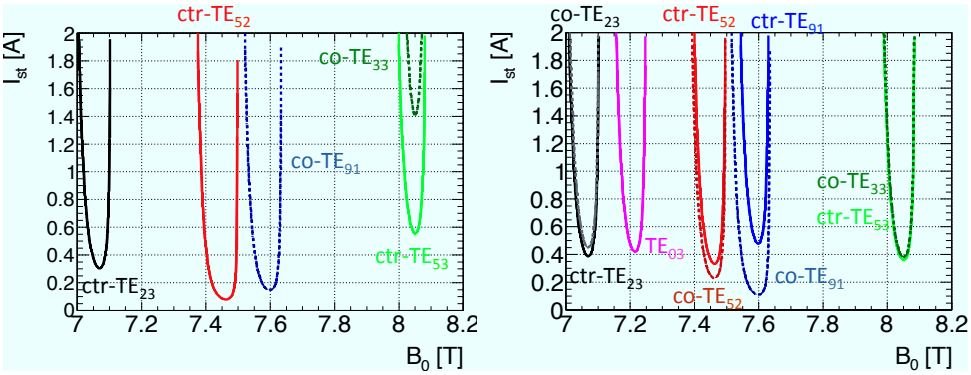

Figure A.9: Dependence of I_{st} on displacement. Left figure shows I_{st} with perfect alignment. Right figure shows I_{st} with displacement of 0.5 mm.

waveguide in a polygonal helix as shown in Fig. A.10. This picture reflects the fact that $\mathrm{TE}_{\mathrm{mn}}$ modes can be decomposed into a series of linearly polarized (helically rotating) plane waves. The envelope of helically reflecting rays in a waveguide with radius R_{W} becomes cylindrical *caustic* with radius R_{C}

$$R_{\mathrm{C}} = R_{\mathrm{W}} \times \frac{m}{j'_{\mathrm{mn}}}. \tag{A.22}$$

In case of TE_{52} mode we use, R_{C} is 0.475 of R_{W}.

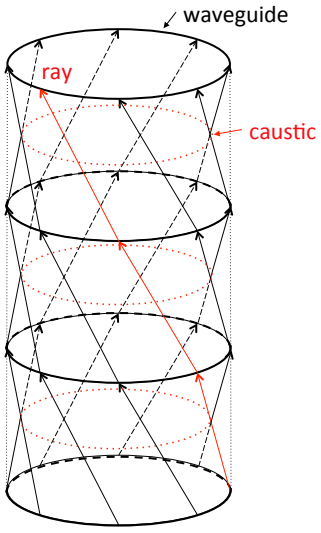

Figure A.10: Rays of time-averaged propagating $\mathrm{TE}_{\mathrm{mn}}$ mode in a waveguide.

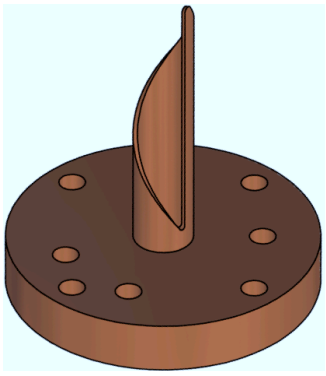

Figure A.11: Schematic view of the helical launcher.

The waveguide opening should be cut open in a helical shape with the helical cut following the ray trajectories in the waveguide. Figure A.11 shows a picture

of this helical launcher used in this experiment. The radiation launched from the helical antenna expands in a radial and twisted fashion corresponding to helical rotation in the waveguide. A quasi-parabolic reflector is introduced to focus the radiation and shape its profile. The left figure of Fig. A.12 shows a top view of the launcher and the reflector. The reflector shape calculated with a requirement of equal optical path length for all rays between the phase front and the focal point. For parallel light (focus point is at infinity), parametric representation $(x_\mathrm{r}, y_\mathrm{r})$ of the reflector shape can be expressed as [47]

$$x_\mathrm{r}(\phi) = R_\mathrm{C} - (2f_0 - R_\mathrm{C}\phi)\tan\left(\frac{1}{2}\phi\right) \tag{A.23}$$

$$y_\mathrm{r}(\phi) = R_\mathrm{C}\tan\left(\frac{1}{2}\phi\right) - \left(f_0 - \frac{1}{2}R_\mathrm{C}\phi\right)\left[\tan^2\left(\frac{1}{2}\phi\right) - 1\right], \tag{A.24}$$

where f_0 is the maximum value of y_r and ϕ is a parameter. In special case of $m = 0$, caustic radius $R_\mathrm{C} = 0$ and the reflector shape becomes

$$y_\mathrm{r} = -\frac{1}{4f_0}x_r^2 + f_0. \tag{A.25}$$

This type of reflector is used in the previous experiment in which the oscillation mode is TE_{03} [54]. The shape for $m \neq 0$ is similar to parabola, but slightly different (quasi-parabola). The reflected rays compose linearly polarized beam of which electric field vectors are parallel to the x-axis shown in the left figure of Fig. A.12.

The right figure of Fig. A.12 shows a side view of the launcher and the reflector. Propagating angle θ_B is called the Brillouin angle expressed as

$$\theta_\mathrm{B} = \sin^{-1}\left(\frac{j'_\mathrm{mn}\lambda}{2\pi R_\mathrm{W}}\right) \tag{A.26}$$

The axial structure should be fabricated so that reflected rays do not hit the launcher head for all frequency used.

One can make a linearly polarized bi-Gaussian beam with the launcher and the quasi-parabolic reflector. Two additional plane mirrors are located over the reflector to extract beam from a small bore of the superconducting solenoid (Fig. 2.2). An ellipsoidal mirror re-shapes the beam to focus at near the output window.

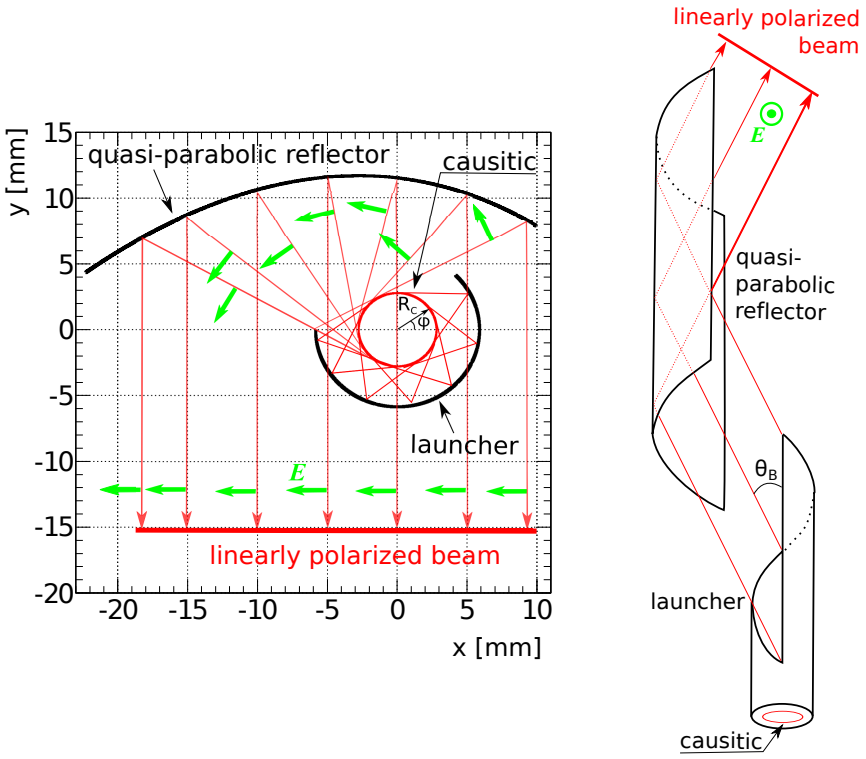

Figure A.12: Schematic view of Gaussian converter. (left) Top view. (right) Side view.

Appendix B

Theory of Positron Acceleration

B.1 Toy Model of the Interaction

Interactions between a positron, an oscillating electric field $E_0 \sin(\omega t)$, and gas molecules can be expressed as the following differential equation:

$$m_\mathrm{e} \frac{dv}{dt} = eE_0 \sin(\omega t) - m\omega_\mathrm{c} v, \tag{B.1}$$

where v is positron velocity, ω_c is averaged angular frequency of collisions, and $m\omega_\mathrm{c} v$ is a relaxation term by collisions. An analytical solution of Eq. (B.1) is

$$v(t) = \frac{eE_0}{m_\mathrm{e}} \sqrt{\frac{1}{\omega^2 + \omega_\mathrm{c}^2}} \sin\left[\omega t - \tan^{-1}\left(\frac{\omega}{\omega_\mathrm{c}}\right)\right]. \tag{B.2}$$

We estimate mean energy gain $\overline{\delta E}$ during collision cycle τ_c

$$\overline{\delta E} = \int_{t=0}^{t=\tau_\mathrm{c}} eE(t)v(t)dt = \frac{e^2}{2m_\mathrm{e}\omega_\mathrm{c}^2} \frac{\omega_\mathrm{c}^2}{\omega^2 + \omega_\mathrm{c}^2} \times E_0^2. \tag{B.3}$$

In case of 1 atm nitrogen gas and 1 eV positron, τ_c is about 3.3 ps. For 203 GHz millimeter waves, expected energy gain of a positron is

$$\overline{\delta E} \sim 0.51\,\mathrm{meV} \times \left(E_0/100\mathrm{kVm}^{-1}\right)^2 \tag{B.4}$$

per one collision. This is very small compared with Ore gap.

B.2 Random Walk Model

We can model a sequence of collisions by random-walk. Since millimeter-wave radiation in the Fabry-Pérot resonant cavity is linearly polarized, it is adequate to only consider one dimensional random walk. If collision is random enough and

not correlated to the electric field oscillation, probability distribution of v after n collisions can be expressed as

$$g(v) = \frac{1}{\sqrt{2\pi\sigma}} \exp\left[-\frac{(v-v_0)^2}{2\sigma^2}\right], \tag{B.5}$$

$$\sigma = \sqrt{n}\delta v, \tag{B.6}$$

where v_0 is an initial velocity of slow positron (a few eV), and δv is acceleration or deceleration per one collision determined by $\delta v = \sqrt{2m_e\overline{\delta E}}$. What we are interested in is probability to exceed the lower edge of Ore gap ($E_{\rm thr} = I - 6.8$ eV). When $v_{\rm thr}$ denotes corresponding positron velocity, this probability can be calculated by

$$G(v > v_{\rm thr}) = 1 - \int_{v_{\rm thr}}^{-v_{\rm thr}} g(v)dv. \tag{B.7}$$

Figure B.1 shows $G(v > v_{\rm thr})$ in 1 atm nitrogen case ($E_{\rm thr} \sim 7.7$ eV). Power dependence is related to $\overline{\delta E}$, which is determined by gas property at scattering.

Previous experiments studied an effect of static electric fields with a Boltzmann equation [60][61]. One can also construct a Monte Carlo simulation to model this phenomenon. Even with these seemingly more quantitative approaches, uncertainties in inelastic scattering are required to be determined through fitting the data. Comparison between models and data needs many data points at different accumulated power. This is difficult with current stability of the gyrotron.

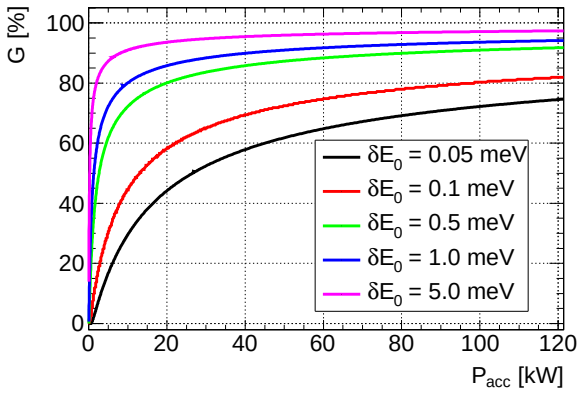

Figure B.1: Simulated Ps formation dependence on power. Calculations of different $\overline{\delta E_0}$ are plotted.

Appendix C

Data Summary

The quantities recorded at the main trigger timing are summarized in Table C.1. The quantities recorded in synchronization with the gyrotron output pulse are summarized in Table C.2. The quantities monitored with the interlock are summarized in Table C.3.

name	module
event ID	-
real time	-
gyrotron ON/OFF	input register (LeCroy C005)
Pla-energy (short gate), 2ch	CS ADC (PHILLIPS 7167)
Pla-energy (long gate), 2ch	CS ADC (REPIC RPC-022)
La-energy, 4ch	CS ADC (CAEN C1205)
Pla-time, 2ch	TDC (KEK GNC-060)
La-time, 4ch	TDC (KEK GNC-060)
live time	SCALER (Kaizu KC3122)
Pla-rate, 2ch	SCALER (Kaizu KC3122)
Pla-and-rate	SCALER (Kaizu KC3122)
La-rate, 4ch	SCALER (Kaizu KC3122)

Table C.1: Quantities measured at main trigger timing.

name	device
input power	pyroelectric detector
reflected power	pyroelectric detector
transmitted power	pyroelectric detector
trigger pulse of gyrotron	ADC (NI USB-6215)
beam current of gyrotron	ADC (NI USB-6215)
heater voltage of the MIG	(input parameter)
cavity length	NANO CONTROL TS102-G
room temperature	logger (HIOKI 8420-50)
temperature of NIM bin	logger (HIOKI 8420-50)
temperature in the gas chamber	logger (HIOKI 8420-50)
pressure in the gas chamber	logger (HIOKI 8420-50)

Table C.2: Quantities recorded in synchronization with gyrotron output pulse.

name	reason
temperature of the collector	check abnormal electron beam operation
temperature of the gyrotron body	check abnormal electron beam operation
temperature of the flange on the MIG	check abnormal electron beam operation
temperature of the output window	protect window glass
vacuum of the gyrotron	protect the emitter surface of the MIG
water flow for gyrotron cooling	protect gyrotron vacuum vessel
water flow for chamber cooling	prevent the mesh mirror from melting

Table C.3: Quantities monitored with the interlock.

Appendix D

Small Systematic Uncertainties

Efficiency of accidental rejection and background normalization are negligible in calculating Ps-HFS compared with other errors. The differences are small but significant, and listed in Table D.1 and Table D.2 for the future precise measurement. They may be due to electric noise of the pulse operation of the gyrotron (voltage=−18 kV, current=500 mA, width=60 ms, frequency=5 Hz). RUNs in which Fabry-Pérot cavity is off-resonance (-0) are also shown as a reference.

RUN ID	efficiency (beam ON)	efficiency (beam OFF)	difference
A-1	56.544(76) %	56.486(50) %	0.10333(17)%
A-2	56.916(77) %	56.973(51) %	−0.09990(16)%
B-0	52.083(86) %	52.179(56) %	−0.18416(36)%
B-1	52.574(65) %	52.570(43) %	0.00799(1)%
C-0	56.464(96) %	56.362(65) %	0.18097(37)%
C-1	56.156(69) %	56.283(63) %	−0.22565(38)%
C-2	54.35(10) %	54.370(66) %	−0.03678(8)%
C-3	56.576(79) %	56.614(52) %	−0.06712(11)%
D-0	54.46(13) %	54.418(87) %	0.07673(22)%
D-1	53.047(73) %	53.060(48) %	−0.02458(4)%
D-2	54.69(18) %	55.07(12) %	−0.6838(27)%
D-3	54.41(18) %	54.40(11) %	0.01758(7)%
D-4	54.34(17) %	54.45(11) %	−0.20478(78)%
D-5	54.63(19) %	54.69(12) %	−0.11336(47)%
E-0	54.580(93) %	54.590(61) %	−0.01841(4)%
E-1	54.434(92) %	54.402(60) %	0.05929(12)%
E-2	55.143(90) %	55.025(60) %	0.21576(42)%
F-0	56.10(14) %	56.104(92) %	−0.002552(8)%
F-1	56.381(69) %	56.258(45) %	0.21881(32)%
F-2	52.779(72) %	52.732(47) %	0.08910(14)%
G-0	55.217(65) %	55.146(43) %	0.12797(18)%

Table D.1: Accidental rejection efficiency.

RUN ID	livetime	uncertainty
A-1	6.7×10^4 sec	0.07 %
A-2	6.7×10^4 sec	0.07 %
B-0	7.0×10^4 sec	0.08 %
B-1	1.1×10^5 sec	0.06 %
C-0	7.2×10^4 sec	0.08 %
C-1	6.6×10^4 sec	0.08 %
C-2	6.8×10^4 sec	0.08 %
C-3	9.9×10^4 sec	0.07 %
D-0	2.6×10^4 sec	0.07 %
D-1	7.2×10^4 sec	0.12 %
D-2	1.2×10^4 sec	0.17 %
D-3	1.3×10^4 sec	0.16 %
D-4	1.4×10^4 sec	0.15 %
D-5	1.3×10^4 sec	0.16 %
E-0	2.3×10^5 sec	0.08 %
E-1	6.1×10^4 sec	0.08 %
E-2	6.0×10^4 sec	0.09 %
F-0	5.8×10^4 sec	0.12 %
F-1	1.0×10^5 sec	0.06 %
F-2	8.0×10^4 sec	0.07 %
G-0	1.2×10^5 sec	0.06 %

Table D.2: Normalization uncertainty.